Understanding Crystal Nucleation through Pressure-driven Phase Transformations

Suse Bebiano

Thesis submitted to the Strathclyde Institute of Pharmacy and Biomedical Sciences at the University of Strathclyde in accordance with the requirements for the degree of Doctor of Philosophy

2021

Declaration of Author's Rights

This thesis is the result of the author's original research. It has been composed by the author and has not been previously submitted for examination which has led to the award of a degree.

Signed: Sara Vanessa dos Santos Bebiano Date: 21/06/2021

Acknowledgements

Firstly, I would like to thank my supervisor, Dr. Iain Oswald. In the first years of my PhD, our weekly meetings and your support in the laboratory was very important. I felt excited and motivated to be learning every day about high-pressure. Your support was crucial to continue during the following years. Thank you. I also would like to thank my supervisor, Prof. Joop ter Horst for his support and inputs in all our meetings and during writing up.

To the members of the Oswald group, I was very lucky to have the opportunity to meet you and discuss our research and life in general. Thank you Abdullah Al Balushi for having been a good friend and maybe one day we will meet in Thailand. Thank you Metinee Hemaprasertsuk for the funny and easy afternoons/evenings in front of Raman waiting for the next pressure point. Thank you Martin Ward for your support and for showing me the exciting new setups in the lab. To Lauren Connor, the person that could travel with me in phase diagrams or social dilemmas, questioning everything and getting lost or maybe not (who knows) in our thoughts. To everyone around me in the office mainly Carla Ferreira and Tony Vassileiou. To Bilal Ahmed for being the first and the last person to talk at the office, your conversations were always interesting.

To my family, thank you for being there. I am grateful for your efforts to give me the best.

Lastly, to Javier for being so similar and so different to me. Thank you for trying and trying to help in every step of this journey, by minimizing my doubts and helping me to find solutions. Thank you for always believing.

Contents

List of Tables

List of Figures

List of Abbreviations

API	**A**ctive **p**harmaceutical **i**ngredient
BM	**B**irch-**M**urnaghan
CCDC	**C**ambridge **C**rystallographic **D**ata **C**entre
CNT	**C**lassical **n**ucleation **t**heory
CSD	**C**ambridge **S**tructural **D**atabase
CSP	**C**rystal **S**tructure **P**rediction
CTZ	**C**hloro**t**hia**z**ide
DAC	**D**iamond **a**nvil **c**ell
DHBA	2,4-**d**i**h**ydro**b**enzoic **a**cid
DMSA	2,2-**d**i**m**ethyl**s**uccinic **a**cid
DSC	**D**ifferential **s**canning **c**alorimetry
EoS	**E**quation **o**f **s**tate
Eti	**Eti**racetam
FA	**F**umaric **a**cid
FIM	**F**ull **i**nteraction **m**ap
GoF	**G**oodness **o**f **F**it
HCT	**H**ydro**c**hloro**t**hiazide
HP	**H**igh-**p**ressure
HRPD	**H**igh **R**esolution **P**owder **D**iffractometer
Lev	**Lev**etiracetam
LVP	**L**arge **v**olume **p**ressure
M	**M**urnaghan

MA	**M**alonic **a**cid
MSZW	**M**eta**s**table **z**one **w**idth
NBA	4-**n**itro**b**enzoic **a**cid
Nct	**N**i**c**o**t**inamide acid
Nic	**Nic**otinic acid
MOF	**M**etal-**o**rganic **f**ramework
OA	**O**xalic **a**cid
***p*ABA**	4-**a**mino**b**enzoic **a**cid
PTFE	**P**oly**t**etra**f**luoro**e**thylene
PTM	**P**ressure **t**ransmitting **m**edia
Res	**Res**orcinol
SA	**S**uccinic **a**cid
Sam	**S**uccin**am**ide
SLE	**S**olid-**l**iquid **e**quilibria
XRPD	**X**-**r**ay **p**owder **d**iffraction

Abstract

This thesis investigates the nucleation and the discovery of new phases using solubility and high-pressure measurements of chiral and racemic solids of (RS)/(S)-2-(2-oxopyrrolidin-1-yl)butanamide. The cocrystallisation of this compound with a range of different coformers has been investigated using solubility measurements to alter the eutectic composition to aid the chiral resolution. Only one successful cocrystal was isolated and was observed to move the eutectic composition. However, this moved towards the chiral phase rather than the racemic composition hence reducing the phase space available for the chiral resolution. Whilst this result is less ideal, the ability to move the eutectic composition is demonstrated and the role of the cocrystal solubility in this process identified. To follow this study, the response of Levetiracetam and Etiracetam to high pressure was investigated with a view to identifying phase transitions that may be used in future measurements of nucleation using high pressure. In this work, both materials undergo phase transformations to new high pressure phases. The changes to both were very subtle and difficult to analyse using Raman spectroscopy, which would have been the best method for phase identification during nucleation due to the speed of collection. The difference in the compression are analysed through void analysis as well as energy calculations to confirm the phase transition had taken place. Lastly, hydrochlorothiazide was identified as a potential compound to use in the nucleation measurements. The phase transition to a new phase occurs at ~0.5 GPa and the Raman spectrum indicated a distinct change over the phase transformation which was one of the key concepts for analysis. Unfortunately, the phase transformation is not reversible within a short time scale. The high-pressure form is stable as a solid for many months without transformation. This observation led the study on a different path to explore the formation and recovery of this high-pressure phase. The high-pressure parameters for the successful recovery of the phase were explored as well as the indexing of the new phase. A potential indexing of this new phase is identified, however, the solution of the new phase has eluded characterisation.

Chapter 1

Introduction

In this chapter, we present an overview of the structural topics relevant to this thesis. Starting with a broad view of crystallisation, crystal nucleation and polymorphism followed with a brief introduction to the field of high-pressure applied to the organic solid-state.

1.1 Crystallisation

Crystallisation is a separation and purification technique of substances where an ensemble of randomly organized molecules, ions or atoms in a solution come together to form an ordered three-dimensional molecular array that is designed as crystal. In the pharmaceutical field, crystallisation is usually the process that follows the synthesis of an organic compound, an active pharmaceutical ingredient (API). The result, normally, is a suspension that contains the desired crystalline product, whereas the solution contains impurities and, to an extent, the dissolved product. After filtration or other separation technique, the crystalline product obtained is characterized by purity, yield, size distribution, crystal form and crystal shape.[1,2] The optimization of a crystallisation process to higher values of yield and purity, and the control of size, crystal form and crystal shape, is the key for an efficient process.[2] Control of crystallisation is very important because it can affect primary unit operations, such as filtration and drying, secondary processing (milling) and manufacturing (tablet production).[1]

In crystallisation from solution the solvent plays an important role in the process. The choice of the appropriate solvent, indeed anti-solvent, is crucial in its ability to aid crystallisation.[3] Solvent properties such as polarity, hydrogen bond donor or acceptor groups and solid-liquid interfacial tensions can all affect the solubility, purity, crystal habit and polymorphic form (the ability of a compound to adopt more than one crystalline form).[4,5] For example, by varying the solvent we can alter the shape of the crystal which can affect the ability to process the material. Phenytoin crystals have been shown to change the morphology depending on the solvent of choice.[6] Crystallisation using a protic solvent such as ethanol produces needle-shaped crystals whereas more block-like crystals can be formed from crystallisation from non-protic solvents, e.g. acetone, through solvent evaporation. The rationale for the alteration being the promotion of the hydrogen bonded chain in the former leading to long needle-like crystals.

The two types of crystallisation are crystallisation from the melt and crystallisation from solution. Melt crystallisation is possible in a small-scale lab discovery process but not for manufacturing – solution crystallisation is more scalable. Regarding crystallisation from solution, Figure 1.1 depicts all four existing sub-types:[2]

(a) Cooling Crystallisation, where the crystallisation relies on a changes in the solubility with a change in the temperature of the solvent. As the solution is cooled the solute is less soluble hence precipitates from solution;

(b) Evaporative crystallisation, where the evaporation of solvent leads to reduction of solvent volume and consequently the increase of concentration which initiates precipitation;

(c) Antisolvent crystallisation, where antisolvent (a solvent in which the solute has limited solubility) will dilute the concentration of the solution (in volume terms), however a change in the property of the mixed solvent over the pure solvent initiates the precipitation of the solid;

(d) Precipitation crystallisation, where the reaction between two ions creates a new solid whose solubility is lower than the reactants hence precipitation occurs.

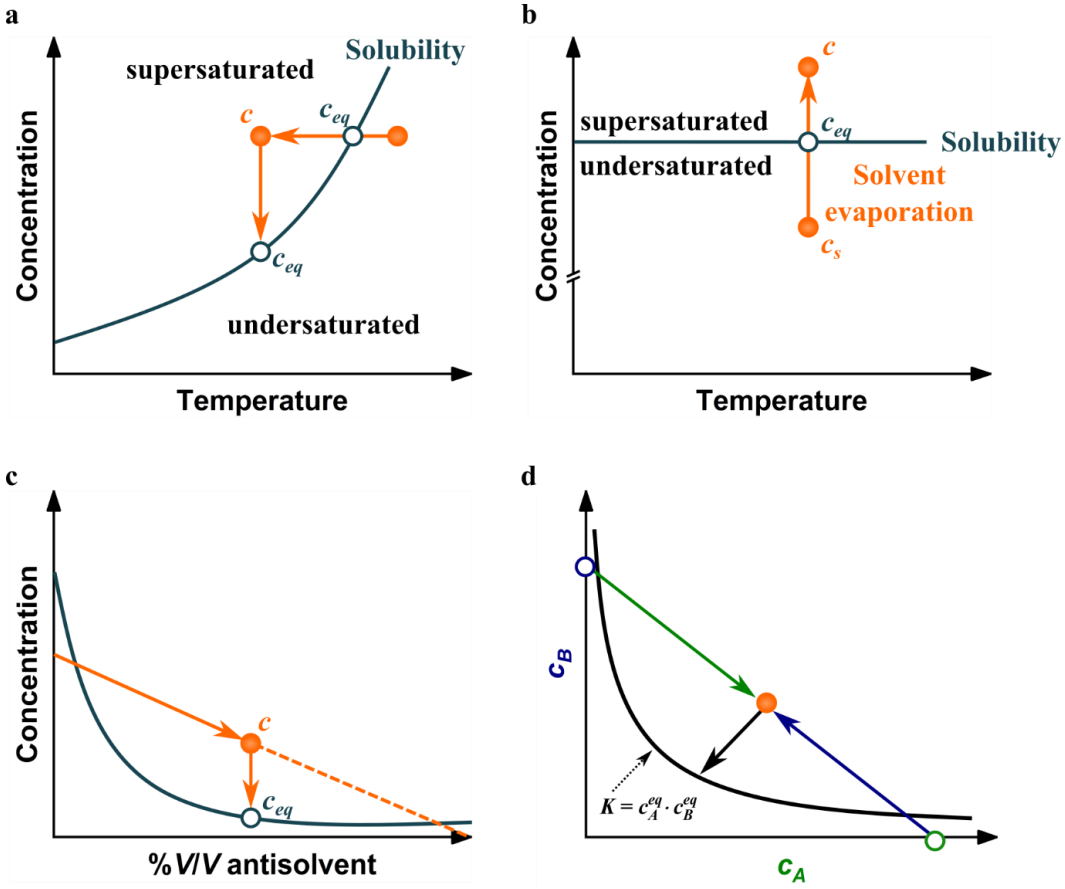

Figure 1.1-Type of crystallisation from solution: (a) cooling crystallisation, (b) evaporative crystallisation, (c) antisolvent crystallisation and (d) precipitation is where two solutions of pure Adapted from Horst et al. article.[2]

The basis of crystallisation is the existence of a driving force that alters an undersaturated solution to a supersaturated one.[2] The zones are divided by solubility curve which is illustrated in Figure 1.2. Spontaneous formation of a new crystal is only

possible above a critical level (dotted curve). The region between the solubility curve and the supersaturated curve is called the metastable zone where the crystal will grow but nucleation process is less observed. The width of the metastable zone width (MSZW) is determined by kinetics and can be affected by agitation[7], cooling/heating rate and impurities[8] whilst solubility curve is a thermodynamic measurement.[9] It is important to note that the knowledge of MSZW is crucial to control the crystal nucleation and crystal growth processes. This is important in the industrial context when the control of polymorphism is critical to their process.[1,2] In the industry, they use seed crystal to promote the formation of the desired polymorph whilst overcoming the nucleation of an undesired form.

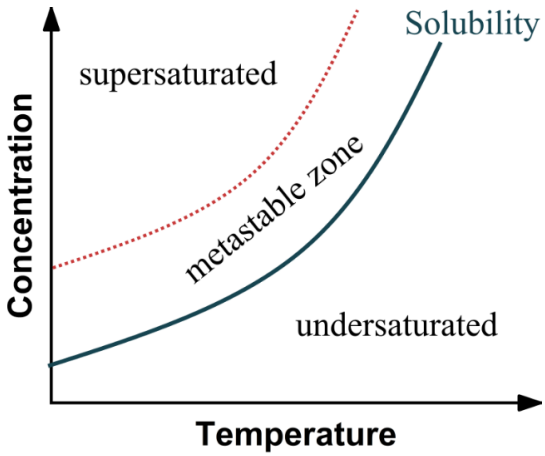

Figure 1.2 – A schematic diagram of a typical concentration/temperature graph indicating the undersaturated, supersaturated regions and the metastable zone in between these two states.

1.2 Nucleation

In crystallisation, nucleation is a phenomenon observed in a transformation from liquid, vapour or solid form to a new crystalline form. The main focus in crystallisation is the formation of a nuclei from a supersaturated solution or melt. The process of nucleation is a stochastic event and is driven by kinetics. It is divided into several

stages: starting from birth of the first nuclei, as the result of the interaction between the components in the system, to growth of the nuclei to particles of a detectable size.[4] There are two different mechanisms that nucleation is thought to precede: classical nucleation theory (CNT) and "nonclassical" crystal nucleation (two-step nucleation mechanism), Figure 1.3.[4]

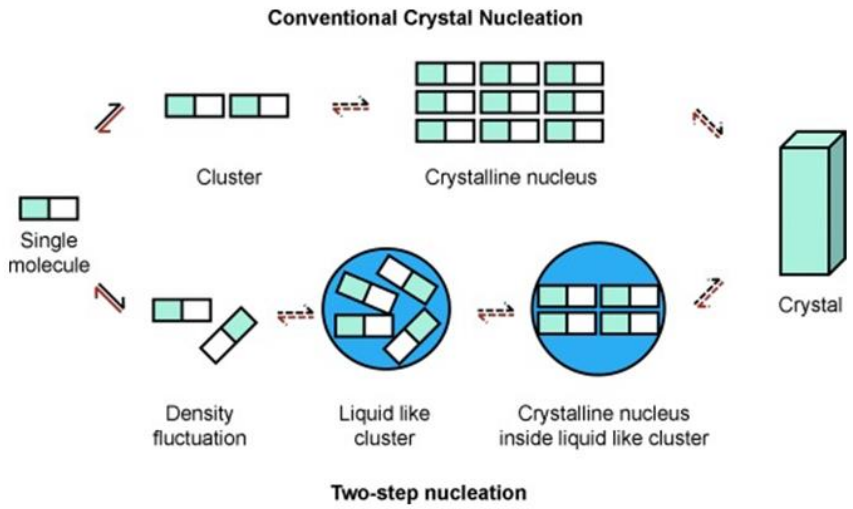

Figure 1.3 – Mechanisms of nucleation in crystallisation from solution. Conventional crystal nucleation is also known as classical nucleation theory (CNT) (top) and two-step nucleation also known as "nonclassical" crystal nucleation (bottom). Taken from Davey et al. article[4]

Classical nucleation theory is identified with small clusters of ordered molecules that resemble known polymorphic forms in a crystalline nucleus - this grows into a crystal. The two-step nucleation process begins with an unordered state where solute molecules gather together in a liquid like cluster. From this state, the molecules order into a cluster that gives origin to a crystal that can then grow.

The nucleation of a system can change with varying nucleation parameters such as supersaturation ratio and rate of cooling. Jiang et al.[10] investigated nucleation rates through the use of probability measurements. In this experiment, they measured

induction time using the Crystal 16 where 16 vials filled with different supersaturation ratios (6 in total) were monitored as a function of temperature. This was done by measuring the turbidity of the solution as a function of temperature. They demonstrated that increasing the supersaturation ratio of *m*-aminobenzoic acid from 1.83 to 2.15 increased the nucleation rate from 50 to 4.03×10^3 $m^{-3} \cdot s^{-1}$. Also, the increase of supersaturation ratio of L-histidine from 1.55 to 1.74 increased the nucleation rate from 160 to 1.98×10^3 $m^{-3} \cdot s^{-1}$. This is a significant increase of nucleation just by varying supersaturation.

To evaluate the cooling rate, Yang *et al.*[11] explored the system of ascorbic – water at constant supersaturation by, again, using probability measurements. In total, 192 measurements of nucleation time and MSZW were carried out in Crystal16 at four different cooling rates 18.0, 9.0, 6.0 and 3.0 $K \cdot hour^{-1}$. They verified that the nucleation time at $P(t) = 0.5$ for measurements using a cooling rate of 18.0 $K \cdot hour^{-1}$ is *approx.* 6600 s with a rapid completion of the nucleation process. In contrast, with the experiments performed at 3.0 $K \cdot hour^{-1}$, the MSZW was much narrower despite having a large nucleation time window. The higher cooling rate (18 $K \cdot hour^{-1}$) increases the MSZW explained by the fact that the solution reaches a lower temperature, due to the rate of temperature change, before nucleation occurs despite the observation of a higher nucleation rate shown in Figure 1.4. Both of these examples show that supersaturation and cooling rate will affect nucleation measurements which would, in turn, impact the design of the control crystallisation in an industrial environment.

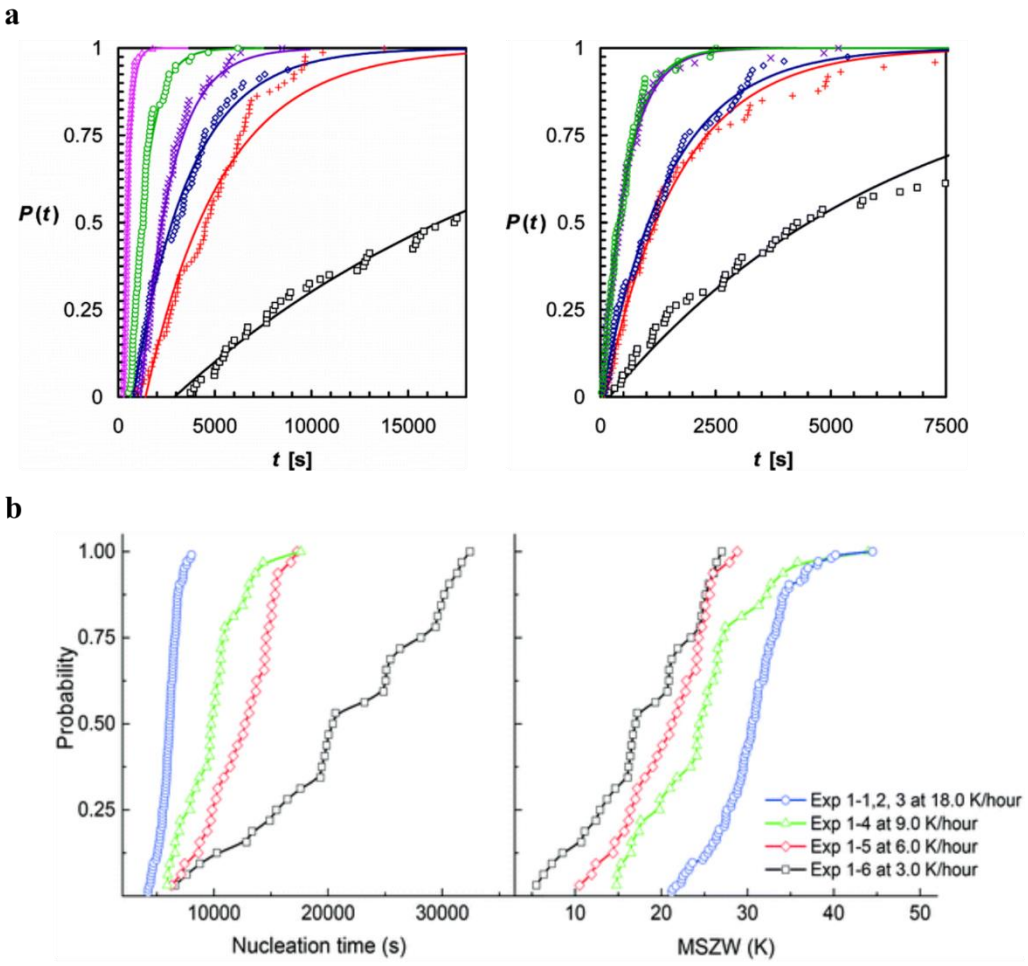

Figure 1.4 – Examples of nucleation studies where cumulative distributions of nucleation times: (**a** –left) *m*-aminobenzoic acid at supersaturation ratios *S* = 1.83 (□), 1.87 (+), 1.93 (◇), 1.96 (×), 2.06 (○), and 2.15 (Δ) in 50 wt % water/ethanol mixtures ; (**a**- right) L-histidine *S* = 1.55 (□), 1.60 (+), 1.64 (◇), 1.69 (×), and 1.74 (○) in water and (**b**-bottom**)** ascorbic in water. The investigation of factors as supersaturation and cooling rate in the crystallisation process is crucial to achieve the desired product. Taken from Jiang et al.[10] and Yang et al[11].

In these examples, they tried to by varying experimental parameters to change the nucleation rate which can impact the metastable zone. The control of this zone is critical to the isolation of a particular polymorph with desirable properties.[1]

1.3 Polymorphism

In this thesis, we define polymorphism as the capacity of a compound with a specific chemical composition to rearrange in different crystalline structures.[12–14] This phenomenon is a result of packing[15] or conformation polymorphism[16–19]. If a compound has rigid molecules, the different arrangements are due to the organization in the packing (e.g. Paracetamol[20,21]). Alternatively, if a compound has flexible molecules, the different conformations can result in different arrangements leading to conformational polymorphism (e.g. L-glutamic acid[22] where the conformers present in α and β polymorph differ in the orientation of the carboxylate group with respect to the carbon backbone).

This definition excludes the addition of new molecules into the system (or guest molecules) such as hydrates (compounds that contain water molecules or its chemical elements), cocrystal (a multi-component compound with different neutral molecules), solvates (multi-component compound where one of the components is a solvent molecule) and salt (multi-component compound that contains different ionic species). These crystalline forms are showed in Figure 1.5. All these solid forms can present polymorphism, as long as the chemical composition continues to be the same. In pharmaceutical industry, the screening of polymorph is required to characterize an API.[1,2,23,24] The reason behind this is the huge implication that a polymorphic transition could affect the bioavailability[25], solubility, processing or storage of a drug. Ritonavir is an example of a drug where the appearance of a new polymorphic form decreased the bioavailability and solubility.[16]

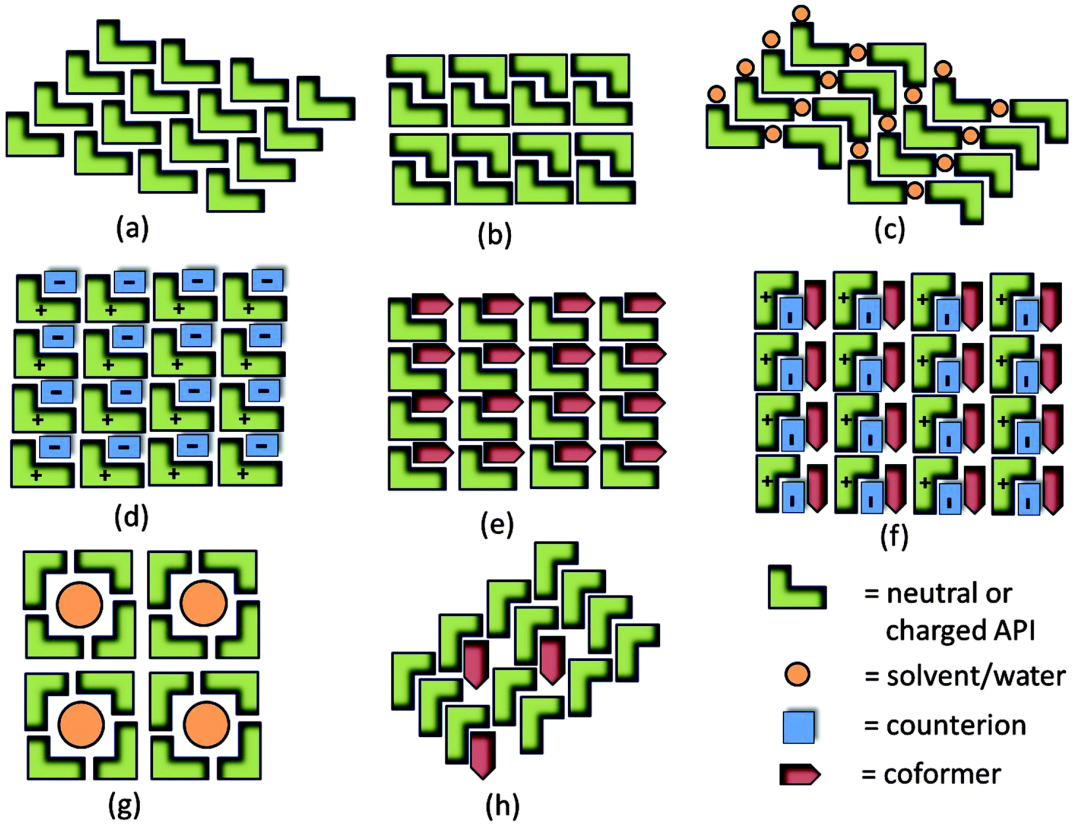

Figure 1.5 – Representation of solid forms of a compound A: **a** polymorphic form I and **b** polymorphic form II; **c** solvate or hydrate; **d** salt; **e** cocrystal; **f** ionic cocrystal; **g** non-stoichiometric inclusion compounds including channel hydrates/solvates and **h** solid solutions (mixed crystals). Taken from Duggirala et al.[26]

The transition of a different polymorphic form can be associated to different packing properties (e.g. density), thermodynamic properties (e.g. melting point[27–29], enthalpy[30], free energy[31] and solubility)[32] kinetic properties (e.g. dissolution rate, rates of solid-state reactions)[33], stability, (e.g. surface free energy, interfacial tensions, crystal habit) and mechanical properties (e.g. hardness, tensile strength, tableting, flowability).[34] All these properties have an important role in pharmaceutical products and in the manufacturing process. Therefore, the selection of the polymorph for new pharmaceuticals is a compromise between physical, chemical, pharmaceutical and biopharmaceutical properties.[32] The continuous monitoring of polymorphic form at all

stages of drug manufacture is a crucial procedure to ensure the desired pharmaceutical product is preserved from early stage of polymorphic selection to shelf storage.[32]

The control of nucleation and growth can define the polymorphic form obtained at the end of crystallisation process.[1] The formation of the first nuclei is associated to the polymorphic form where the process of nucleation is faster, a consequence of a lower free energy barrier (ΔG) to nucleate. However, the crystal growth rates could allow another polymorphic form to coexist in a crystallisation process. Therefore, the formation of polymorphs is influenced by thermodynamic and kinetic conditions until achievement of equilibrium.[2]

The type of crystallisation can assist the formation of a specific polymorph by selecting conditions that benefit nucleation and growth of one form over another. For example, the design of a cooling crystallisation the choice of parameters such as solvents[35], cooling profile, concentration and mixing condition have an impact in the polymorphic form produced. In crystallisation from the melt,[36,37] the temperatures change[38] (min, max and gradients) could induce the formation of another polymorphic form. As an alternative of temperature, pressure (typically up to 10 GPa induced in organic compounds) can be used as a thermodynamic parameter to prompt a new polymorph form from solution or by compressing crystalline material. The high-pressure topic is explained in more detail in the section 1.5.

In the pharmaceutical industry, it is necessary to select a crystalline form that presents specific physicochemical and biopharmaceutical properties. When the polymorphic forms known do not show the desired behaviour, the crystallisation of API with other chemical species can be a route to explore the properties of the material. Hydrates and solvates can present advantages in terms of stability at ambient

conditions.[32] Salts and cocrystals are also an option to change properties such as solubility, dissolution rate and stability.[32,39–41] The difference between these two compounds is the type of the guest molecule. In salts, the guest is an ionic species which reduces the number of suitable counterion candidates due to specificity of interaction between the ionisable API with the counterion.[42] In the case of cocrystals, the guest molecules are neutral species (known as co-formers) which lists hundreds of possible candidates for cocrystals formation.[43]

1.4 Cocrystal

The application of cocrystals in the pharmaceutical industry has expanded in the last decade.[44] Cocrystals are formed by two neutral chemical molecules that interact through hydrogen bonds (no covalent bonds are broken or formed in the cocrystallisation process). Cocrystals are designed to improve the properties of the target compound. In the agrochemical industry, urea is used as a source of nitrogen. Due to its higher solubility (ca. 110–170 g/100 ml, in the 20–40 °C range), the impact in water quality, biodiversity and human health can be harmful. This compound is hygroscopic which presents problems in transportation, handling, and storage. Sandhu et. al,[45] explored the landscape of urea using full interaction maps (FIMs) and the data available in CSD (Cambridge Structural Database). From 60 attempted reactions, the formation of crystals was reported in 49 reactions. Furthermore, they were able to find two urea cocrystals that presented lower solubility and hygroscopicity. The urea:pimelic acid and urea:4-nitrophenol cocrystal presented a 20-fold and 60-fold decrease in the aqueous solubility of urea, respectively.[45] The results also showed that urea became transparent liquid in less than 24 hours at 85% humidity, however,

urea:pimelic acid and urea:4-nitrophenol cocrystals remained crystals solids for over one month. That means that these cocrystals could be applied as a slow-release fertilizer and the limited hygroscopicity could avoid problems of handling.[45]

Cocrystals have been used as a method to design drugs with specific physicochemical properties.[32] Sanphui et. al,[46] studied hydrochlorothiazide (HCT) a diuretic API with low aqueous solubility (0.7 $g \cdot L^{-1}$) and low permeability (Caco-2 permeability: −6.06). The cocrystals of HCT−nicotinic acid (HCT−Nic), HCT−nicotinamide (HCT−Nct), HCT−succinamide (HCT−Sam), HCT−4-aminobenzoic acid (HCT−*p*ABA) and HCT−resorcinol (HCT−Res) were prepared using liquid-assisted grinding.[46] The results showed that higher solubility for all of the cocrystals with exception of HCT−Sam when compared to HCT: HCT−*p*ABA (2.4-fold) > HCT−Res > HCT−Nct (1.3-fold)> HCT > HCT−Nic > HCT−Sam. The values of permeability also showed higher values for all of the cocrystal with the exception again of HCT−Sam: HCT−Nic (2-fold) > HCT−Nct (1.8-fold) > HCT−Res > HCT−*p*ABA (1.3-fold) > HCT > HCT−Sam.[46] Therefore, cocrystallisation is a useful way to tune the physicochemical properties but further investigation during formulation will be a necessary step to maximise the potential of these systems.

1.5 High-pressure

The thermodynamic parameter pressure is rarely explored to induce transformation in materials. However, in the last decade, the effect of pressure has been explored in diverse fields such as alcohols[47–50], amino acids[51], metal-organic framework materials (MOFs),[52] polymers and APIs[53–56]. The increase of research in this area is associated to the development of high-pressure equipment such as the diamond anvil cell (DAC)

and large volume pressure (LVP) concomitant with the improvement of diffraction methods at University's laboratories and synchrotron facilities. Nowadays, the application of pressure can be useful to: a) discover polymorphic forms that have been missed by ambient-pressure screening experiments; b) serve as probe to understand important features of intermolecular and intramolecular interaction in a material[57,58]; c) explore ambient metastable forms that are stable high-pressure forms with the ability to be recovered at ambient condition and d) to characterize *in-situ* transformation that can occur during the drug processing and manufacturing.

The investigation of MOFs using high-pressure was applied to explore the importance of metal-metal bonds and metal-framework bonds (intramolecular interactions) and intermolecular interactions. Woodall et al.[59] investigated tris-(μ_2-3,5-diiso-propyl-1,2,4-triazolato-κ_2N^1:N^2)trigold(I) complex in crystalline state under high pressure. This complex undergoes for successive polymorphic transformations driven by aurophilic interactions (Au…Au intermolecular interactions). In this study, a total of four phase transitions were described for this complex at 1.69 GPa (Form II), 2.18 GPa (Form III), 2.70 GPa (Form IV) and at 3.3 GPa (Form II). The highlight of this study is the last phase transition that results in the rare reappearing of form II at high-pressure. The rich polymorphic behaviour was characterized via spectroscopy and X-ray diffraction.[59]

In the case of amino acids, they have been explored extensively under ambient conditions, yet with the high-pressure it was possible to access new polymorphic forms. For example, DL- and L- forms of serine[51,60–65], cysteine[66,67] and alanine[68,69] at high-pressure possess different behaviour under compression. Two high-pressure polymorphic forms were described for L-serine, form II and III which transitions occur

at 5.3 GPa and 7.8 GPa, respectively; in each of the transitions the orthorhombic symmetry is retained. The transformations in L-serine are related to changes in the conformations of the zwitterions thereby altering the hydrogen--bonded network. In the case of DL-serine, no phase transitions were observed up to a pressure of 8.6 GPa. L-cysteine possesses two polymorphic forms at atmospheric pressure, an orthorhombic form I and a monoclinic form II. Only the orthorhombic form of L-cysteine has been investigated at high-pressure and gives rise to two new high-pressure polymorphs (III and IV). The transformation behaviour of form I of L-cysteine depends on the pressure treatment of the sample and the pressure-transmitting medium. In pentane:isopentane, small increases in pressure cause a reconstructive phase transition to occur breaking up the single crystals at ~1.8 GPa. If the pressure is applied in large steps, then the single crystal remains intact and can be identified as form III (orthorhombic). However, in 4:1 methanol:ethanol the speed of compression has no effect; the single crystal remains intact and undergoes the transition.[70] The effects of pressure transmitting medium on the behaviour of samples is a well-known phenomenon.[71–73] On decompression, another phase transition to the intermediate L-cysteine IV (monoclinic form) occurs. Raman spectroscopy of L-cysteine form I[67,74] confirmed that at 3.6 GPa the spectrum was similar to the high-pressure form III in Moggach *et al.*[70] A further transition at lower pressure (1.9 GPa) was different to form I and III, hence could have been that of form IV. On the other hand, DL-cysteine does not possess such a rich polymorphic behaviour; there is only one polymorph known even at high pressures. The solid form accessed at 0.1 GPa was the same form as at low temperature.

In contrast to serine and cysteine, DL- and L-forms of alanine showed no phase transition up to 8.3 GPa.[68,69] An anisotropy of strain is observed in both compounds where the decrease of void space in both DL- and L-structures causes the non-isotropic compression of the unit-cell parameters. Beyond 8.3 GPa, a further study using neutron diffraction has shown that the crystalline phase persists up to 13 GPa before becoming amorphous at 15 GPa.[75,76] The amorphous phase, in this case, becomes crystalline once the pressure is released. Funnell *et al* suggested that the amorphisation of alanine is driven by minimisation of pressure x volume contribution to the free energy of the structure and not due to destabilising contacts. Usually, in organic compounds, the increase of pressure induces a reduction of the voids in the structure since that requires significantly less energy to compress than covalent bonds. In the case of alanine, it is suggested that the rearrangement of the molecules is necessary to access the void space at the expense of the long-range order of the structure.[76]

The effect of pressure in pharmaceutical compounds can reveal nucleation and growth process distinct that the ones observed at atmospheric conditions. For example, chlorpropamide (4-chloro-N-(propylaminocarbonyl)benzenesulfonamide) presents a very rich polymorphic behaviour at atmospheric conditions (five different polymorphs α-ε) that is obtained through different crystallisation methods.[77,78] The β and ε forms present polymorphic transitions through cooling. β form transforms to βII form at 267K following through a new transition to βIII form at 150-125K. While ε form undergoes a phase transition to ε' form at 200K. The same rich polymorphic behaviour is observed by applying pressure. Boldyreva et al. identified transformations in α and β form by applying different pressure transmitting media (PTM).[72,79,80] The phases that have been achieved through pressure are expected to be slight modifications of the

known forms. Many of these phases are observed. Starting from the beta form, the authors observed transformation to the α phase using Neon as the PTM. There was a further transition at high pressure that is commensurate with the observation of the α form using ethanol solution. Interestingly, with helium (a more penetrating medium) there is a transformation to a new β' structure at 0.5 GPa followed by a further transition at ~1 GPa to β''. The first transition is mirrored using paraffin oil as the medium but in the oil the crystal breaks up. At higher pressures (1 GPa), however, the behaviour changes where the helium changes to a new phase (β'') with a fracturing of the crystal whilst the oil undergoes two further phase transitions to different forms (β^{III}_{HP} and β^{IV}_{HP}). In these latter cases, a powder is formed. The authors also investigated seeding experiments where the behaviour alters depending on the seeds present. In this case, the presence of no seeds the γ form is observed whilst the δ form is observed if the α and γ forms are present from the start indicating that the α form is aiding the isolation of the δ form

Piracetam (2-oxo-pyrrolidineacetamide)[81,82] is an analogous compound of Levetiracetam (Lev) and Etiracetam (Eti) without the ethyl group and possesses three polymorphic forms at atmospheric pressure. Form II (triclinic, $P\bar{1}$) and III (monoclinic, $P2_1/n$) have been isolated using cooling crystallisation in 2-propanol from 353 K where different batches produced the two different polymorphs using the same procedure.[83,84] The formation of form I (triclinic, $P\bar{1}$) occurs by increasing the temperature above 400 K. The thermodynamic behaviour of these forms has been described by Picciochi et al.[85] and they found the relative stabilities to be III > II > I at ambient temperature. This was confirmed by Toscani *et al.*[86] who investigated the system with increasing pressure. In addition to these three polymorphic forms, two high-pressure

polymorphic forms were described in the literature. Form IV (monoclinic, $P2_1/c$) was obtained by crystallisation of methanolic and aqueous solutions of piracetam form II at pressure of 0.07 and 0.40 Gpa,[82,87] respectively. Form V (triclinic, $P\bar{1}$) was identified after a transition from the same form in 2-propanol at 0.7 GPa.

Another compound with a rich phase diagram at atmospheric[88] and high-pressure[73] is *p*-aminobenzoic acid (*p*ABA). Cruz-Cabeza et al.[88] investigated the polymorphism behaviour at atmospheric pressure through structural analyse of reported crystal data in Cambridge Structural Database, crystal structure prediction and molecular simulation. The known atmospheric polymorphic forms are α-forms obtained via solvent selections and supersaturation conditions, β-form crystallized at low supersaturation (S < 1.5) solution in water and γ-forms obtained from water in the presence of selenous acid and vapour growth technique. Additionally, Ward et al.[73] reported a high-pressure form of *p*ABA at 0.3 GPa from three different pressure-transmitting media: water, water:ethanol and pure ethanol. This high-pressure form was possible to recover at ambient condition using large volume press (LVP), which allowed the production of enough quantity for thermo- and structural characterisation. Moreover, this form continued to be stable for a few weeks. The recovery at ambient conditions brings the opportunity to analyse high-pressure polymorphic forms using the standard methods of crystal form characterisation, but also the application of high-pressure polymorphic seeds in crystallisations at ambient conditions. Another example of recovery of materials is glycolide. Hutchison *et al*[89] discovered a high-pressure polymorph that was possible to produce in large quantities (300 mg) by LVP. This polymorphic phase was stable for 12 days at ambient condition. All these examples show that is possible to expand our knowledge of phase diagram by applying pressure.

1.6 Synopsis of thesis

In this thesis, we explore the structural features of the RS- and S-forms of 2-(2-Oxo-1-pyrrolidinyl) butyramide (Figure 1.6a &b). The racemic compound, Etiracetam (Eti), possesses two polymorphs at atmospheric pressure.[90] Form I (monoclinic, $P2_1/c$) is stable below 303.5 K and form II (monoclinic, $P2_1/c$) is formed via a suspension of form I in methanol above 313 K. In contrast, despite several crystallisations attempts[91] only one crystalline structure was reported for the S-form, Levetiracetam (Lev).[92] It is interesting to observe that racemic and enantiopure compound that share similar molecules (different conformations) present different polymorphic behaviour. The cocrystallisation of these compounds, in some cases, is possible with the same coformers which allow the use of Lev and Eti as models compound. This system can be used to explore the phase diagrams to improve the conditions of chiral resolution. Also, since piracetam (Figure 1.6c) presents a rich phase diagram at high-pressure, these compounds seem good candidates to study nucleation and to evaluate chiral resolution at high-pressure.

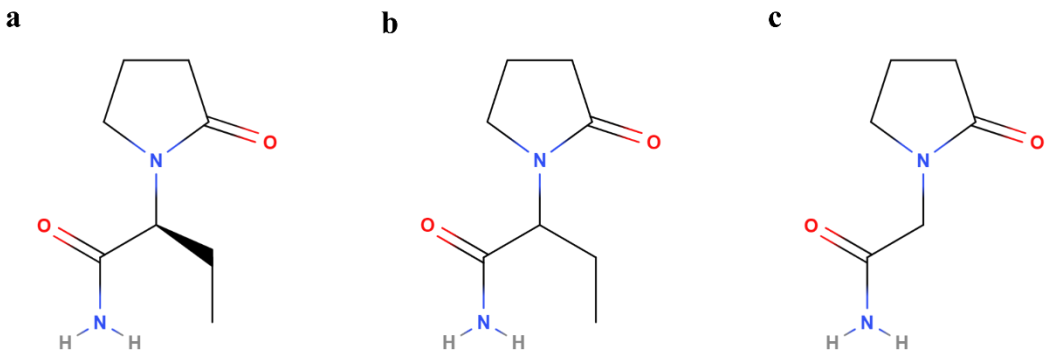

Figure 1.6 – Chemical diagram of **a** Levetiracetam, **b** Etiracetam and **c** piracetam.

In Chapter 2, a brief review is presented for solubility measurements methods and structural characterisation methods, X-ray diffraction and Raman Spectroscopy.

In chapter 3, we analyse the ability of cocrystallisation to modify a chiral phase diagram of the model compounds Eti and Lev (S-(2-(2-oxo-pyrrolidin-1-yl)-butyramide). The chiral system is studied in a selection of solvents using pseudo-binary phase diagrams. Several candidate co-formers are added to the chiral system to promote the formation of cocrystals based on the individual solubility of the components. The oxalic acid cocrystals identified are also studied in a pseudo-binary phase diagram and compared with the initial pseudo-binary phase diagram of the chiral system. The application of cocrystallisation to change the eutectic composition is confirmed to this system, however, the new position of eutectic composition in the cocrystal system represents a small region of enantiopure compound. New strategies are discussed to find a system where the opposite could be observed to enhance methods of chiral resolution.

In chapter 4, we investigate the molecular and crystal structure of Eti and Lev at ambient and high-pressure conditions. The application of pressure highlighted the important role of intermolecular and interlayers interaction for the stability of compounds in the study. The unit cell parameters and intermolecular energies as a function of pressure are analysed to understand the non-linear compression of both compounds. In this system, the hypothesis of spontaneous resolution through high pressure is evaluated by the study of density as a function of pressure.

In chapter 5, our goal to this chapter was to study nucleation in solid crystal to solid crystal transformation at low pressure (p < 1 GPa). The transformations reported to Lev and Eti were at higher pressures and the transitions were very subtle to proceed to a nucleation study using Raman Spectroscopy. For that reason, we changed the system in this work. Hydrochlorothiazide (HCT; Figure 1.7) was selected as a model

compound due to the rich polymorphic behaviour that presents at ambient conditions, also some previous studies in our group indicated a change in the polymorph form on compression. Nucleation process in a transition between solid state is characterized by single crystal-to-single crystal mechanism or through reconstructive mechanisms (where is observed the division of the first polymorph in several crystals by breaking). A reconstructive phase transition was visualized during the compression of HCT where the new polymorphic form was possible to recover at ambient conditions. Consequently, the slow kinetics turns this system unsuitable for nucleation studies. However, the structural behaviour of HCT at low pressure brought the opportunity to manipulate a high-pressure form at ambient conditions.

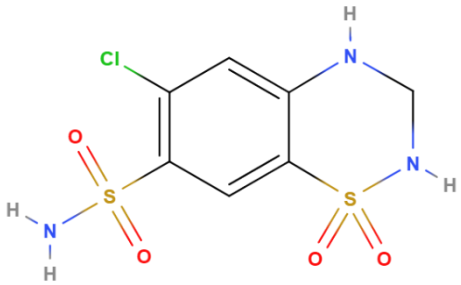

Figure 1.7 - Structural formula of Hydrochlorothiazide

Finally, in Chapter 6 the main findings of this thesis are summarised and future studies that could be explore following the work here discussed.

1.7 References

(1) Chen, J.; Sarma, B.; Evans, J. M. B.; Myerson, A. S. Pharmaceutical Crystallization. *Cryst. Growth Des.* **2011**, *11* (4), 887–895. https://doi.org/10.1021/cg101556s.

(2) ter Horst, J. H.; Schmidt, C.; Ulrich, J. Fundamentals of Industrial Crystallization. In *Handbook of Crystal Growth: Bulk Crystal Growth: Second Edition*; Elsevier, 2015; Vol. 2, pp 1317–1349. https://doi.org/10.1016/B978-0-444-63303-3.00032-8.

(3) Johnston, A.; Bardin, J.; Johnston, B. F.; Fernandes, P.; Kennedy, A. R.; Price, S. L.; Florence, A. J. Experimental and Predicted Crystal Energy Landscapes of Chlorothiazide. *Cryst. Growth Des.* **2011**, *11* (2), 405–413. https://doi.org/10.1021/cg1010049.

(4) Davey, R. J.; Schroeder, S. L. M.; Ter Horst, J. H. Nucleation of Organic Crystals - A Molecular Perspective. *Angew. Chemie - Int. Ed.* **2013**, *52* (8), 2166–2179. https://doi.org/10.1002/anie.201204824.

(5) Ce Nicoud, L.; Licordari, F.; Myerson, A. S. Estimation of the Solubility of Metastable Polymorphs: A Critical Review. **2018**. https://doi.org/10.1021/acs.cgd.8b01200.

(6) Moriyama, K.; Furuno, N.; Yamakawa, N. Crystal Face Identification by Raman Microscopy for Assessment of Crystal Habit of a Drug. *Int. J. Pharm.* **2015**, *480* (1–2), 101–106. https://doi.org/10.1016/j.ijpharm.2015.01.031.

(7) Mealey, D.; Croker, D. M.; Rasmuson, Å. C. Crystal Nucleation of Salicylic Acid in Organic Solvents. *CrystEngComm* **2015**, *17* (21), 3961–3973. https://doi.org/10.1039/c4ce01428f.

(8) Gu, C. H.; Chatterjee, K.; Young, V.; Grant, D. J. W. Stabilization of a Metastable Polymorph of Sulfamerazine by Structurally Related Additives. *J. Cryst. Growth* **2002**, *235* (1–4), 471–481. https://doi.org/10.1016/S0022-0248(01)01784-5.

(9) Black, S.; Dang, L.; Liu, C.; Wei, H. On the Measurement of Solubility. *Organic Process Research and Development*. American Chemical Society March 15, 2013, pp 486–492. https://doi.org/10.1021/op300336n.

(10) Jiang, S.; ter Horst, J. H. Crystal Nucleation Rates from Probability Distributions of Induction Times. *Cryst. Growth Des.* **2011**, *11* (1), 256–261. https://doi.org/10.1021/cg101213q.

(11) Yang, H.; Florence, A. J. Relating Induction Time and Metastable Zone Width. *CrystEngComm* **2017**, *19* (28), 3966–3978. https://doi.org/10.1039/C7CE00770A.

(12) Bernstein, J. Polymorphism − A Perspective. *Cryst. Growth Des.* **2011**, *11* (3), 632–650. https://doi.org/10.1021/cg1013335.

(13) Vippagunta, S. R.; Brittain, H. G.; Grant, D. J. W. Crystalline Solids. *Adv. Drug Deliv. Rev.* **2001**, *48* (1), 3–26. https://doi.org/10.1016/S0169-409X(01)00097-7.

(14) Haleblian, J.; McCrone, W. Pharmaceutical Applications of Polymorphism. *Journal of Pharmaceutical Sciences*. 1969, pp 911–929. https://doi.org/10.1002/jps.2600580802.

(15) Braun, D. E.; Gelbrich, T.; Kahlenberg, V.; Laus, G.; Wieser, J.; Griesser, U. J. Packing Polymorphism of a Conformationally Flexible Molecule (Aprepitant). *New J. Chem.* **2008**, *32* (10), 1677–1685. https://doi.org/10.1039/b805438j.

(16) Bauer, J.; Spanton, S.; Henry, R.; Quick, J.; Dziki, W.; Porter, W.; Morris, J. Ritonavir: An Extraordinary Example of Conformational Polymorphism. *Pharm. Res.* **2001**, *18* (6), 859–866. https://doi.org/10.1023/A:1011052932607.

(17) Saini, A.; Chadha, R.; Gupta, A.; Singh, P.; Bhandari, S.; Khullar, S.; Mandal,

S.; Jain, D. S. New Conformational Polymorph of Hydrochlorothiazide with Improved Solubility. *Pharm. Dev. Technol.* **2015**, *21* (5), 1–8. https://doi.org/10.3109/10837450.2015.1041040.

(18) Maria, T. M. R.; Castro, R. A. E.; Bebiano, S. S.; Ramos Silva, M.; Matos Beja, A.; Canotilho, J.; Ermelinda S Eusébio, M. Polymorphism of Trans-l,4-Cyclohexanediol: Conformational Isomorphism. *Cryst. Growth Des.* **2010**, *10* (3), 1194–1200. https://doi.org/10.1021/cg901160v.

(19) Nangia, A. Conformational Polymorphism in Organic Crystals. *Acc. Chem. Res.* **2008**, *41* (5), 595–604. https://doi.org/10.1021/ar700203k.

(20) Kolesov, B. A.; Mikhailenko, M. A.; Boldyreva, E. V. Dynamics of the Intermolecular Hydrogen Bonds in the Polymorphs of Paracetamol in Relation to Crystal Packing and Conformational Transitions: A Variable-Temperature Polarized Raman Spectroscopy Study. *Phys. Chem. Chem. Phys.* **2011**, *13* (31), 14243–14253. https://doi.org/10.1039/c1cp20139e.

(21) Cruz, P. C.; Rocha, F. A.; Ferreira, A. M. Application of Selective Crystallization Methods to Isolate the Metastable Polymorphs of Paracetamol: A Review. *Org. Process Res. Dev.* **2019**, *23* (12), 2592–2607. https://doi.org/10.1021/acs.oprd.9b00322.

(22) Ruggiero, M. T.; Sibik, J.; Zeitler, J. A.; Korter, T. M. Examination of l -Glutamic Acid Polymorphs by Solid-State Density Functional Theory and Terahertz Spectroscopy. *J. Phys. Chem. A* **2016**, *120* (38), 7490–7495. https://doi.org/10.1021/acs.jpca.6b05702.

(23) Lee, E. H. A Practical Guide to Pharmaceutical Polymorph Screening & Selection. *Asian J. Pharm. Sci.* **2014**, *9* (4), 163–175.

https://doi.org/10.1016/j.ajps.2014.05.002.

(24) Shekunov, B. Y.; York, P. Crystallization Processes in Pharmaceutical Technology and Drug Delivery Design. *J. Cryst. Growth* **2000**, *211* (1), 122–136. https://doi.org/10.1016/S0022-0248(99)00819-2.

(25) Singhal, D.; Curatolo, W. Drug Polymorphism and Dosage Form Design: A Practical Perspective. *Adv. Drug Deliv. Rev.* **2004**, *56* (3), 335–347. https://doi.org/10.1016/j.addr.2003.10.008.

(26) Duggirala, N. K.; Perry, M. L.; Almarsson, Ö.; Zaworotko, M. J. Pharmaceutical Cocrystals: Along the Path to Improved Medicines. *Chem. Commun.* **2016**, *52* (4), 640–655. https://doi.org/10.1039/C5CC08216A.

(27) Silva, J. F. C.; Rosado, M. T. S.; Jasiurkowska-Delaporte, M.; Silva, M. R.; Piedade, M. F. M.; Dryzek, E.; Eusébio, M. E. S. Ordered and Plastic Crystals in the Complex Polymorphism of Pinanediol. *Cryst. Growth Des.* **2019**, *19* (11), 6127–6135. https://doi.org/10.1021/acs.cgd.9b00428.

(28) Nogueira, B. A.; Ildiz, G. O.; Canotilho, J.; Eusébio, M. E. S.; Henriques, M. S. C.; Paixão, J. A.; Fausto, R. 5-Methylhydantoin: From Isolated Molecules in a Low-Temperature Argon Matrix to Solid State Polymorphs Characterization. *J. Phys. Chem. A* **2017**, *121* (28), 5267–5279. https://doi.org/10.1021/acs.jpca.7b05030.

(29) Grčman, M.; Vrečer, F.; Meden, A. Some Physico-Chemical Properties of Doxazosin Mesylate Polymorphic Forms and Its Amorphous State. In *Journal of Thermal Analysis and Calorimetry*; 2002; Vol. 68, pp 373–387. https://doi.org/10.1023/A:1016019214704.

(30) Giovannini, J.; Ter Minassian, L.; Céolin, R.; Toscani, S.; Perrin, M. A.; Louër,

D.; Leveiller, F. Tetramorphism of Fananserine: P, T Diagram and Stability Hierarchy from Crystal Structure Determinations and Thermodynamic Studies. In *Journal De Physique. IV : JP*; 2001; Vol. 11. https://doi.org/10.1051/jp4:20011017.

(31) Braun, D. E.; Gelbrich, T.; Kahlenberg, V.; Tessadri, R.; Wieser, J.; Griesser, U. J. Conformational Polymorphism in Aripiprazole: Preparation, Stability and Structure of Five Modifications. *J. Pharm. Sci.* **2009**, *98* (6), 2010–2026. https://doi.org/10.1002/jps.21574.

(32) Florence, A.T.; Attwood, D. *Physicochemical Principles of Pharmacy*, 5th editio.; Pharmaceutical Press, 2011.

(33) Fernandes, M. A.; Levendis, D. C. Photodimerisation of the A′-Polymorph of: Ortho -Ethoxy- Trans -Cinnamic Acid Occurs via a Two-Stage Mechanism at 343 K Yielding 100% α-Truxillic Acid. *CrystEngComm* **2016**, *18* (38), 7363–7376. https://doi.org/10.1039/c6ce00809g.

(34) AALTONEN, J.; Allesø, M.; Mirza, S.; Koradia, V.; GORDON, K. C.; RANTANEN, J.; Solid Form Screening – A Review. *Eur. J. Pharm. Biopharm.* **2008**, *71* (1), 23–37. https://doi.org/10.1016/j.ejpb.2008.07.014.

(35) Rossi, D.; Gelbrich, T.; Kahlenberg, V.; Griesser, U. J. Supramolecular Constructs and Thermodynamic Stability of Four Polymorphs and a Co-Crystal of Pentobarbital (Nembutal). *CrystEngComm* **2012**, *14* (7), 2494. https://doi.org/10.1039/c2ce06659a.

(36) Leitão, M. L. P.; Canotilho, J.; Cruz, M. S. C.; Pereira, J. C.; Sousa, A. T.; Redinha, J. S. Study of Polymorphism from DSC Melting Curves. Polymorphs of Terfenadine. In *Journal of Thermal Analysis and Calorimetry*; 2002; Vol. 68,

pp 397–412. https://doi.org/10.1023/A:1016023315613.

(37) Saunier, J.; Mazel, V.; Paris, C.; Yagoubi, N. Polymorphism of Irganox 1076®: Discovery of New Forms and Direct Characterization of the Polymorphs on a Medical Device by Raman Microspectroscopy. *Eur. J. Pharm. Biopharm.* **2010**, *75* (3), 443–450. https://doi.org/10.1016/j.ejpb.2010.04.014.

(38) Bolla, G.; Mittapalli, S.; Nangia, A. Pentamorphs of Acedapsone. *Cryst. Growth Des.* **2014**, *14* (10), 5260–5274. https://doi.org/10.1021/cg5010424.

(39) Elder, D. P.; Holm, R.; De Diego, H. L. Use of Pharmaceutical Salts and Cocrystals to Address the Issue of Poor Solubility. *International Journal of Pharmaceutics*. Elsevier B.V. August 30, 2013, pp 88–100. https://doi.org/10.1016/j.ijpharm.2012.11.028.

(40) Trask, A. V.; Motherwell, W. D. S. S.; Jones, W. Physical Stability Enhancement of Theophylline via Cocrystallization. *Int. J. Pharm.* **2006**, *320* (1–2), 114–123. https://doi.org/10.1016/j.ijpharm.2006.04.018.

(41) Schultheiss, N.; Roe, M.; Boerrigter, S. X. M. Cocrystals of Nutraceutical P-Coumaric Acid with Caffeine and Theophylline: Polymorphism and Solid-State Stability Explored in Detail Using Their Crystal Graphs. *CrystEngComm* **2011**, *13* (2), 611–619. https://doi.org/10.1039/c0ce00214c.

(42) Cerreia Vioglio, P.; Chierotti, M. R.; Gobetto, R. Pharmaceutical Aspects of Salt and Cocrystal Forms of APIs and Characterization Challenges. *Advanced Drug Delivery Reviews*. Elsevier B.V. August 1, 2017, pp 86–110. https://doi.org/10.1016/j.addr.2017.07.001.

(43) Wood, P. A.; Feeder, N.; Furlow, M.; Galek, P. T. A.; Groom, C. R.; Pidcock, E. Knowledge-Based Approaches to Co-Crystal Design. *CrystEngComm* **2014**,

16 (26), 5839–5848. https://doi.org/10.1039/c4ce00316k.

(44) Kersten, K.; Kaur, R.; Matzger, A. Survey and Analysis of Crystal Polymorphism in Organic Structures. *IUCrJ*. International Union of Crystallography March 1, 2018, pp 124–129. https://doi.org/10.1107/S2052252518000660.

(45) Sandhu, B.; Sinha, A. S.; Desper, J.; Aakeröy, C. B. Modulating the Physical Properties of Solid Forms of Urea Using Co-Crystallization Technology. *Chem. Commun.* **2018**, *54* (37), 4657–4660. https://doi.org/10.1039/C8CC01144C.

(46) Sanphui, P.; Devi, V. K.; Clara, D.; Malviya, N.; Ganguly, S.; Desiraju, G. R. Cocrystals of Hydrochlorothiazide: Solubility and Diffusion/Permeability Enhancements through Drug–Coformer Interactions. *Mol. Pharm.* **2015**, *12* (5), 1615–1622. https://doi.org/10.1021/acs.molpharmaceut.5b00020.

(47) Allan, D. R.; Clark, S. J. Comparison of the High-Pressure and Low-Temperature Structures of Ethanol and Acetic Acid. *Phys. Rev. B* **1999**, *60* (9), 6328–6334. https://doi.org/10.1103/PhysRevB.60.6328.

(48) Allan, D. R.; Clark, S. J.; Brugmans, M. J. P.; Ackland, G. J.; Vos, W. L. Structure of Crystalline Methanol at High Pressure. *Phys. Rev. B* **1998**, *58* (18), R11809–R11812. https://doi.org/10.1103/PhysRevB.58.R11809.

(49) Allan, D. R.; Clark, S. J.; Dawson, A.; McGregor, P. A.; Parsons, S. Pressure-Induced Polymorphism in Phenol. *Acta Crystallogr. Sect. B* **2002**, *58* (6), 1018–1024. https://doi.org/doi:10.1107/S0108768102018797.

(50) McGregor, P. A.; Allan, D. R.; Parsons, S.; Pulham, C. R. The Low-Temperature and High-Pressure Crystal Structures of Cyclobutanol (C 4 H 7 OH). *Acta Crystallogr. Sect. B Struct. Sci.* **2005**, *61* (4), 449–454.

https://doi.org/10.1107/S0108768105019191.

(51) Moggach, S. A.; Parsons, S.; Wood, P. A. High-Pressure Polymorphism in Amino Acids. *Crystallogr. Rev.* **2008**, *14* (2), 143–184. https://doi.org/10.1080/08893110802037945.

(52) Moggach, S. A.; Parsons, S. High Pressure Crystallography of Inorganic and Organometallic Complexes. In *Spectroscopic Properties of Inorganic and Organometallic Compounds*; Royal Society of Chemistry, 2009; pp 324–354. https://doi.org/10.1039/b715012c.

(53) Fabbiani, F. P. A. A.; Pulham, C. R. *High-Pressure Studies of Pharmaceutical Compounds and Energetic Materials*; The Royal Society of Chemistry, 2006; Vol. 35. https://doi.org/10.1039/b517780b.

(54) Neumann, M. A.; van de Streek, J.; Fabbiani, F. P. A.; Hidber, P.; Grassmann, O. Combined Crystal Structure Prediction and High-Pressure Crystallization in Rational Pharmaceutical Polymorph Screening. *Nat. Commun.* **2015**, *6* (1), 7793. https://doi.org/10.1038/ncomms8793.

(55) Oswald, I. D. H.; Pulham, C. R. Co-Crystallisation at High Pressure - An Additional Tool for the Preparation and Study of Co-Crystals. *CrystEngComm* **2008**, *10* (9), 1114–1116. https://doi.org/10.1039/b805591b.

(56) Oswald, I. D. H.; Lennie, A. R.; Pulham, C. R.; Shankland, K. High-Pressure Structural Studies of the Pharmaceutical, Chlorothiazide. *CrystEngComm* **2010**, *12* (9), 2533. https://doi.org/10.1039/c001355b.

(57) Boldyreva, E. V. CHAPTER 2: High Pressure Crystallography: Elucidating the Role of Intermolecular Interactions in Crystals of Organic and Coordination Compounds. In *Monographs in Supramolecular Chemistry*; 2019; Vol. 2019-

Janua, pp 32–97. https://doi.org/10.1039/9781788013086-00032.

(58) Moggach, S. A.; Oswald, I. D. H. Crystallography Under High Pressures. In *21st Century Challenges in Chemical Crystallography I*; Mingos, D.; Raithby, P., Ed.; Springer, Cham, 2020; pp 141–198. https://doi.org/10.1007/430_2020_70..

(59) Woodall, C. H.; Christensen, J.; Skelton, J. M.; Hatcher, L. E.; Parlett, A.; Raithby, P. R.; Walsh, A.; Parker, S. C.; Beavers, C. M.; Teat, S. J.; et al. Observation of a Re-Entrant Phase Transition in the Molecular Complex Tris(M2-3,5-Diisopropyl-1,2,4-Triazolato-K2 N 1:N 2)Trigold(I) under High Pressure. *IUCrJ* **2016**, *3* (5), 367–376. https://doi.org/10.1107/S2052252516013129.

(60) Bordallo, H. N.; Kolesov, B. A.; Boldyreva, E. V.; Juranyi, F. Different Dynamics of Chiral and Racemic (L- and DL-) Serine Crystals: Evidenced by Incoherent Inelastic Neutron and Raman Scattering. *J. Am. Chem. Soc.* **2007**, *129* (36), 10984–10985. https://doi.org/10.1021/ja073351n.

(61) Moggach, S. A.; Allan, D. R.; Morrison, C. A.; Parsons, S.; Sawyer, L. Effect of Pressure on the Crystal Structure of L-Serine-I and the Crystal Structure of l-Serine-II at 5.4 GPa. *Acta Crystallogr. Sect. B* **2005**, *61* (1), 58–68. https://doi.org/doi:10.1107/S0108768104031787.

(62) Moggach, S. A.; Marshall, W. G.; Parsons, S. High-Pressure Neutron Diffraction Study of L-Serine-I and L-Serine-II, and the Structure of L-Serine-III at 8.1 GPa. *Acta Crystallogr. Sect. B Struct. Sci.* **2006**, *62* (5), 815–825. https://doi.org/10.1107/S010876810601799X.

(63) Johnstone, R. D. L.; Francis, D.; Lennie, A. R.; Marshall, W. G.; Moggach, S.

A.; Parsons, S.; Pidcock, E.; Warren, J. E. High-Pressure Polymorphism in L-Serine Monohydrate: Identification of Driving Forces in High Pressure Phase Transitions and Possible Implications for Pressure-Induced Protein Denaturation. *CrystEngComm* **2008**, *10* (12), 1758–1769.

(64) Wood, P. A.; Francis, D.; Marshall, W. G.; Moggach, S. A.; Parsons, S.; Pidcock, E.; Rohl, A. L. A Study of the High-Pressure Polymorphs of L-Serine Using Ab Initio Structures and PIXEL Calculations. *CrystEngComm* **2008**, *10* (9), 1154. https://doi.org/10.1039/b801571f.

(65) Zakharov, B. A.; Kolesov, B. A.; Boldyreva, E. V. Effect of Pressure on Crystalline L- and Dl-Serine: Revisited by a Combined Single-Crystal X-Ray Diffraction at a Laboratory Source and Polarized Raman Spectroscopy Study. *Acta Crystallogr. Sect. B Struct. Sci.* **2012**, *68* (3), 275–286. https://doi.org/10.1107/S0108768112015960.

(66) Moggach, S. A.; Allan, D. R.; Clark, S. J.; Gutmann, M. J.; Parsons, S.; Pulham, C. R.; Sawyer, L. High-Pressure Polymorphism in L-Cysteine: The Crystal Structures of L-Cysteine-III and L-Cysteine-IV. *Acta Crystallogr. B.* **2006**, *62* (Pt 2), 296–309. https://doi.org/10.1107/S0108768105038802.

(67) Minkov, V. S.; Krylov, A. S.; Boldyreva, E. V.; Goryainov, S. V.; Bizyaev, S. N.; Vtyurin, A. N. Pressure-Induced Phase Transitions in Crystalline L- and DL-Cysteine. *J. Phys. Chem. B* **2008**, *112* (30), 8851–8854. https://doi.org/10.1021/jp8020276.

(68) Tumanov, N. A.; Boldyreva, E. V; Kolesov, B. A.; Kurnosov, A. V; Cabrera, R. Q. Pressure-Induced Phase Transitions in L-Alanine, Revisited. *Acta Crystallogr. Sect. B-Structural Sci.* **2010**, *66*, 458–471.

https://doi.org/10.1107/s010876811001983x.

(69) Tumanov, N. A.; Boldyreva, E. V. X-Ray Diffraction and Raman Study of DL-Alanine at High Pressure: Revision of Phase Transitions. *Acta Crystallogr. Sect. B-Structural Sci.* **2012**, *68* (4), 412–423. https://doi.org/10.1107/s0108768112028972.

(70) Moggach, S. A.; Allan, D. R.; Clark, S. J.; Gutmann, M. J.; Parsons, S.; Pulham, C. R.; Sawyer, L. High-Pressure Polymorphism in <scp>L</Scp> -Cysteine: The Crystal Structures of <scp>L</Scp> -Cysteine-III and <scp>L</Scp> -Cysteine-IV. *Acta Crystallogr. Sect. B Struct. Sci.* **2006**, *62* (2), 296–309. https://doi.org/10.1107/S0108768105038802.

(71) Zakharov, B. A.; Seryotkin, Y. V.; Tumanov, N. A.; Paliwoda, D.; Hanfland, M.; Kurnosov, A. V.; Boldyreva, E. V. The Role of Fluids in High-Pressure Polymorphism of Drugs: Different Behaviour of [Small Beta]-Chlorpropamide in Different Inert Gas and Liquid Media. *RSC Adv.* **2016**, *6* (95), 92629–92637. https://doi.org/10.1039/C6RA17750F.

(72) Seryotkin, Y. V.; Drebushchak, T. N.; Boldyreva, E. V. A High-Pressure Polymorph of Chlorpropamide Formed on Hydrostatic Compression of the [Alpha]-Form in Saturated Ethanol Solution. *Acta Crystallogr. Sect. B* **2013**, *69* (1), 77–85. https://doi.org/doi:10.1107/S0108768112051142.

(73) Ward, M. R.; Younis, S.; Cruz-Cabeza, A. J.; Bull, C. L.; Funnell, N. P.; Oswald, I. D. H. Discovery and Recovery of Delta p -Aminobenzoic Acid. *CrystEngComm* **2019**, *21* (13), 2058–2066. https://doi.org/10.1039/C8CE01882K.

(74) Fu, C.; Dai, C.; Du, B.; Li, P.; Lei, L.; Hu, F.; Jiang, Z. Raman Spectroscopic

Study of Orthorhombic L-Cysteine under Pressure up to 20.2 GPa. *J. Mol. Struct.* **2018**, *1171*, 196–201. https://doi.org/10.1016/j.molstruc.2018.05.061.

(75) Funnell, N. P.; Dawson, A.; Francis, D.; Lennie, A. R.; Marshall, W. G.; Moggach, S. A.; Warren, J. E.; Parsons, S. The Effect of Pressure on the Crystal Structure of L-Alanine. *CrystEngComm* **2010**, *12* (9), 2573–2583. https://doi.org/10.1039/c001296c.

(76) Funnell, N. P.; Marshall, W. G.; Parsons, S. Alanine at 13.6 GPa and Its Pressure-Induced Amorphisation at 15 GPa. *CrystEngComm* **2011**, *13* (19), 5841–5848. https://doi.org/10.1039/C1CE05487B.

(77) Drebushchak, T. N.; Drebushchak, V. A.; Boldyreva, E. V. Solid-State Transformations in the β-Form of Chlorpropamide on Cooling to 100 K. *Acta Crystallogr. Sect. B Struct. Sci.* **2011**, *67* (2), 163–176. https://doi.org/10.1107/S0108768111004290.

(78) Drebushchak, T. N.; Drebushchak, V. A.; Pankrushina, N. A.; Boldyreva, E. V. Single-Crystal to Single-Crystal Conformational Polymorphic Transformation in Tolbutamide at 313 K. Relation to Other Polymorphic Transformations in Tolbutamide and Chlorpropamide. *CrystEngComm* **2016**, *18* (30), 5736–5743. https://doi.org/10.1039/c6ce00764c.

(79) Boldyreva, E. V.; Dmitriev, V.; Hancock, B. C. Effect of Pressure up to 5.5 GPa on Dry Powder Samples of Chlorpropamide Form-A. *Int. J. Pharm.* **2006**, *327* (1–2), 51–57. https://doi.org/10.1016/j.ijpharm.2006.07.019.

(80) Zakharov, B. A.; Goryainov, S. V.; Boldyreva, E. V. Unusual Seeding Effect in the Liquid-Assisted High-Pressure Polymorphism of Chlorpropamide. *CrystEngComm* **2016**, *18* (29), 5423–5428.

https://doi.org/10.1039/C6CE00711B.

(81) Fabbiani, F. P. A.; Allan, D. R.; Parsons, S.; Pulham, C. R. An Exploration of the Polymorphism of Piracetam Using High Pressure. *Crystengcomm* **2005**, *7*, 179–186. https://doi.org/10.1039/b418976k.

(82) Fabbiani, F. P. A. A.; Allan, D. R.; David, W. I. F. F.; Davidson, A. J.; Lennie, A. R.; Parsons, S.; Pulham, C. R.; Warren, J. E. High-Pressure Studies of Pharmaceuticals: An Exploration of the Behavior of Piracetam. *Cryst. Growth Des.* **2007**, *7* (6), 1115–1124. https://doi.org/10.1021/cg0607710.

(83) Admiraal, G.; Eikelenboom, J. C.; Vos, A. Structures of the Triclinic and Monoclinic Modifications of (2-Oxo-1-Pyrrolidinyl)Acetamide. *Acta Crystallogr. Sect. B Struct. Crystallogr. Cryst. Chem.* **1982**, *38* (10), 2600–2605. https://doi.org/10.1107/s0567740882009431.

(84) Bandoli, G.; Clemente, D. A.; Grassi, A.; Pappalardo, G. C. Molecular Determinants for Drug-Receptor Interactions. 1. Solid-State Structure and Conformation of the Novel Nootropic Agent 2-Pyrrolidone-N-Acetamide: X-Ray and Theoretical SCF-MO Studies. *Mol. Pharmacol.* **1981**, *20* (3), 558–564.

(85) Picciochi, R.; Diogo, H. P.; Minas Da Piedade, M. E. Thermodynamic Characterization of Three Polymorphic Forms of Piracetam. *J. Pharm. Sci.* **2011**, *100* (2), 594–603. https://doi.org/10.1002/jps.22294.

(86) Toscani, S.; Céolin, R.; Ter Minassian, L.; Barrio, M.; Veglio, N.; Tamarit, J. L.; Louër, D.; Rietveld, I. B. Stability Hierarchy between Piracetam Forms I, II, and III from Experimental Pressure-Temperature Diagrams and Topological Inferences. *Int. J. Pharm.* **2016**, *497* (1–2), 96–105. https://doi.org/10.1016/j.ijpharm.2015.11.036.

(87) Gonnade, R. G.; Sangtani, E. Polymorphs and Cocrystals: A Comparative Analysis. In *Journal of the Indian Institute of Science*; Springer International Publishing, 2017; Vol. 97, pp 193–226. https://doi.org/10.1007/s41745-017-0028-2.

(88) Cruz-Cabeza, A. J.; Davey, R. J.; Oswald, I. D. H.; Ward, M. R.; Sugden, I. J. Polymorphism in p -Aminobenzoic Acid. *CrystEngComm* **2019**, *21* (13), 2034–2042. https://doi.org/10.1039/C8CE01890A.

(89) Hutchison, I. B.; Bull, C. L.; Marshall, W. G.; Parsons, S.; Urquhart, A. J.; Oswald, I. D. H. Compression of Glycolide-h 4 to 6 GPa. *Acta Crystallogr. Sect. B Struct. Sci. Cryst. Eng. Mater.* **2017**, *73* (6), 1151–1157. https://doi.org/10.1107/S2052520617015657.

(90) Herman, C.; Vermylen, V.; Norberg, B.; Wouters, J.; Leyssens, T. The Importance of Screening Solid-State Phases of a Racemic Modification of a Chiral Drug: Thermodynamic and Structural Characterization of Solid-State Phases of Etiracetam. *Acta Crystallogr. Sect. B Struct. Sci. Cryst. Eng. Mater.* **2013**, *69* (4), 371–378. https://doi.org/10.1107/S2052519213015054.

(91) Xu, K.; Xiong, X.; Guo, L.; Wang, L.; Li, S.; Tang, P.; Yan, J.; Wu, D.; Li, H. An Investigation into the Polymorphism and Crystallization of Levetiracetam and the Stability of Its Solid Form. *J. Pharm. Sci.* **2015**, *104* (12), 4123–4131. https://doi.org/10.1002/jps.24628.

(92) Song, J.; Lou, K. X.; Li, X. J.; Wu, X. P.; Feng, R. X. 2-(2-Oxopyrrolidin-1-Yl)Butyramide. *Acta Crystallogr. Sect. E Struct. Reports Online* **2003**, *59* (11). https://doi.org/10.1107/S1600536803022578.

Chapter 2

Methods

2.1 Measurement of solubilities

The selection of a method to measure solubility depends on the characteristics of the system. Currently, there are two main types of methods for solubility measurement, which are based on either concentration variation or temperature variation.[1,2] The concentration method can be divided into two approaches as shown in Figure 2.1a: 1) the saturation concentration (orange circle) can be determined by analysing a filtered solution after achieving equilibrium with an excess of solid (excess method), and 2) a known amount of solid is added to the initial concentration in steps until the saturation concentration has been reached (addition method). The temperature method is applied by heating a solution with an excess of solid until complete dissolution, which corresponds to the saturation temperature (T_{sat}), as illustrated in Figure 2.1b.

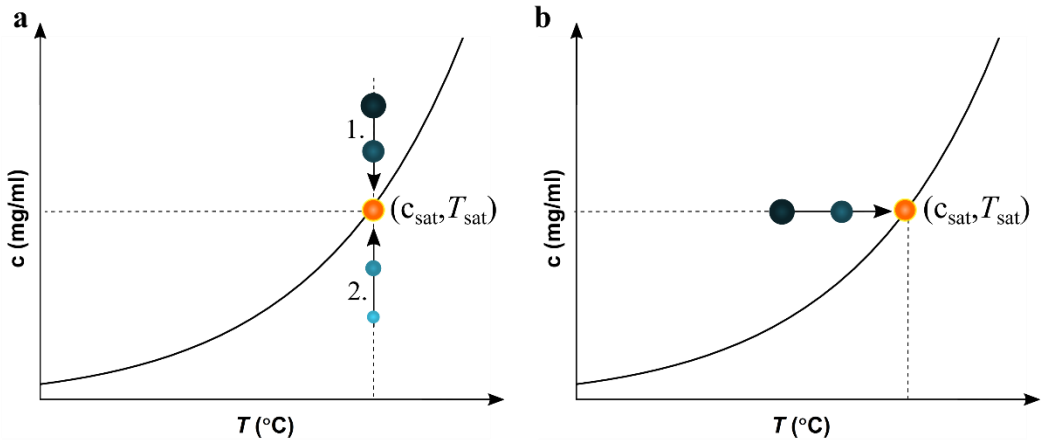

Figure 2.1– Representation of solubility measurements using **a1.** excess method, **a2.** addition method at constant temperature and **b** temperature variation method.

Although the concentration variation method is considered more accurate, this method is often tedious and time-consuming. In contrast, the temperature variation method is gaining visibility due to the possibility of running a higher number of measurements in a shorter period of time and it being less labour intensive. In this study, the Crystal16 (Avantium Technologies)[3] was used to determine solubility. Crystal16 is a multiple reactor system that can accommodate 16 vials (capacity of 1 ml each) with electromagnetic stirring, with the possibility of applying 4 different temperature regimes simultaneously. In this equipment, the solubility is obtained through the measurement of turbidity as a function of temperature. A laser signal is propagated throughout the vials and collected by light sensors at the other end of the reactors. When the transmission is equal to 100% (the first point without detection of particles), the clear point is achieved and the saturation temperature (red circle) is measured, as observed in Figure 2.2. The selection of heating rate is important to secure a fast dissolution and therefore dissolution kinetics can be neglected. In Figure 2.2, the change in the transmission is sharp and well-defined which provides confidence in the measurement of the saturation temperature. The heat-cool cycle enables both the clear point (T_{sat}) and the cloud point (precipitation of solid) to be measured so that a metastable zone width can also be measured for the given experimental parameters. An average of 3 heat-cool cycles has been demonstrated to be the most efficient and accurate measurement of T_{sat} establishing a link between clear temperature and saturation temperature.[4] There are some factors that can impact the accuracy of the measurement, such as solvent evaporation and fouling.

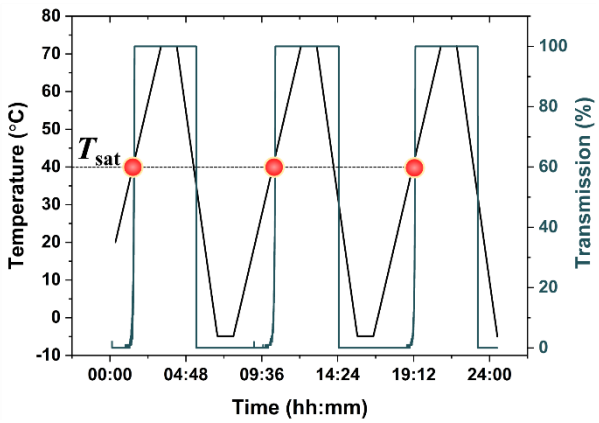

Figure 2.2 – Determination of the saturation temperature (T_{sat}) using Crystal16 equipment through turbidity transmission measurements. If the heating rate is sufficiently small the clear point/temperature (red circle) is equal to T_{sat} hence the light transmission is equal to 100%.

2.2 Diffraction methods

The phenomenon present in diffraction methods are generally scattering of radiation, where ideally there is no absorption of radiation by the sample and the variation of intensity with direction is observed. The source of radiation can be electromagnetic or generated by small particle such neutrons or electrons by deceleration of high-energy electrons or by electronic transitions in the inner orbitals atoms, respectively. In the diffraction experiment, the radiation applied needs to have a wavelength compatible with the size of the sample in study (atoms and molecules), in the range of 10^{-5} to 100 Å, that can be found in electromagnetic in the X-ray region.[5,6]

The process of X-ray diffraction is like that of the scattering of laser light using grating, the typical Young's slit experiment. In that experiment, the grating is the same magnitude as the laser light and it is regularly spaced grating which enables the laser to be refracted into fringes of high and low scattered radiation where constructive and destructive interference between the scattered waves. Critical to this experiment is the

order of the grating. In X-ray diffraction experiments, the light is now X-ray radiation and the 'grating' is the crystal which must have long range order for the process to occur. The crystal is a three-dimensional object hence the scattered radiation is observed as discrete spots that can be measured. The measurement of diffraction pattern is basically a physical scattering of an X-ray beam by the sample, where the scattering pattern is collected and registered by the detector. From these experiments the scattered light possesses two properties that we are able to observe. Firstly, the intensity of the scattered light and secondly the relative position of the diffracted radiation. These two properties enable us to calculate the unit cell parameters and also the position of the atoms. Unfortunately, some of the information in the scattered X-rays are lost when the pattern is recorded which is known as the 'Phase problem' but this can be overcome using a number of techniques to find the atomic coordinates such as direct methods, charge-flipping, Patterson methods and intrinsic phasing. [5–7] Mathematical recombination of the scattered X-rays is performed by a computer using equations that represent the physical process.

The physical scattering is a result of the interference between electric vector of X-rays and the crystalline structure, Figure 2.3. This phenomenon, named diffraction, occurs when the d-spacing between layers of atoms are roughly the same as the wavelength of the radiation (λ_{inc}) and when the scattering centers of the crystal are organized in the regular way (black dots in the Figure 2.3). This process was described by W. H. Bragg in 1912 in Equation 2.1 - Bragg equation. It is important to highlight that only one angle, θ, meet the condition for constructive interference for a given d-spacing expressed in the Equation 2.1.[5]

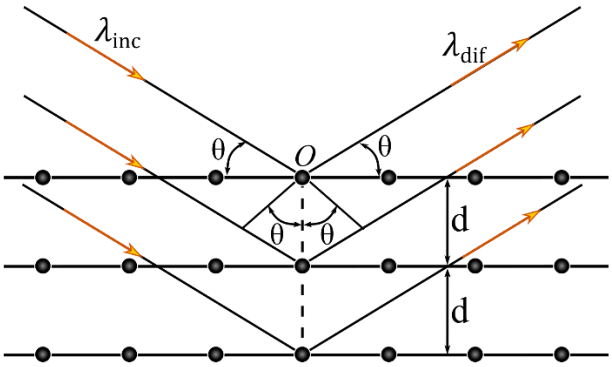

Figure 2.3 – Diffraction of X-ray by a crystal. A X-ray beam (λ_{inc}) strikes the crystal at incident angle θ and it is scattered (λ_{dif}) if the conditions for constructive interference are meet.

$$n\lambda = 2d_{hkl} \sin \theta_{hkl} \qquad \textbf{Equation 2.1}$$

The diffraction experiment provides a three-dimensional observation of the scattered X-rays that are observed in a regular lattice, the spacing between the lattice points depends on the size of the unit cell. The lattice can also be used to identify the symmetry of the crystal system as detailed below.

2.2.1 Lattice and Crystal Systems

A crystalline structure can be described by selecting the small representation of the structure, designated by the unit cell shown in Figure 2.4. This representation is based in the three length vectors *a*, *b* and *c* that are related through three angles α, β and γ, also known as lattice parameters. The infinite repetition of the unit cell in space generates the crystal structure and it is this structure that can be represented by a lattice, where an atom or group of atoms are allocated to every point.

A crystal is characterized by a regular array of molecules that are related with each other by symmetry. There are eight symmetry elements that could define a crystal. The combination of these symmetry elements results in 32 point groups that are the base

of the classification of 7 crystal systems. Furthermore, the crystals systems can be represented by 14 Bravais lattices. The relationship between the crystal systems and the Bravais lattices is shown in Figure 2.5. The classification of crystals is even more detailed, since the identification of screw axis and glide reflection divide the crystals in 230 space groups.

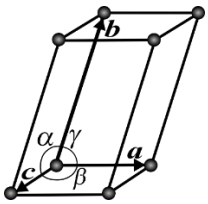

Figure 2.4 – Scheme of an unit cell.

		Bravais lattices				
		Parameters	Simple (*P*)	Body centered (*I*)	Base centered (*C*)	Face centered (*F*)
Crystal Systems	Triclinic	$a \neq b \neq c$ $\alpha \neq \beta \neq \gamma$				
	Monoclinic	$a \neq b \neq c$ $\alpha \neq \gamma = 90° \neq \beta$				
	Orthorhombic	$a \neq b \neq c$ $\alpha = \beta = \gamma = 90°$				
	Tetragonal	$a = b \neq c$ $\alpha = \beta = \gamma = 90°$				
	Trigonal	$a = b = c$ $\alpha = \beta = \gamma \neq 90°$				
	Cubic	$a = b = c$ $\alpha = \beta = \gamma = 90°$				
	Hexagonal	$a = b \neq c$ $\alpha = \beta = 90°; \gamma = 120°$	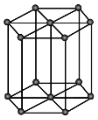			

Figure 2.5 – The fourteen Bravais lattices

2.2.2 Lattice Planes

The lattice planes are described by using Miller indices (*h k l*). This is the way that with can relate planes used in the Bragg equation with the unit cell. By definition, Miller indices are the reciprocals of the fractional coordinates of the plane that intercept the crystallographic axes. These planes are not solid planes that reflect light as might be suggested by the Bragg illustration in Figure 2.3, but are a useful way to help in the description of the crystal structure. For example, the (2 0 0) Miller index would be defined as a plane that is located at a =1/2 and would be parallel to the *bc*-plane, shown in Figure 2.6a. The (3 0 2) Miller index would be defined as a plane that crosses at a = 1/3 and c= 1/2 but would never cross the *b*-axis, illustrated in Figure 2.6b. These can be imagined in any orientation to cut through the unit cell and a consequence of this is that the higher the integer value in the Miller index the smaller the *d*-spacing between the planes, therefore they provide greater spatial resolution for identification of the structure. In the diffraction experiments, we assign Miller indexes to every collected scattered intensity which is the process of indexing. At this point, it may be useful to describe the diffraction experiment and the way in which data is processed.

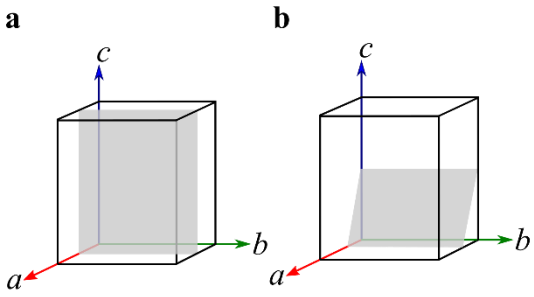

Figure 2.6 – Representation of Miller indexes(in grey) for **a** (2 0 0) plane and **b** (3 0 2).

2.2.3 Crystal structure determination

We start a diffraction measurement by putting a single crystal in the goniometer, this part of the diffractometer allows the rotation of the crystal in all the position for a full collection set of diffraction data. As we discussed, the X-rays interact with the repeating pattern of atoms (or more precisely, the electrons) resulting in the diffraction of X-rays. From the position and intensities of the diffraction data we can establish the crystalline structure. If the crystal is aligned with the X-ray beam, it possible to know the position of the reflections collected by the detector (Figure 2.7a). The reflections are observed in a reciprocal lattice plot (lattice of the diffraction pattern) represented in the Figure 2.7b that show a regular array of the reflections in a plane perpendicular to the *b**-direction. This representation can be assigned to the unit cell lengths, *a*=9.46 Å*: b*=7.67 Å*: c*=11.44 Å, the primitive lattice that describe the crystal structure. The process of indexing allows us to assign (*h k l*) values to every reflection so that we can relate to the unit cell.

In the process of integration, it is possible to determine the intensity of the reflections by drawing boxes around the reflections and counting the amount of photons present in each reflection. The intensity of the reflection is proportional to the number of electrons that is present in a specific Miller plane that are scattering the X-rays. We measure the diffracted intensity (I_{hkl}) from which we can obtain the $F_{hkl.}$ via the square root of intensity. From structure factor equation, Equation 2.2, *F*(*hkl*) is simply sum of the structure factors of each atom in unit cell:

$$F(h\ k\ l) = \sum_{n=1}^{N} f_n \exp[2\pi i(hx_n + ky_n + lz_n) \qquad \textbf{Equation 2.2}$$

where f_n is the atomic scattering factor for the *N* atom in the unit cell. f_n varies as a function of diffraction angle.

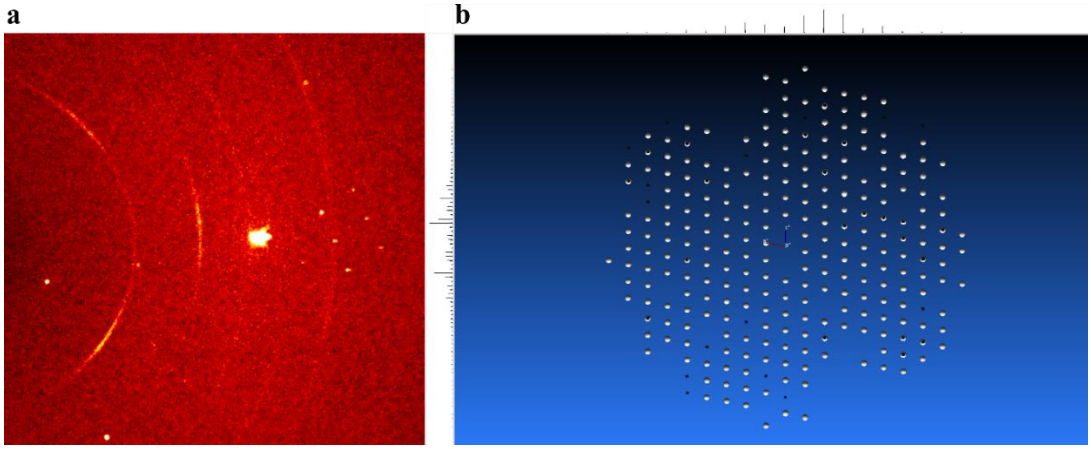

Figure 2.7 – Information obtained in a X-Ray diffraction experiment from a single crystal in diamond anvil cell (DAC): **a** frame of diffraction where is visible diffraction of the crystal (discrete sharp points), diffraction of diamonds (large point at the middle of the image) and gasket diffraction (yellow semi-cycles) and **b** reciprocal lattice plot for the (0 1 0) view.

Each of the atoms in structure will scatter a wave as a result of the interaction between the X-rays photon and the electrons in the structure. The scattering of each atom may or may not be in the phase with the another depending on their relative positions to one another. The only scattering from the crystal where the scattering waves are in phase with each other is when the value is 0. Unfortunately, this position is in the same place as the direct beam which makes this information unavailable to us. Every other scattered intensity will have a magnitude, that we can measure, however the relative phases of the scattered waves are lost. This is known as the 'Phase Problem'. The electron density that describes the scattering of the crystal is given by the reverse *Fourier transform* of the diffraction pattern. From the Equation 2.3, it is possible to obtain the electron density (ρ (xyz)), however, it requires both intensity and wave phase. F_{hkl} is determined by square root of intensity (I_{hkl}) but there no any information of the phase (ϕ_{hkl}), and therefore we cannot access the structure.

$$\rho(xyz) = \int_{cell} \frac{1}{V} \sum_{h,k,l} |F(hkl)| exp[i\phi(hkl)] exp[-2\pi i(hx + ky + lz)] \qquad \textbf{Equation 2.3}$$

We can tackle the 'Phase Problem' through structural solution such as direct methods and 'charge flipping' or by using a reference known model obtained in previous diffraction experiments. During the successful structure solution, we obtain values of the phase that can be input in the Equation 2.3 to provide chemical reasonable solution to the electron density (or crystal structure). Conversely, random allocations of phases will lead to electron density map that does not give a chemical reasonable structure. From the structure solution, we now have a model from which with can now calculate the intensity and the phase. In Equation 2.4, it is applied the electron density and calculate the diffraction pattern using the forward *Fourier Transform*.

$$F(hkl) = \int_{cell} \rho(xyz).\exp[2\pi i(hx + ky + lz)dV \qquad \textbf{Equation 2.4}$$

From the diffraction pattern, it is observed intensities and from the structure solution we have a model from which we calculate a diffraction pattern. This allows us to be able to measure how well the model can fit the diffraction pattern from our crystal. This measure is known as *R* factor:

$$R = \frac{\Sigma||F_{obs}|-|F_{cal}||}{\Sigma|F_{obs}|} \qquad \textbf{Equation 2.5}$$

The *R* factor represents a difference in the magnitude of observed and calculated magnitude divided by the observed magnitude from each observed intensities. As the difference of this magnitude decreases, the R factor decreases, which it is a consequence of the improvement of the approximation of the model to the diffraction pattern.

2.2.4 Crystal structure refinement

The model can be improved be adding parameters but ensuring that we do not neglect our knowledge of the molecular structure and chemically reasonable behaviour. In the refinement it is possible to include thermal motion of the atoms (setting the atoms to anisotropic conditions), add hydrogens and apply an extinction factor (to correct the reduction in the diffracted intensity due the orientation of the crystal with the respect to the direct beam). Each of these parameters bring us closer to the true structure given by the experiment however we may need help to achieve this.

Constraints can be applied to reduce the parameters to refine, either by relating one parameter with others or by fixing an exact value to the parameter, e.g. setting the phenyl group conformation (bond lengths = 1.390Å; angles = 120°). These are strict hence their use has to be limited to ensure chemical reasonable behaviour. Phenyl ring constraints are often used but for good diffraction data their use may be questionable. Restraint information is applied by attributing meaningful estimates to the parameter or by creating a dependence between parameters, e.g. bond lengths or by changing the direction of atoms vibration to be perpendicular to the bond direction (RIGU restraint). The application of restraints allows the conversion of the parameter to a value that suits the model and is based on the diffraction experiment, in contrast to the use of constraints where the value is fixed. Both refinements strategies are very useful to applied in disorder structure or reduced data sets as in high-pressure experiments.[7]

2.2.5 X-ray powder diffraction

The X-ray powder diffraction has the same principles to single crystal X-ray diffraction. However, X-ray powder diffraction presents two-dimensional data where the existence of peak overlaps and preferred orientation are an issue. Peak overlaps cause difficulty in assigning intensities for each peak therefore causing trouble in structure refinement. Preferred orientation results in specific peaks having greater or less relative intensity compared with the rest of the diffraction pattern which also impacts the structural refinement.[7]

Moreover, the quality of signal-to-noise ratio is higher in the single X-ray diffraction. For these reasons, the single crystal X-ray diffraction is often desirable, since it allows to obtain an unambiguous solution of structure.

2.3 High-pressure

High pressure research is now widespread among several topical areas. High-pressure is used in the synthesis of novel material as superhard materials[8], nanoporous materials[9] and MOFs[10]. For a long time, it has been used in planetary science[11] and physics to simulate processes occurring in the Earth's core, which could help to understand phenomena observed at the surface. High-pressure is also being applied in food industry to conserve food through pasteurisation e.g. orange juice and guacamole have been preserved using this method. It is thought the use of pressure preserves the taste of the food in contrast to heat treatment. In the pharmaceutical industry, the study of active pharmaceutical ingredients (APIs) at high-pressure has been growing. It is a thermodynamic factor that can help to understand intermolecular and intramolecular interactions present in the crystal structure, may induce different path of phase

transitions as well as amorphisation[12] of crystalline samples. High-pressure experiments also can simulate conditions when the materials are exposed to pressure conditions (e.g. tabletting and extrusion).

The range of pressure in the study depends of composition of the sample and the condition that we want to simulated. For example, in geosciences to explore the compounds that may be in Earth's core the pressure could reach hundreds GPa. In contrast, organic compounds have only really been investigated in the range of 0-10 GPa.

2.3.1 Diamond anvil cell

The use of diamond anvil cell (DAC) allows to generate pressure in the system and observe *in-situ* structural modifications by the use of microscopy (Figure 2.8a), spectroscopy and X-ray diffraction. The DAC is constituted by two plates that support two diamonds (in opposite configuration) that will be use to compress the materials shown in Figure 2.8b&c. Due to the transparency of diamonds, the radiation can pass through them almost with little interaction.

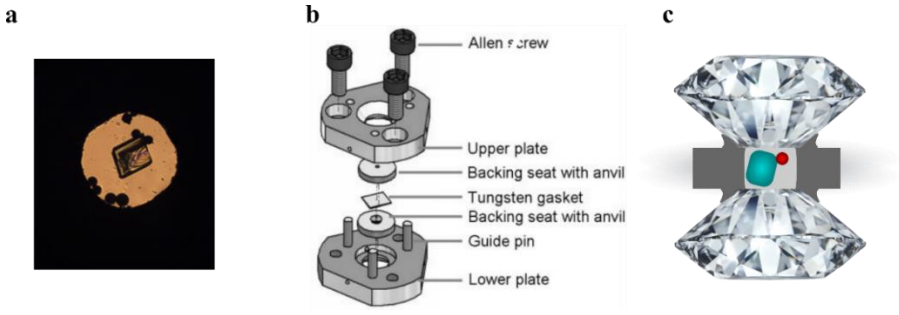

Figure 2.8 – Pressure generation experiment using a DAC. **a** the loading of the cell is performed under a microscopy and it is possible to observe the system (ruby in black and crystal in the image centre); **b** the design of a DAC consists in two steel plates each one with a backing seat with anvil. In the beginning of the experiment, a gasket is placed between the diamonds and squeeze until an indentation is created. In the middle of the gasket, a hole is drilled that will accommodate **c** the material in study (in blue), the pressure transmitting medium (in light grey) and a ruby (in red).

The physical principle behind the DAC is the application of force in a small area, the use of small culets (200-300 μm) could active pressure large than 50 GPa. In the Figure 2.8, it is represented a Merrill–Bassett DAC[13] where the force is applied in the diamonds by tightening the screws. There are several factors that can affect the performance of the device, such as backing plates materials[14], diamonds purity, culet size (tip of the diamond)[15], DAC opening, hole size and thickness, and gasket material. In the preparation to the experiment, a gasket is compressed until the gasket is only 80-100 μm thick and a 200-300 μm hole drilled in its centre. At this point, the set up device is ready. These measurements are dependent of the diamonds culets selection because it will determine both the maximum pressure and the dimensions of the hole.

The DAC loading of the cell has three main elements that could change depending the sample in study and the objective of the experiment. In the sample loading, the hole gasket will act as a chamber for sample, pressure transmitting medium (PTM) and ruby (pressure reader). The sample could be in different forms: single crystal, powder, liquid or gas. The PTM should be inert compound that secures the compression of the sample in hydrostatic condition[16] or could be a solution that allows the *in-situ* crystal growth[17–19]. Furthermore, the selection of PTM can favour the transformation of the compounds (e.g. polymorphism)[20,21] or indeed prohibit change.

2.3.2 Collect diffraction data using a DAC

The advances in the X-ray diffraction sources, detectors and goniometer have increase the quality of diffraction data in high-pressure experiments. However, the challenges continue to exist due to interaction of the DAC with the X-ray beam. The diamonds are large single crystal hence interact with the X-ray radiation and their

diffraction is observed in the experiments. This is shown in centre of the diffraction pattern in Figure 2.7a (bright white large spot). The gasket in the DAC set-up can also diffract the incident beam (this effect is illustrated in Figure 2.7a where is observed semi-rings in the diffraction pattern). A further issue, is the DAC blocks a large amount of radiation from the incident beam and from the scattered waves by the sample. Figure 2.9 shows this effect highlighted in the reciprocal lattice of a single-crystal of same compound on a fibre (Figure 2.9a) compared with one in the DAC (Figure 2.9b). The reciprocal lattice shape changes from a sphere to a donut shape due to the reduction of data, as a result of radiation blocked by the cell body of the DAC. This reduction in the data can be quite severe with the completeness of the data being reduced to 30% for triclinic systems.

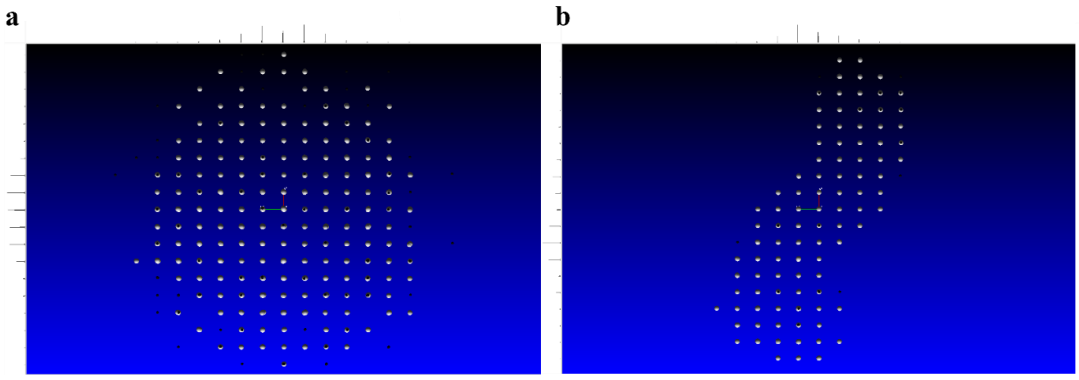

Figure 2.9 – Reciprocal lattice plot from (0 0 1) view for compound A when **a** the crystal is mounted on a fiber and **b** the crystal is inside the diamond anvil cell.

2.3.3 Ruby signal

The pressure inside the DAC can be determined by the use of internal standard materials whose changes in physical properties with pressure are known. These materials are loaded together with the sample in the chamber (gasket hole). The selection of the pressure marker material depends on the pressure range, the measuring

method and the experimental condition (e.g. temperature). The most widely applied standard material to measure the pressure is ruby using the fluorescence signal, Figure 2.10. The relation between applied pressure and wavelength shift of the R-line emission from the ruby is known as ruby pressure gauge. This emission is formed by two peaks, the R1-line and R2-line that show similar behaviour in a hydrostatic pressure but different response in nonhydrostatic conditions[22]. As consequence, only most intense R1-line is selected for pressure calibration. Here, in this thesis, we follow the linear equation developed by Piermarini et al.[23] through calibration of the pressure using R1-line ruby emission to pressure below 19.5 GPa, expressed in the Equation 2.6:

$$P[GPa] = 0.2753(\pm 0.0014)\,\Delta\lambda \qquad \textbf{Equation 2.6}$$

where *P* is pressure and Δλ (Å) is the ruby R1-shift at 298K.

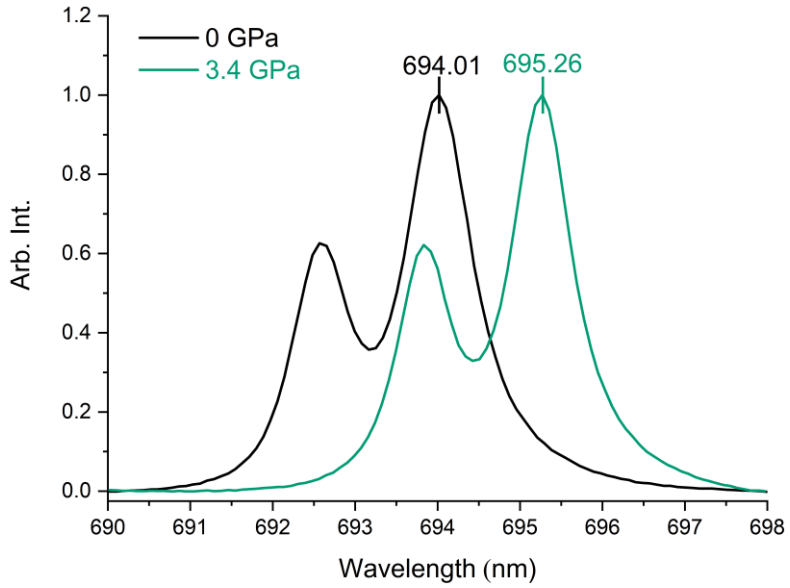

Figure 2.10 – Florescence of ruby gauge at ambient condition collected using Raman spectroscopy. The ambient condition and high-pressure (3.4 GPa) at 298K is represent in black and green plot, respectively.

The advances in X-ray diffraction methods and the increase of pressure ranges make imperative the redefinition of the Equation 2.6 for pressure up to 150 GPa. In 2020, the Executive Committee of AIRAPT proposed the Equation 2.7 (referred as Ruby2020) to analyse the relation between pressure and the ruby gauge, where λ_0 is the wavelength of the R1-line near 694.25 nm at ambient condition.[24] The utilization of Equation 2.7 has since been recommended to allow the data to be directly compared across laboratories.

$$P[GPa] = 1.87(\pm 0.01) \times 10^3 \left(\frac{\Delta\lambda}{\lambda_0}\right)[1 + 5.63(\pm 0.03)]\left(\frac{\Delta\lambda}{\lambda_0}\right) \qquad \textbf{Equation 2.7}$$

2.4 Raman spectroscopy

In 1928, C.V. Raman discovered that the wavelength of small fraction of the scattered radiation by certain molecules differs from the wavelength of incident radiation. He also concluded that the shift in the wavelength is related with the chemical structure of the irradiated molecule. He was award in 1930 with the Novel Prize in physics for this discovery and works in this area.[25]

Raman spectroscopy is based in the same type of quantized vibrational changes that are associated to infrared absorption but uses inelastic scattering of light to probe these states. For both methods, the difference in wavelength between the incident and scattered radiation corresponds to wavelengths in the middle-infrared region. These techniques are known to be complimentary, due to fact that some groups are only active in Raman and others in infrared.

Raman scattering occurs due to the interaction of the electrical field of the radiation with the electronic cloud of the sample. However, the vibration is only Raman active if the interaction induces a momentary polarizability of the bond. If the bonds vibrate

in a way that the distortion of the vibration mode is difficult (lower polarizability), the vibration is Raman inactive, e.g. asymmetrical vibration of carbon dioxide. This is an example where the vibration is Raman inactive but infrared active, because the distortion of the bond does not cause a change in the polarizability however there is a change in the dipole moment.

Raman spectrum is achieved due to the interaction between a laser beam of ultraviolet, visible or infrared monochromatic radiation and the sample. During the experiment, the spectrum of scatted radiation is measured. It is represented by intensity as function of wavenumber shift, which is the difference between the scattered radiation and the incident radiation ($\Delta\bar{\nu} = \bar{\nu}_{incident} - \bar{\nu}_{scattered}$), however, to simplify the x-axis is labelled as wavenumber rather than wavenumber shift.

The process of irradiation and scattering is illustrated in the energy level diagram in Figure 2.11.[25] The photon from the source will provide an energy equal to *hv* to the molecule, illustrated by the couple arrows at the left of the phase diagram. Depending of the frequency of the radiation, the molecule could be excited to any virtual state between the ground electronic state and the lowest excited electronic state. The wider arrow at the left represents the interaction of a photon with molecule that is in a fundamental level of the ground electronic state. At the ambient condition, the molecules normally occupy this state, however, a small quantity could be in the first vibrational level of the electronic ground state, represented by the second arrow at the left.

The next arrows in the energy level diagram illustrate the process of scattering from the molecule. The middle of the diagram depicts the most common scattering, known as Rayleigh scattering. This process is characterized by the unchanged energy

involved in the electronic excitation and scattering, in this case the photon-molecule interaction is known as elastic. In opposite, the Stoke and the anti-Stoke emissions (Raman scattering) happens when there is a gain (+ΔE) or a loss of energy (-ΔE), respectively, known as inelastic scattering. Due to the relative low population of the first level of the ground electronic energy state, the anti-Stokes emission has a considerably lower probability to occur than Stokes emission. By convention, the Stoke peaks are represented at right and anti-Stoke at the left of the origin in the Raman spectra. Both have the same wavelength shift that is related by $\pm \Delta E$. The ratio of anti-Stoke and Stoke intensities with variation of temperature can serve as *in-situ* temperature probe. The increase of temperature will increase the electronic population of the to the first level of the ground electronic state. As a consequence, the probability of anti-Stoke emission will increase and therefore the ratio anti-Stoke and Stoke intensities for the same vibrational mode also increases.

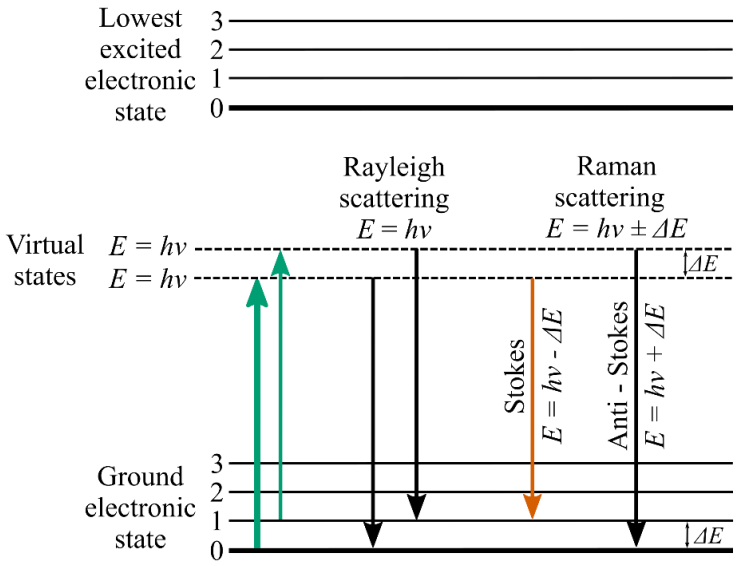

Figure 2.11 - Energy level diagram showing excitation, Rayleigh and Raman scattering. Adapted from Skoog et al.[25]

In high-pressure studies, Raman spectroscopy is a support technique to X-ray diffraction.[26] The quick screening of pressure using Raman spectroscopy provide a highlight of pressure regions where a transformation of the material may be happening.[27] However, the assignment of the measured Raman band to a phase transformation needs to be confirmed by X-ray, since the modification of the Raman spectrum is often ambiguous[28,29]. The Raman spectra is very specific for a compound, mainly in at low wavenumber region (<500 cm^{-1}) where the lattice structure contributes. The analysis of Raman spectra also can yield important information about weak interactions as hydrogen bonding or breathing modes, which are will be altered with different polymorphs. A modification of Raman spectrum (e.g. disappearing or appearing of a peak) may be associated to a change in the crystalline structure, such as phenomena as phase transition and decomposition.

In a compression study, the increase of the density of the material is evidenced through a shift of the wavenumber to the right, which is related with the increase in the frequency of vibrations in a reduced volume. Then, if this behaviour is not observed during compression, the sample could be approaching a phase transformation (e.g. a denser phase) or the system has achieved the limit of pressure for the DAC setup. Additionally, a Raman spectrum for a sample in a DAC presents a characteristic peak at 1335 cm^{-1} due to the scattering of the diamond, this effect is shown in Figure 2.12.

The techniques highlighted here are used together in this thesis to analyse the changes in the systems under a range of temperature and pressure conditions. They provide complementary evidence on various timescales that has helped us to understand the changes to our system.

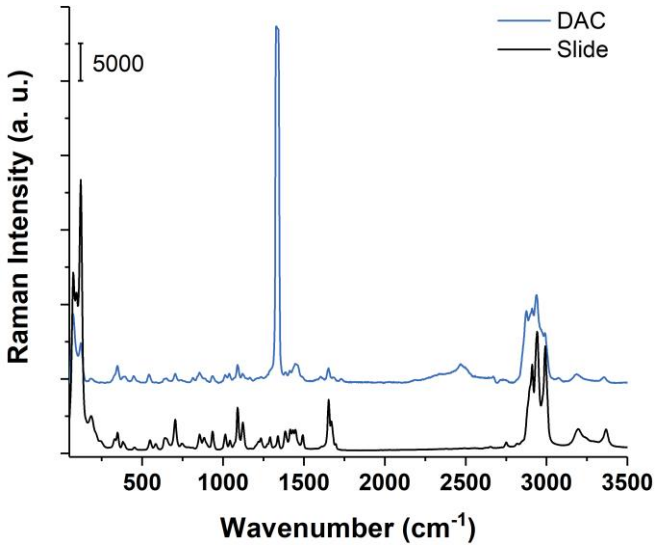

Figure 2.12 – Raman spectra of single-crystal of Levetiracetam at 0 GPa in a DAC and on top of a microscope slide.

2.5 References

(1) Reus, M. A.; van der Heijden, A. E. D. M.; ter Horst, J. H. Solubility Determination from Clear Points upon Solvent Addition. *Org. Process Res. Dev.* **2015**, *19* (8), 1004–1011. https://doi.org/10.1021/acs.oprd.5b00156.

(2) Lorenz, H. Solubility and Solution Equilibria in Crystallization. In *Crystallization: Basic Concepts and Industrial Applications*; Wiley-VCH Verlag GmbH & Co. KGaA: Weinheim, Germany, 2013; pp 35–74. https://doi.org/10.1002/9783527650323.ch3.

(3) Crystal16 - Crystallization Systems https://www.crystallizationsystems.com/crystal16 (accessed Nov 9, 2020).

(4) Vellema, J.; Hunfeld, N. G. M.; Van den Akker, H. E. A.; ter Horst, J. H. Avoiding Crystallization of Lorazepam during Infusion. *Eur. J. Pharm. Sci.* **2011**, *44* (5), 621–626. https://doi.org/10.1016/j.ejps.2011.10.010.

(5) Waseda, Y.; Matsubara, E.; Shinoda, K. *X-Ray Diffraction Crystallography*; Springer Berlin Heidelberg, 2011. https://doi.org/10.1007/978-3-642-16635-8.

(6) Giacovazzo, C.; Monaco, H. L.; Artioli, G.; Viterbo, D.; Milanesio, M.; Gilli, G.; Gilli, P.; Zanotti, G.; Ferraris, G.; Catti, M. *Fundamentals of Crystallography*; Giacovazzo, C., Ed.; Oxford University Press, 2013. https://doi.org/10.1093/acprof:oso/9780199573653.001.0001.

(7) Clegg, W.; Blake, A. J.; Cole, J. M.; Evans, J. S. O.; Main, P.; Parsons, S.; Watkin, D. J. *Crystal Structure Analysis: Principles and Practice*; Oxford University Press, 2009; Vol. 9780199219. https://doi.org/10.1093/acprof:oso/9780199219469.001.0001.

(8) Solozhenko, V. L.; Gregoryanz, E. Synthesis of Superhard Materials. *Mater. Today* **2005**, *8* (11), 44–51. https://doi.org/10.1016/S1369-7021(05)71159-7.

(9) MacHon, D.; Pischedda, V.; Le Floch, S.; San-Miguel, A. Perspective: High Pressure Transformations in Nanomaterials and Opportunities in Material Design. *J. Appl. Phys.* **2018**, *124* (16), 160902. https://doi.org/10.1063/1.5045563.

(10) Paseta, L.; Potier, G.; Sorribas, S.; Coronas, J. Solventless Synthesis of MOFs at High Pressure. *ACS Sustain. Chem. Eng.* **2016**, *4* (7), 3780–3785. https://doi.org/10.1021/acssuschemeng.6b00473.

(11) Wang, Z.; Cui, H.; Hou, J.; Dong, X. Can HHe+ Exist at High Pressure: Exploration of High Pressure Induced HF–He Compounds. *Geosci. Front.* **2021**, *12* (2), 1039–1043. https://doi.org/10.1016/j.gsf.2020.03.010.

(12) Guan, J.; Daljeet, R.; Kieran, A.; Song, Y. Pressure-Induced Amorphization and Reactivity of Solid Dimethyl Acetylene Probed by *in Situ* FTIR and Raman Spectroscopy. *J. Phys. Condens. Matter* **2018**, *30* (22), 224004. https://doi.org/10.1088/1361-648X/aabeac.

(13) Merrill, L.; Bassett, W. A. Miniature Diamond Anvil Pressure Cell for Single Crystal X-ray Diffraction Studies. *Rev. Sci. Instrum.* **1974**, *45* (2), 290–294. https://doi.org/10.1063/1.1686607.

(14) Moggach, S. A.; Oswald, I. D. H. Crystallography Under High Pressures. In *21st Century Challenges in Chemical Crystallography I*; Mingos, D.; Raithby, P., Ed.; Springer, Cham, 2020; pp 141–198. https://doi.org/10.1007/430_2020_70.

(15) Ballaran, T. B.; Kurnosov, A.; Trots, D. Single-Crystal X-Ray Diffraction at Extreme Conditions: A Review. *High Pressure Research*. 2013, pp 453–465. https://doi.org/10.1080/08957959.2013.834052.

(16) Klotz, S.; Chervin, J. C.; Munsch, P.; Le Marchand, G. Hydrostatic Limits of 11 Pressure Transmitting Media. *J. Phys. D-Applied Phys.* **2009**, *42* (7), 7. https://doi.org/10.1088/0022-3727/42/7/075413.

(17) Fabbiani, F. P. A. A.; Allan, D. R.; David, W. I. F. F.; Davidson, A. J.; Lennie, A. R.; Parsons, S.; Pulham, C. R.; Warren, J. E. High-Pressure Studies of Pharmaceuticals: An Exploration of the Behavior of Piracetam. *Cryst. Growth Des.* **2007**, *7* (6), 1115–1124. https://doi.org/10.1021/cg0607710.

(18) Fabbiani, F. P. A. A.; Pulham, C. R. High-Pressure Studies of Pharmaceutical Compounds and Energetic Materials. *Chem. Soc. Rev.* **2006**, *35* (10), 932. https://doi.org/10.1039/b517780b.

(19) Oswald, I. D. H.; Pulham, C. R. Co-Crystallisation at High Pressure - An Additional Tool for the Preparation and Study of Co-Crystals. *CrystEngComm* **2008**, *10* (9), 1114–1116. https://doi.org/10.1039/b805591b.

(20) Boldyreva, E. V.; Shakhtshneider, T. P.; Ahsbahs, H.; Sowa, H.; Uchtmann, H. Effect of High Pressure on the Polymorphs of Paracetamol. *J. Therm. Anal. Calorim.* **2002**, *68* (2), 437–452. https://doi.org/10.1023/A:1016079400592.

(21) Drebushchak, T. N.; Drebushchak, V. A.; Boldyreva, E. V. Solid-State Transformations in the β-Form of Chlorpropamide on Cooling to 100 K. *Acta Crystallogr. Sect. B Struct. Sci.* **2011**, *67* (2), 163–176. https://doi.org/10.1107/S0108768111004290.

(22) Chai, M.; Michael Brown, J. Effects of Static Non-Hydrostatic Stress on the R Lines of Ruby Single Crystals. *Geophys. Res. Lett.* **1996**, *23* (24), 3539–3542. https://doi.org/10.1029/96GL03372.

(23) Piermarini, G. J.; Block, S.; Barnett, J. D.; Forman, R. A. Calibration of the Pressure Dependence of the R 1 Ruby Fluorescence Line to 195 Kbar. *J. Appl. Phys.* **1975**, *46* (6), 2774–2780. https://doi.org/10.1063/1.321957.

(24) Shen, G.; Wang, Y.; Dewaele, A.; Wu, C.; Fratanduono, D. E.; Eggert, J.; Klotz, S.; Dziubek, K. F.; Loubeyre, P.; Fat'yanov, O. V.; et al. Toward an International Practical Pressure Scale: A Proposal for an IPPS Ruby Gauge (IPPS-Ruby2020). *1. Shen, G. al. Towar. an Int. Pract. Press. scale A Propos. an IPPS ruby gauge (IPPS-Ruby2020). High Press. Res. 40, 1–16 (2020).High Press. Res.* **2020**, *40* (3), 1–16. https://doi.org/10.1080/08957959.2020.1791107.

(25) Skoog, D. A.; Leary, J. J. *Principles of Instrumental Analysis*, 4th Editio.; Saunders golden sunburst series; Saunders College Pub., 1992.

(26) Boldyreva, E. V. Combined X-Ray Diffraction and Raman Spectroscopy Studies of Phase Transitions in Crystalline Amino Acids at Low Temperatures and High Pressures: Selected Examples. *Phase Transitions* **2009**, *82* (4), 303–321. https://doi.org/10.1080/01411590902838656.

(27) Goncharov, A. F. Raman Spectroscopy at High Pressures. *Int. J. Spectrosc.* **2012**, *2012*, 1–16. https://doi.org/10.1155/2012/617528.

(28) Schmitt, M.; Popp, J. Raman Spectroscopy at the Beginning of the Twenty-First Century. *J. Raman Spectrosc.* **2006**, *37* (1–3), 20–28. https://doi.org/10.1002/jrs.1486.

(29) Tumanov, N. A.; Boldyreva, E. V. X-Ray Diffraction and Raman Study of DL-Alanine at High Pressure: Revision of Phase Transitions. *Acta Crystallogr. Sect. B-Structural Sci.* **2012**, *68* (4), 412–423. https://doi.org/10.1107/s0108768112028972.

Chapter 3

Phase Diagrams of Chiral Cocrystal Systems for Exploring Chiral Resolution Potential

3.1 Abstract

Crystallisation of chiral compounds results in the majority of the cases in the formation of racemic compounds. Commonly, the separation of pure enantiomers is performed through chromatography, a powerful and versatile technique but less amenable to large-scale separations therefore likely to be more expensive. The application of cocrystallisation to the separation of chiral target compounds eases the scalability of chiral resolution processes. In this study, the phase diagram of a chiral target compound has been conducted using the racemic, RS-(2-(2-oxo-pyrrolidin-1-yl)-butyramide, and pure enantiomer, S-(2-(2-oxo-pyrrolidin-1-yl)-butyramide, compounds in different solvent systems. A change in the eutectic composition was investigated using cocrystallisation with oxalic acid by altering the molar fractions of pure enantiomer and observing the saturation temperature. The oxalic acid cocrystal system shows a shift towards a higher eutectic composition. In this case, the higher eutectic composition gives a smaller region in which the chiraly pure cocrystal can be isolated. Despite the eutectic composition moving in the wrong direction, this study demonstrates that cocrystallisation is a valid method to alter the phase diagram of chiral compounds to potentially enhance their resolution.

3.2 Introduction

Enantiomers are stereoisomers that are non-superimposable mirror images of each other and can be key to affecting a physiological response in patients, Figure 3.1.[1] Louis Pasteur in 1848[2] observed crystals of sodium ammonium salts of tartaric acid which were mirror-symmetrical pairs.[3] After manual separation into the two different crystals groups, Pasteur verified that one group of dissolved crystals rotated polarized light clockwise (+) and the other group rotated polarized light counterclockwise (-). This is a way to designate enantiomers, nowadays the enantiomers can also be known as (D) or (L) commonly applied to sugars and amino acids, or (R) or (S). Most of physical and chemical properties of the pure enantiomers are identical (e.g., solubility and melting point).

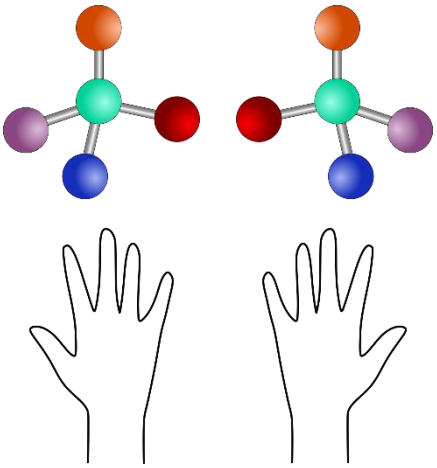

Figure 3.1 – A pair of enantiomers where four different substituents are bound to a chiral center (sphere in light blue). Comparison with hands that as enantiomers are nonsuperimposable mirror images of each other.

In contrast with nature, that tends to be homochiral, the synthesis of enantiomers generally generates both forms in an approximately equal ratio (a racemic solution has an enantiomeric excess of 0 %).[4] When crystallized from a racemic solution usually

both enantiomers are present in the crystalline structure, known as racemic compound, Figure 3.2a.[5] However, the homochiral receptors of biomolecules in the body ensure that the chirality of pharmaceutical compounds plays an important role in the therapeutic effect.[1,6] In extreme cases, a racemic mixture can even cause serious undesired side-effects in the body. Examples are thalidomide a drug where the R-enantiomer has a sedative effect on pregnant women while the S-enantiomer causes birth defects (reported in the 1960s)[7]; also levodopa[6] and penicillamine[7], where only the S-enantiomers exhibits therapeutic behaviour and the counter-enantiomers provoke secondary effects or toxicity. Whilst the racemisation of compounds in the body or physiological fluid cannot be changed, such as in the case of thalidomide, we can influence the initial drug product. Hence, by controlling the enantiomer content in the pharmaceutical product and in absence of racemization in the body, the pharmaceutical product will have the desired positive therapeutic effect. To avoid the undesired effects of the counter-enantiomer, the pharmaceutical industry has prioritised the application of pure single enantiomers in the drug formulation.[8] In general, the production process of pure enantiomers can be obtained via two approaches: (a) enantioselective synthesis using asymmetry synthesis (e.g. chiral building blocks or asymmetric catalysis) and (b) nonselective synthesis and subsequent chiral separation using methods such as chromatography, enantioselective membranes or crystallisation.[9,10]

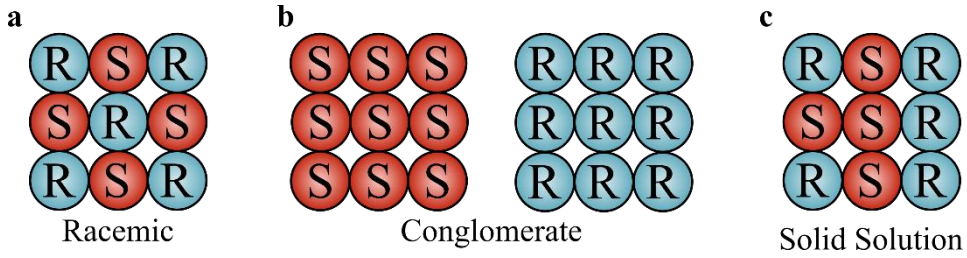

Figure 3.2 – Schematic representation of **a** racemic, **b** conglomerate and **c** solid solution compounds. R-enantiomers are illustrated in blue circles and S-enantiomers in red circles.

Crystallisation is an important technique applied to separate chiral compounds and consequently purify them. In the majority of the cases for chiral systems the goal is the enrichment in the desired enantiomer.[11] The knowledge of the solid-liquid equilibria (SLE) is crucial to understand the maximum achievable yield, purity and the stability of the chiral system.[4] The SLE is represented in the phase diagram as a function of composition, temperature, and pressure. At constant pressure and temperature, a chiral system of enantiomers and solvent can be characterized in the form of a ternary phase diagram, a solubility phase diagram, where lower corners are attributed to pure single enantiomers (R- and S-) and the top corner to pure solvent. There are three main classes of ternary phase diagrams of chiral system: racemic, conglomerate and solid-solution.[12,13] The complexity of these diagrams will increase with the additional compounds added to form salts, solvates or cocrystals but for clarity we will focus on simpler systems, Figure 3.3.[4,14] These phase diagram show the compositional regions where only the isolated single enantiopure crystal phase is in equilibrium and where both enantiopure phases are in equilibrium with the solution.

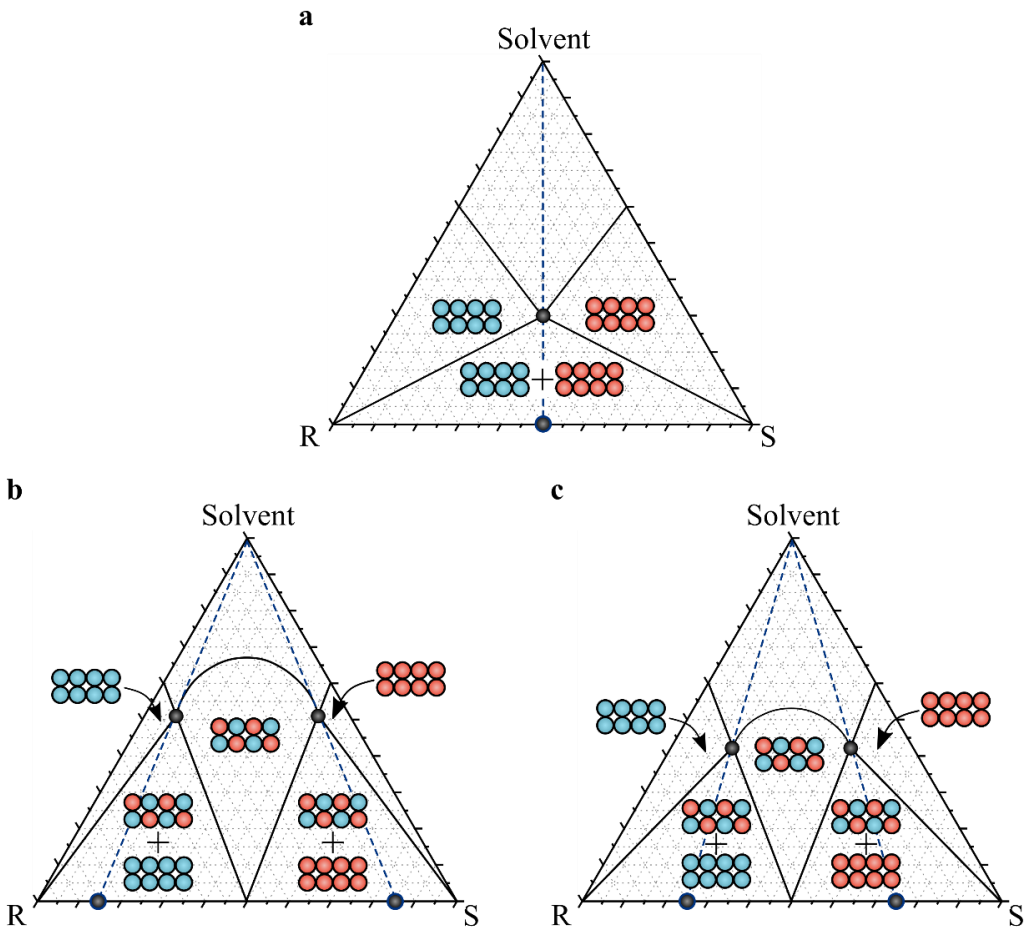

Figure 3.3 – Isothermal equilibrium ternary phase diagram for **a** conglomerate and racemic systems: **b** higher eutectic composition and **c** lower eutectic composition. The composition of the stable solid phases in each region is illustrated in red for S-enantiomer and in blue for R-enantiomer. The eutectic point and composition are represented by a black circle.

For the goal of chiral resolution, it is desirable that the enantiomers crystallize as conglomerates for the direct application of preferential crystallisation.[9,15–17] Conglomerates are a physical mixture constituted by single pure enantiomer crystals, Figure 3.2b and Figure 3.3a. The process of enantiomer resolution by preferential crystallisation starts by use of enantiopure seed crystals which induce the crystallisation of the desired crystals. However, as consequence of crystallisation, the solution will be progressively enriched with the counter enantiomer. The continuation

of this process will end up with a physical mixture of both pure enantiomer crystals where the yield is 50% although the yield can be increased through methods[9,10] such as Viedma ripening[18].

There are rare cases less than 1% where both enantiomers are organized randomly in the solid structure forming a solid solution, Figure 3.2c.[4,19] Most commonly, in around 90% of the cases, crystallisation from a racemic solution leads to the formation of racemic compound.[4] A racemic compound is a mixture of enantiomers in a 50:50 composition where the enantiomers interact to form a crystal structure. Two cases of phase diagram are illustrated in Figure 3.3b and c. The important constituents of the phase diagram for chiral resolution are the eutectic points (black points). The eutectic points are found in the intersection of the solubility isotherm of the racemic and the enantiomeric species. In terms of solubility, these points correspond to the highest solubility where the racemic and the enantiopure solid compounds can co-exist in equilibrium with a solution. As illustrated, the position of eutectic points highlights the composition beyond which the crystallisation of the single pure enantiomer crystals can takes place. Note that if we can somehow alter the eutectic composition from Figure 3.3b to c we are increasing the area of phase space in which the pure enantiomer is formed. This can be exploited in crystallisation-enhanced chiral separation processes to more easily obtain enantiopure products in larger yields.

The knowledge of eutectic composition in a chiral phase diagram is important to describe the enantiopure crystal regions. The use of cocrystallisation can be applied to change physical properties of the chiral compounds by the addition of a coformer compound to create a new crystals structure.[20] At constant pressure (atmospheric pressure) and temperature, the addition of a coformer to the chiral system increases the

complexity from a three- to a four-dimensional system which is extremely challenging. To aid our analysis, we have simplified this problem by scanning phase behaviour as a function of enrichment at constant solvent and co-former composition. In this case, the phase diagram can be defined as a temperature-composition pseudo-binary phase diagram, similar to a previously proposed by Weiwei et al.[21,22] workflow, following a solubility-based cocrystal screening method using a achiral coformer.[19,23]

In this work, we selected racemic compound Etiracetam ((RS)-2-(2-oxo-pyrrolidin-1-yl)-butyramide) (Eti) and Levetiracetam ((S)-2-(2-oxo-pyrrolidin-1-yl)-butyramide) (Lev) to understand if cocrystallisation can be applied as method to modify the phase diagram to enhance chiral resolution using an achiral coformer. Firstly, we determined the phase diagram of the chiral system in selected solvents. Secondly, we crystallized the cocrystals and determined its solubility. Finally, we have constructed and analysed the cocrystal phase diagram.

3.3 Experimental procedure

3.3.1 Material

S-2-(2-oxopyrrolidin-1-yl) butanamide (Levetiracetam, Lev) and, (RS)-2-(2-oxopyrrolidin-1-yl) butanamide (Etiracetam, Eti) were purchased from Xiamen Top Heath Biochem Tech. The solvents acetonitrile and acetone were provided by VWR chemicals, and ethyl acetate acquired from Sigma-Aldrich. The co-former oxalic acid (OA) anhydrous was purchased from Fluka Analytical.

3.3.2 Solubility measurements

Saturation temperatures (T_S) were determined using the Crystal16 instrument (Technobis B.V.) following the temperature variation method developed by ter Horst et al.[24] The equipment is based on the transmission of light through a sample that detects whether the sample is a suspension (transmission smaller than 100%) or a clear solution (transmission equal to 100%).

A sample of known composition was prepared by weighing the solids and solvent into a 1 mL HPLC vial after which a stirrer bar was added. Firstly, the suspensions with known concentration were subjected to a pre-treatment by increasing the temperature at 0.5°C·min^{-1} from room temperature to approximately 10°C below the boiling point of the solvent. The samples were held at this temperature for 1 hour to confirm the total dissolution of the sample. The sample was cooled to -5°C at 0.3 °C·min^{-1} and held at this temperature for 1 hour to allow the crystallisation of material. The heating rate (0.3 °C·min^{-1}) was selected slow enough to assume the saturation temperature to be equal to the determined clear point temperature of the sample composition. The two heating-cooling cycles were performed using the same parameters as the pre-treatment to determine the clear point temperature of the sample. The clear point temperature is the temperature at which a suspension turns into a clear solution, upon heating (i.e. the temperature at which the transmission of light becomes 100%). This methodology was applied to determine the solubility of pure compounds and also to mixed samples compositions. The instrument was calibrated (tuned) at the beginning of the experiment with samples containing water. All clear solution samples measured were colourless and transparent.

3.3.3 X-ray powder diffraction

The temperature profile used in the solubility measurements were replicated in Crystalline equipment (Technobis B.V.) on a slightly larger scale of around 3 ml to obtain sufficient cocrystal material for X-ray powder diffraction (XRPD) analysis. The cocrystal material was collected from the Crystalline vial and dried using filter paper. The samples were analysed without grinding to ensure the absence of phase transformations during this step albeit if the solid was a solvate, desolvation could have potentially occurred. The X-ray scans were carried out on a Bruker D8 Advance II diffractometer configured in Debye–Scherrer transmission geometry. The instrument was equipped with a Cu source (λ = 1.5406 Å) used in conjunction with a $K\alpha_1$ Johansson monochromator and 1 mm anti-divergence slit. A Vantec 1D detector was used together with 2.5° Soller slits. The samples were supported in a multiwell stage with a single layer of Kapton film. The collection was performed at room temperature. The diffraction patterns were analysed using Pawley fitting and Rietveld refinement using TOPAS software (Academic, V5).[25]

3.4 Results

In this work, pseudo-binary phase diagrams[19] are used to structure and simplify the determination of a quaternary phase-diagram for the chiral compound 2-(2-Oxo-1-pyrrolidinyl) butyramide) with a coformer in a selected solvent. The reason behind this approach is due to the characteristics of a quaternary phase-diagram; a system consisting of four components would require analysis in four dimensional space. The determination of a quaternary phase diagram is very expensive (time and resource intense). The use of pseudo-phase diagrams mitigates this and allows the visualization

in two dimensions and the understanding of the changes to solid states induced by the coformer presence.

The exploration of a chiral cocrystalline phase diagram can be executed in three steps[23]: (1) determination of the pure component solubility of enantiopure (Lev), racemic compound (Eti) and coformer (binary system); (2) determination of the solubility of various ratios of enantiomer mixtures (Eti + Lev + solvent; ternary system); (3) determination of the solubility of mixed compositions of chiral compounds and coformer (Eti + Lev+ coformer + solvent; quaternary system) which could give rise to the formation of cocrystal compound. This progression in complexity will enable the comparison of a ternary pure chiral phase diagram with a quaternary cocrystal phase diagram where the eutectic composition may vary due to the change in solids of the system. Here we are in particular interested in the change in eutectic composition.

3.4.1 Solubility of Levetiracetam and Etiracetam

We selected three solvents that are commonly used in the chemical industry: acetone, ethyl acetate and acetonitrile. Figure 3.4 presents a typical profile of light transmission in time when applying a temperature profile for Eti and Lev in the different solvents. The red and green lines represent the dissolution of Eti and Lev in the solvents detected by the increase of light transmission; then saturation temperature is the temperature at which the transmission becomes 100%. The signal of light transmission is very reliable and consistent for acetonitrile with sharp changes to the transmission (Figure 3.4a). For example, the measurement of clear point for Eti in

acetonitrile (c = 309.1 mg·ml^{-1}) is at 63.4 °C (Time = 2h39), 58.9 °C (Time =11h00) and 58.4°C (Time = 19h24).

In contrast, acetone and ethyl acetate show a greater amount of fluctuation for the Lev data which hinders the determination of the solubility. (Figure 3.4b & c). The reason of this variability could be due to a crowning layer just above the liquid level observed in the vials during the measurements. Upon heating, the crowning layer detaches and suspends in the sample solution increasing density of suspension and lowering transmission. Crowning also decreases overall solution concentration and therefore might lead to lower clear point temperatures if a crowning layer does not detach. For this reason, acetonitrile was the solvent selected to continue the investigation of phase diagrams for chiral cocrystals.

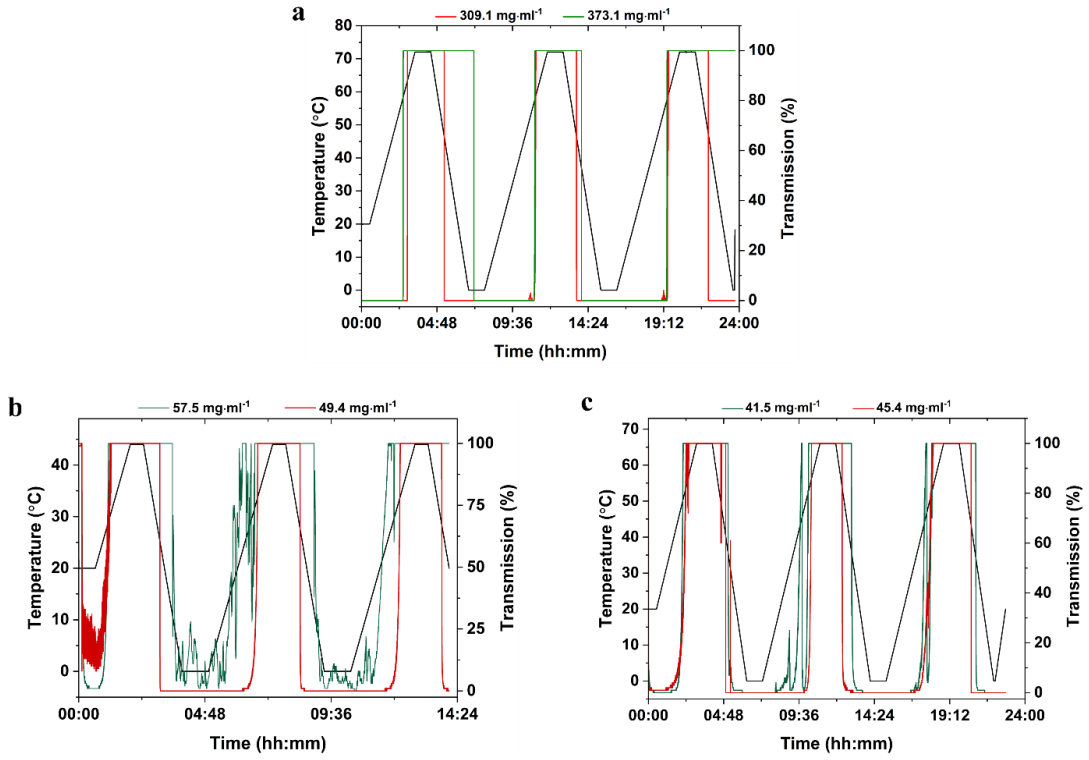

Figure 3.4 - Temperature cycles (black) and typical light transmission signals in time during solubility measurements of Lev (green) and Eti (red) in **a** acetonitrile, **b** acetone, and **c** acetate ethyl acetate**.** The labels on top of the graphs indicate the concentration of Lev or Eti used in the measurement.

It is possible to estimate solubility as function of temperature by applying the van 't Hoff equation for multicomponent solids to the experimental solubility data:

$$\sum_{i}^{N} \ln x_i = -\frac{\Delta H}{R}\left(\frac{1}{T_S} - \frac{1}{T_0}\right) \qquad \textbf{Equation 3.1}$$

where x_i is the molar fraction of the components i, presenting in the solid phase, N is the total number of components i, ΔH (enthalpy change on dissolution in J·mol^{-1}) and T_S (saturation temperature in K) are parameters specific for each solubility line derived from experimental data. The application of the van 't Hoff equation to Lev and Eti in acetonitrile showed a good fit of the experimental data (Figure 3.5a). The solubility of Lev and Eti in acetonitrile at low temperature is very similar, however, as the temperature is increased the difference between the solubility of these compounds becomes greater.

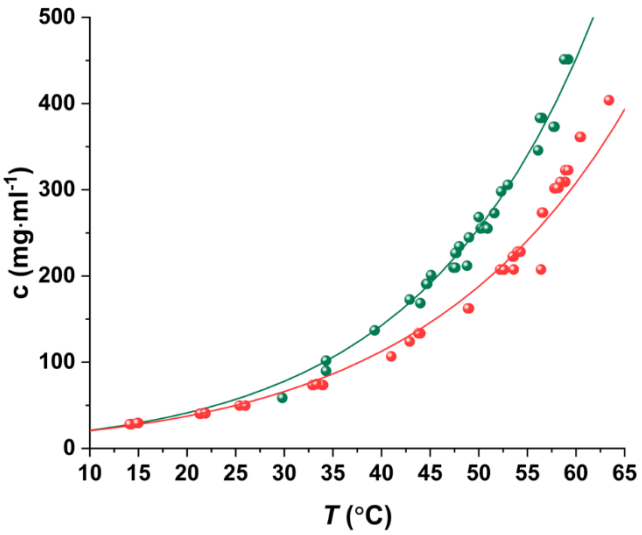

Figure 3.5 - Solubility curves for Lev (green) and Eti (red) in **a** acetonitrile b acetone **c** ethyl acetate.

Using the linear form of the van 't Hoff equation we are able to visualize the solubility data in a different way and estimate solubility at different temperatures:

$$\ln x = \frac{A}{T_m} + \mathrm{B} \qquad \textbf{Equation 3.2}$$

where A = -$\Delta H/R$ and B = $\Delta H/RT_m$ are fitting parameters. Applying Equation 3.2 to the solubility data of Lev and Eti we can achieve a linear fit to the data (Figure 3.6). The data gathered using acetonitrile is well-described, and the *R*-square value equal to 0.99 for both compounds. From this representation we are able to interpolate or extrapolate solubility of the Lev and Eti at other temperatures, which is crucial to the construction of the pseudo-phase diagrams and theoretical solubility lines.

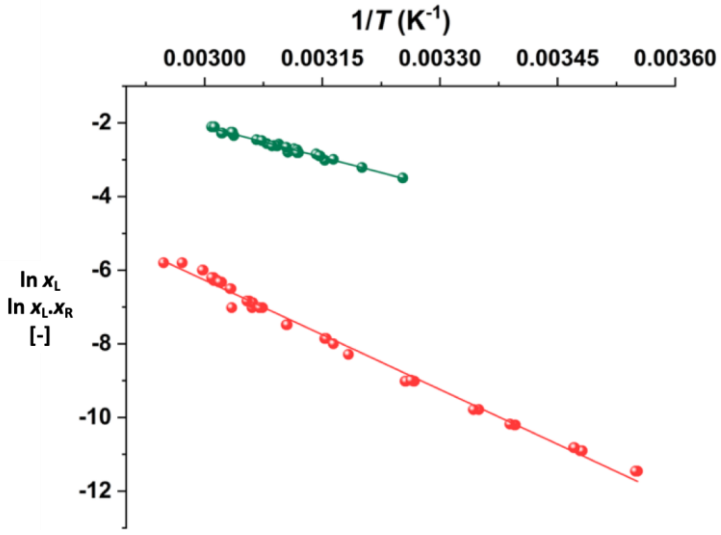

Figure 3.6 – Solubility curves of Lev (in green) and Eti (in red) in acetonitrile presented as van 't Hoff plot.

It was found in the literature that both Lev and Eti crystallize out in the form of cocrystals with oxalic acid (OA), 2,4-dihydrobenzoic acid (DHBA), 2,2-dimethylsuccinic acid (DMSA) and 4-nitrobenzoic acid (NBA) using the grinding method.[26] The successful formation of these cocrystals provides us four potential systems to move the eutectic and consequently enabling the chiral resolution of Eti. Through our experience of crystal engineering, we added malonic acid (MA) and

succinic acid (SA) to the list of potential co-formers due to presence of a similar rigid carboxylic chain observed in OA.

From the data presented in Figure 3.7, it is clear that most of the co-formers are described well by the van 't Hoff equation with exception of SA. A broad range of concentration were used to measure the solubility of SA from 791 to 16007 mg·ml^{-1}. The measured clear points were not precise. For example, for one of two sample of SA with a composition of 791 mg·ml^{-1}, the compound did not crystallize during the experiment, while for the second sample a clear point of 16.3 °C (in the 2nd temperature cycle) and 4.2 °C (in the 3rd temperature cycle) were obtained. The observed variation in the clear point measurements may find its origin in polymorph or solvate formation or it might be that crystallisation kinetics are very slow in these systems. [27]

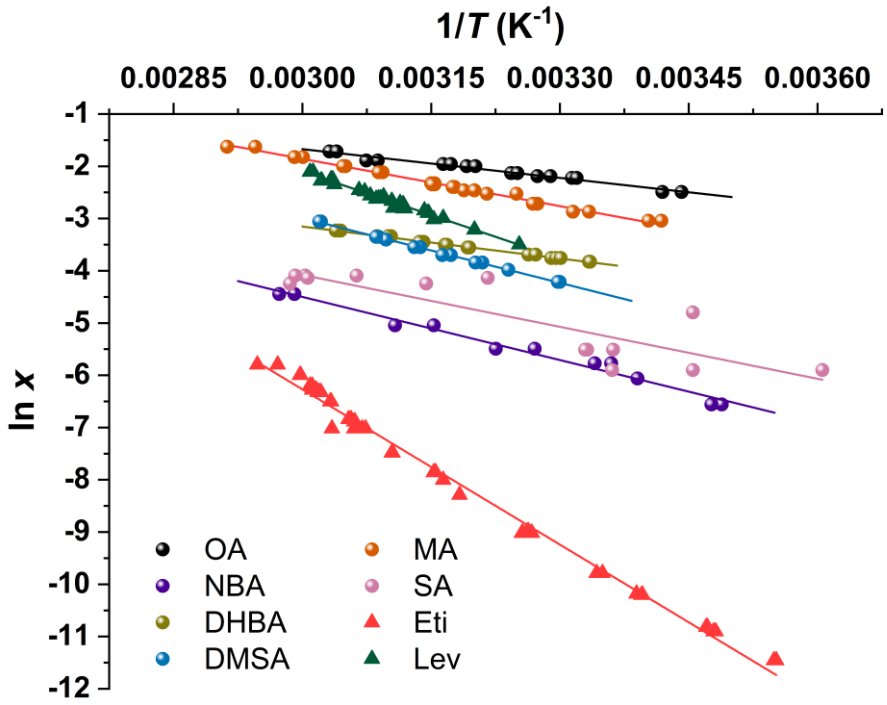

Figure 3.7 - Solubility curves of Lev (in green) and Eti (in red) and **a** co-formers OA (in black), NBA (in violet), DHBA (in olive), DMSA (in blue), MA (in orange) and SA (in pink) in acetonitrile.

3.4.2 Formation of cocrystals

We decided to select a solution method in which the cocrystal screening is based on thermodynamic factors such as pure component solubilities rather than following the conventional molar stoichiometry of the cocrystal.

The formation of cocrystals from solution was investigated using Nehm et al [28], who proposed that the solubility of cocrystal can be expressed as a product of the component concentrations. Ter Horst et al[23] developed a methodology assuming that at a fixed temperature, the individual solubility of starting material is unaffected by the presence of each other and the solubility of cocrystals is expressed as solubility product of starting compounds. The solubility of Eti or Lev (x_A) and co-formers (x_B) are then the key to define the region where the cocrystal is stable. If the cocrystal is more stable than its individual compounds, then the solubility (dash grey line) will be lower than the mixture of its individual compounds (black circle), Figure 3.8. These solubility data allowed us to select the optimum composition to favour the formation of cocrystal.

The cocrystal formation is confirmed by the measurement of saturation temperatures of a mixture containing a chiral compound (in pure enantiomer or racemic form) with a coformer. These temperatures are compared to a reference temperature (T_{REF}) defined by the solubility of the individual component at a specific temperature. If the saturation temperature measured for the mixture is 10°C above the T_{REF} (T- T_{REF} >10°C), it signifies that the formation of a new compound is a high possibility. The results from the solubility measurements were confirmed by X-ray powder diffraction data.

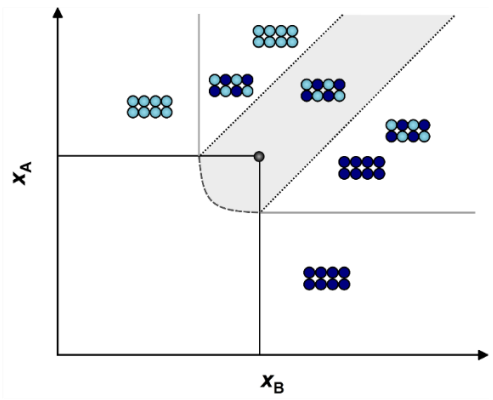

Figure 3.8 – Schematic isothermic phase diagram of AB cocrystal where the region of formation of crystal A (light blue circles), crystal B (dark blue circles), and AB cocrystal (dark and light blue combination). The pure AB crystal region is highlighted in grey and its solubility in grey dash line.

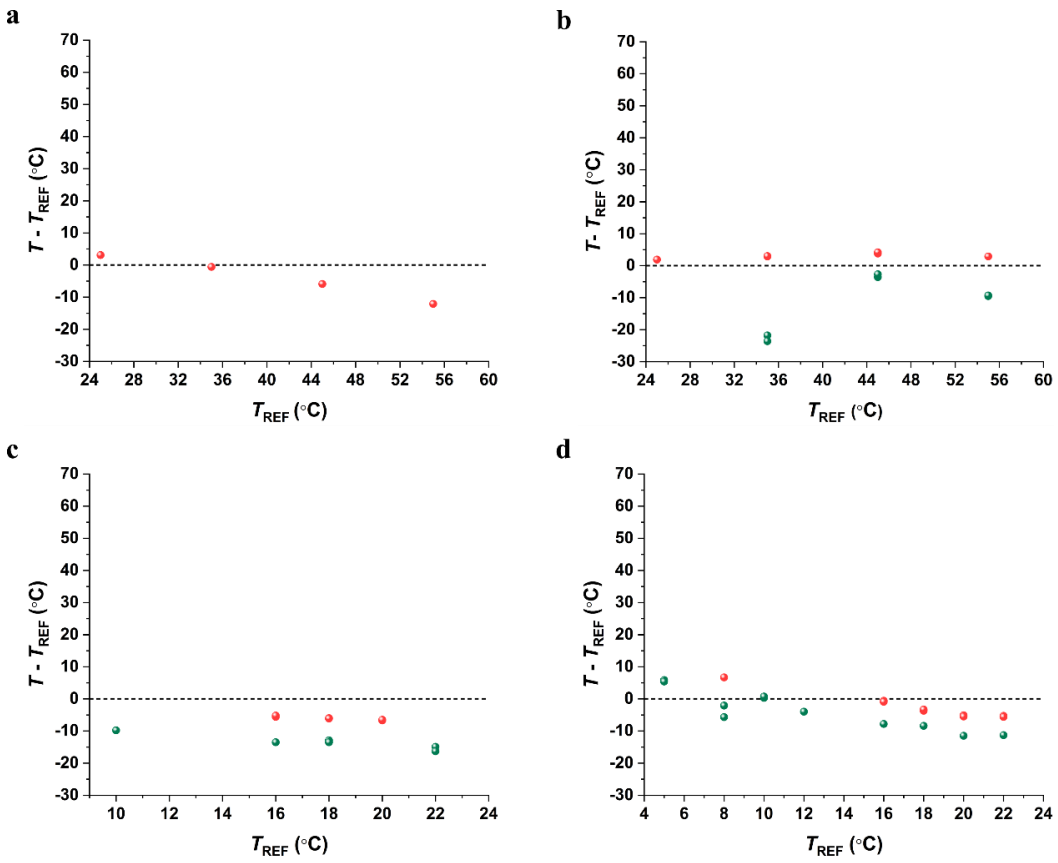

Figure 3.9 - Investigation of formation of Lev cocrystals and Eti cocrystals with different co-formers. **a** DMSA, **b** NBA**, c** MA, and **d** SA by the measurement of clear temperatures. Experimental data of Lev and coformer mixture are represented by green and experimental data of Eti and coformer mixture are represented in red.

We found that it was not possible to crystallize out any material for DHBA using either Eti or Lev despite numerous attempts including ex-situ cooling in the fridge. With co-former DMSA only the sample containing Eti crystallized out Figure 3.9a). The T-T_{REF} measurements show values close to zero indicating the absence of a cocrystal material. The Lev and Eti mixtures containing NBA (Figure 3.9b) and malonic acid (Figure 3.9c) successfully crystallized out, however, the T-T_{REF} measured was lower or did not exceed a 10°C difference to validate the formation of cocrystals.

In the case of Lev-OA and Eti-OA mixtures, the saturation temperatures diverged from the reference temperature for both mixtures (Figure 3.10a). If we assume that the individual solubility is not affected by the presence of another compound, the mixture Lev-OA and Eti-OA were not a physical mixture, but a new compound with a specific saturation temperature. The solubility of a Lev-OA compound showed saturation temperatures approx. 20 °C higher than the starting mixture. The same happened to Eti-OA compound that presented saturation temperatures approx. 45 °C higher than the starting mixture (Figure 3.10a). To verify the formation of the cocrystal we performed X-ray powder diffraction analysis and identified that 94.99 % and 85.36 % of the powder was Eti-OA cocrystals and Lev-OA cocrystals, respectively (Figure 3.10b & c). Both samples also showed the existence of oxalic acid dihydrate and oxalic acid form β in the case of Lev-OA cocrystals sample (Figure 3.10b). These impurities can be attributed to the method used for collecting and drying the sample**.** An ineffective drying method and the time expended to obtain the diffraction data could be the cause for the nucleation of both forms of oxalic acid.

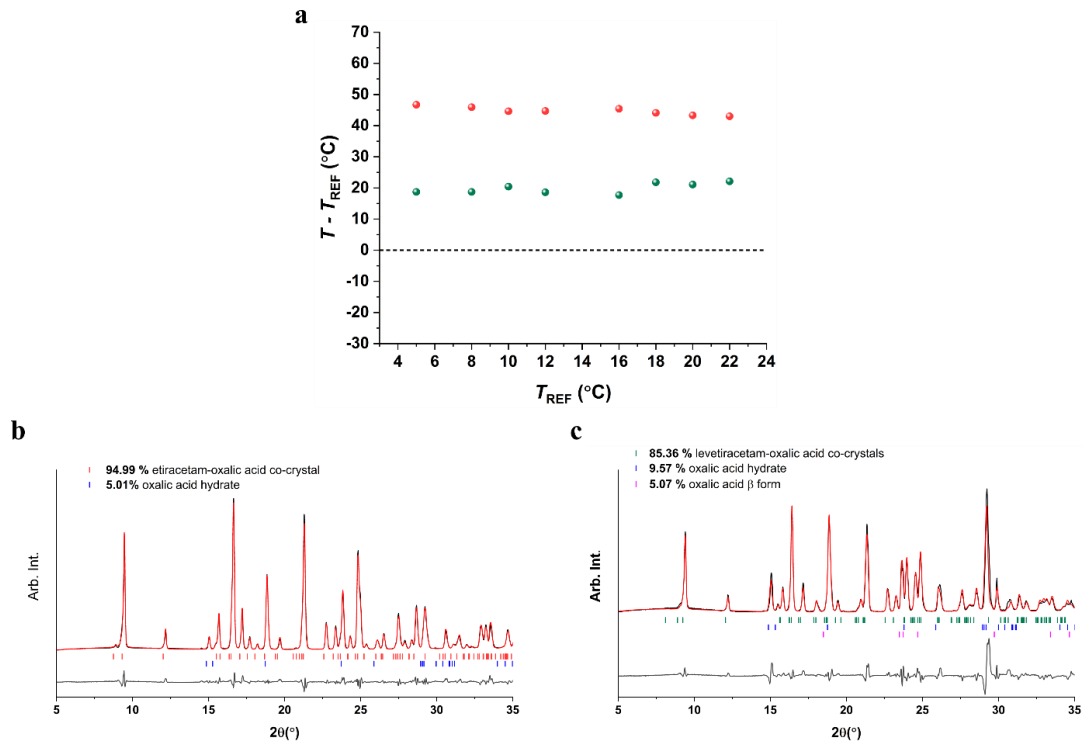

Figure 3.10 - Formation of cocrystals of Eti-oxalic acid (Eti-OA) and Lev-oxalic acid (Lev-OA). **a** measurement of the difference between the saturation temperature of the mixture and reference temperature (T-T_{REF}) i.e. the solubility temperature for Eti or Lev (T_{REF}) and OA. **b** Rietveld analysis of the Eti-OA powders from the solubility measurements showing the formation of the cocrystal and a residual oxalic dihydrate that may have formed as solvent evaporated from the crystals and **c** Rietveld analysis of the Lev-OA mixture. Again, the extra sample present is likely due to the evaporation of excess solution on drying the powders. Experimental data is represented by the black line, fitted data shown by the red line and the difference between them is shown in grey.

3.5 Eutectic compositions

A convenient approach to measure ternary phase diagrams of chiral compounds is by determining pseudo-binary phase diagrams.[19] A pseudo-binary phase diagram measures a thermodynamic quantity such as solubility or saturation temperature as a function of specific sample compositions varied along a straight line in the ternary phase diagram, Figure 3.11. By doing so, for instance the saturation temperature of samples with overall constant concentration of chiral compound but with varying

enantiomeric excess can be studied. The saturation temperature can be represented as a function of the molar fraction of the enantiomer in excess,

$$y_S = \frac{x_S}{x_S + x_R}, \qquad \textbf{Equation 3.3}$$

making sure that the total molar fraction of chiral compound (x_S + x_R) is fixed. In a ternary system this would mean that also the molar fraction of solvent remains constant during the experiment.

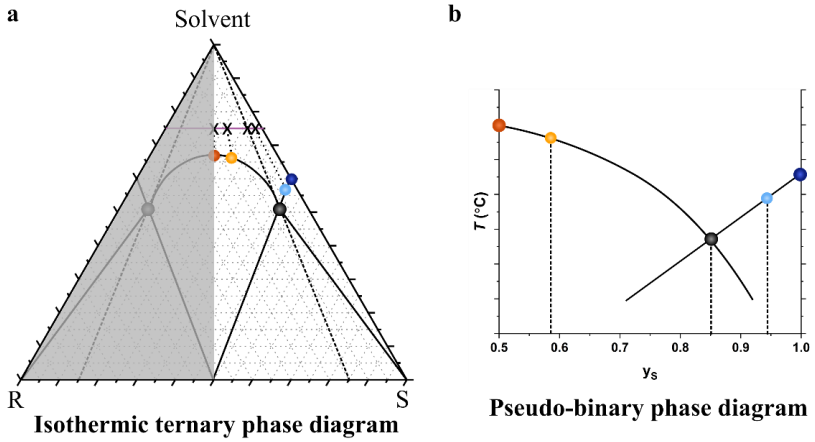

Figure 3.11 – Representation of **a** ternary phase diagram and **b** pseudo-binary phase diagram of a racemic compound in a solvent. The construction of a pseudo-binary phase diagram is obtained by varying the composition of x_S in a fixed amount of $(x_S + x_R)$ and solvent (violet straight line in the ternary phase diagram). In the ternary phase diagram several compositions are represented by ✕ to the respective solubilities (coloured circles) including the eutectic composition (black circle). The conversion of ternary phase diagram to the pseudo-phase diagram results in a representation of temperature as a function of solvent-excluded molar fraction$y_s = x_S/(x_S + x_R)$. The saturation temperatures and y_s compositions of racemic and pure enantiomer and eutectic composition are illustrated in the pseudo-binary phase diagram (orange circle, blue circle and black circle respectively).

The use of pseudo-phase diagrams allows to identify the saturation temperature and eutectic composition. Figure 3.12 represents the eutectic composition with high (right) and low values (left) in binary and respective pseudo-phase diagram. The first step in this study is to identify the eutectic composition and verify if it is possible to

alter it to lower values of eutectic composition y_S. In this way, the region of pure enantiomer crystals is wider (change from Figure 3.12a to b).

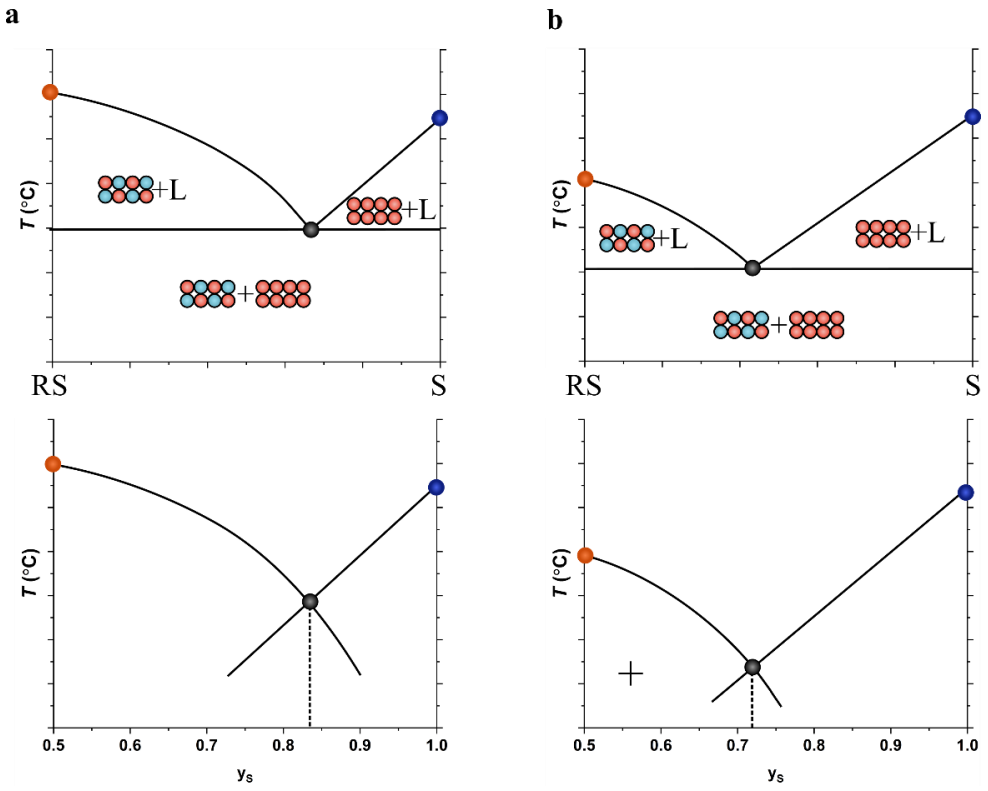

Figure 3.12 – Comparison between binary phase diagram (upper) and pseudo-phase diagram (lower) of a racemic compound with **a** low eutectic composition and **b** high eutectic composition. The racemic crystals are illustrated by a set of blue and red circles and pure enantiomer by red circle. The letter L represents the melt phase (this is not observed in the pseudo-phase diagram as we are in solution). The melting temperature and solubilities of racemic compound and pure enantiomers are shown in orange and blue circles. The eutectic composition is highlight by the dash line in black.

We determined the pseudo-binary phase diagram at $(x_S + x_R)$= 0.061 mmol·mmol^{-1} while varying the solvent excluded S-enantiomer fraction y_S shown Figure 3.13a. The pseudo-binary phase diagram clearly presents a shape for a chiral compound that behaves as a racemic compound system.[19] The theoretical solubility lines can be estimated by applying the same principle in Equation 3.2. (van't Hoff fitting), using A = -ΔH /R. The A values determined for pure Lev and Eti were applied

to define left and right branch, respectively. The experimental eutectic composition was found close to the theoretical value, y_{eu}^{ex} = 0.86 and y_{eu}^{th} = 0.87, with respective saturated temperature of T_{eu}^{ex} = 42.0 °C and T_{eu}^{th} = 44.0 °C, as a shown in Figure 3.13a. The experimental data show a deviation with respect to the theoretical solubility lines induce by the influence of the counter enantiomer in the solubility of Eti and Lev; the model assumes ideality of the solution where one component does not affect the solubility of the other.

The eutectic composition of the Lev and Eti mixture will be compared with the eutectic composition of the Lev and Eti and coformer mixture to identify the changes in the eutectic composition due to cocrystallisation. The eutectic composition obtained in this procedure should be lower than 0.87 to enhance the condition of pure enantiomer crystallisation.

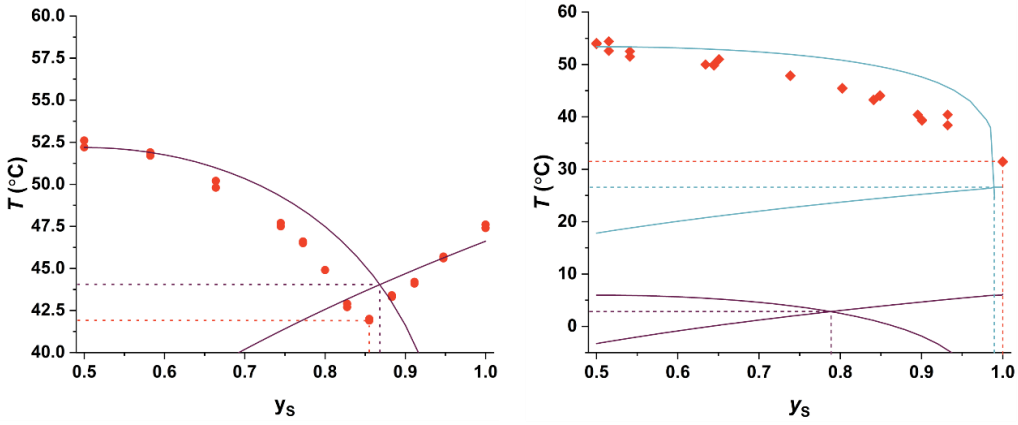

Figure 3.13– Pseudo-binary phase diagram of Eti and Lev in acetonitrile without (left) and with (right) the co-former oxalic acid shown as the measured saturation temperature T against the S-enantiomer fraction $y_S = x_S/(x_S + x_R)$. Left: $(x_S + x_R) = 0.061$. Right: (x_S+x_R) = 0.00486 mmol·mmol^{-1}, oxalic acid concentration x_{OA}=0.067 mmol·mmol^{-1}. The blue lines are the estimated pseudo-binary phase diagram using the cocrystal solubilities. The violet lines in both graphs are the estimated pseudo-binary phase diagram using the pure components solubilities in absence of coformer.

The determination of pseudo-binary phase diagram of the chiral system in the previous section was the first step to characterize the chiral system and to understand how the shift of the eutectic composition could improve the conditions for chiral resolution. We applied cocrystallisation method by adding an achiral compound, oxalic acid (OA) to the chiral system. The formation of racemic cocrystal and enantiomer cocrystal may change the stability of the chiral compounds and eutectic composition of the system. The addition of a new component into the system changes the system from three components to four. The representation of this system can be schematically visualized in a quaternary phase diagram at pressure and temperature constants, Figure 3.14. To ensure that we are still dealing with a pseudo-binary phase diagram despite the increase in number of components, the composition of the mixture $(x_S + x_R)$, the amount of solvent and the amount of co-former are fixed.

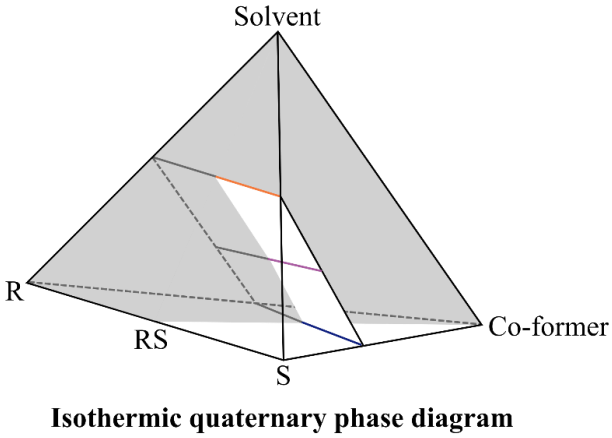

Figure 3.14 – Representation of a quaternary phase diagram of chiral system and co-former in a solvent. If the amount of solvent (orange line) and co-former (blue line) are fixed, it is possible to determine the saturation temperature of composition mixtures between pure racemic and pure S-enantiomer (violet line) which could be represented in a form of pseudo-phase diagram.

A pseudo-binary phase diagram with a fixed composition of solvent (0.927 mmol·mmol^{-1}), x_S+x_R (0.00486 mmol·mmol^{-1}) and co-former (0.067 mmol·mmol^{-1})

was measured as well (Figure 3.13b). As expected by the saturation temperature determined above, the saturation temperature for both cocrystals is higher than the single compounds at the same condition. This can be seen by the comparison of the measured points with the pseudo-binary phase diagram in violet. The variation of saturation temperature between Eti and Eti-oxalic acid is approximately 45 °C and between Lev and Lev-oxalic acid it is 25 °C. The formation of cocrystals increases the difference between the pure enantiomer compound and the racemic compound, reflecting into a substantial increase of eutectic composition to around y_S = 0.99. The racemic cocrystal is predominant in all the phase diagram.

3.6 Discussion

In this work, we started by determining the solubility of Eti and Lev in acetonitrile, acetone and ethlyacetate. The experimental data collected in acetonitrile presented a good theoretical fit using the van't Hoff equation. The solubility of Eti and Lev in acetonitrile is similar at low temperature (10-25°C), however, at increased temperatures the relative solubility for Lev progressively increased, resulting in a 1.5 times higher solubility at 60 °C. This indicates that the relative stability of the racemic compound Eti compared to the enantiopure compound Lev decreases with increasing temperature. Still, the racemic compound remains more stable than the conglomerate system in racemic suspensions up to the melting temperature.

We explored the ternary phase diagram of racemic Eti in acetonitrile at constant pressure and amount of solvent, determining saturation temperatures of specific compositions. In this way, we can represent the ternary phase diagram as a pseudo-binary phase diagram. For an overall mole fraction $(x_S + x_R)$= 0.061 the eutectic

composition and eutectic composition temperature were y_s = 0.86 and T= 42.0 °C. As at the same overall mole fraction the saturation temperature of Eti and Lev were 52.5 and 47.5°C, respectively, Figure 3.13a, the eutectic composition is closer to the pure composition of Lev (S-enantiomer). This means that the compositional region in the ternary phase diagram for crystallisation of enantiopure Lev is smaller than the crystallisation region for racemic compound. To perform a chiral resolution of Eti by crystallisation at these conditions (solvent, Eti and Lev composition and pressure), the solution requires to be enriched to values higher than y_s = 0.86 by another separation technology.

We applied solution cocrystallisation as a method to manipulate the position of the eutectic point by cocrystallizing Eti and Lev with co-formers. The solubility order at 45°C were found from less soluble Eti < NBA < SA < DMSA < DHBA < Lev < MA < OA, Figure 3.7. The relative solubility between the Eti /Lev and the co-former strongly influences the appearance of the cocrystal phase diagram and therefore this has to be accounted for in the cocrystal screening stage.[29] In this way, we found that cocrystals form for both Eti and Lev with OA. The cocrystallisation of Lev and Eti with OA was confirmed by XRPD and the pseudo-phase diagram of this system showed much higher saturation temperature than the initial chiral pseudo-phase diagram. This indicates that the cocrystal of both Lev and Eti are much more stable than their single component counterparts.

However, we were not able to find indications of cocrystal formation of Eti and Lev with the other selected coformers. This could be related to a asymmetry phase diagram of the cocrystal. To validate this assumption more demanding methodology can be used as high-performance liquid chromatography to analyse the composition of

liquid phase remaining after crystallisation followed by the determination of crystal form though XRPD.

The goal of this study was to validate the use of cocrystallisation to move the eutectic point. Although that was achieved, as can be seen in Figure 3.13b, the shift towards more extreme values of eutectic composition y_s does not improve the potential for chiral resolution.

3.7 Conclusion

We showed that cocrystallisation of a chiral compound with an achiral coformer can change the eutectic composition of a chiral system. However, the choice of oxalic acid as co-former for Etiracetam changed drastically the eutectic composition towards $y_S = 1$, because the increase in stability of the racemic cocrystal compound compared to the racemic compound Etiracetam outweighs the increase in stability of the enantiopure cocrystal compound compared to the enantiopure compound Levetiracetam. To increase the ease of resolution a lower eutectic composition value would usually be preferred. In that case, the increase in stability for the enantiopure cocrystal needs to substantially outweight that of the racemic cocrystal.

3.8 Acknowledgements

This work was supported by a STSM Grant from COST Action CM1402 Crystallize. This grant gave me the opportunity to start this study in the Institute of Condensed Matter and Nanosciences at the *Université Catholique de Louvain* and to present this work at CM1402 Crystallize Conference in Czech Republic. I would like

to thank Professor Tom Leyssens for the supervision during the period of the execution of work at the *Université Catholique de Louvain.*

I also would like to thank EPSRC and the Doctoral Training Centre in Continuous Manufacturing and Crystallisation (Grant Ref: EP/K503289/1) and the Centre for Innovative Manufacturing in Continuous Manufacturing and Crystallisation (Grant Ref: EP/I033459/1) for funding this work.

I like to acknowledge that this work was carried out in the CMAC National Facility supported by UKRPIF (UK Research Partnership Fund) award from the Higher Education Funding Council for England (HEFCE) (Grant Ref: HH13054).

3.9 References

(1) Murakami, H. From Racemates to Single Enantiomers – Chiral Synthetic Drugs over the Last 20 Years. In *Topics in Current Chemistry*; 2006; Vol. 269, pp 273–299. https://doi.org/10.1007/128_2006_072.

(2) Gal, J. When Did Louis Pasteur Present His Memoir on the Discovery of Molecular Chirality to the Académie Des Sciences ? Analysis of a Discrepancy. *Chirality* **2008**, *20* (10), 1072–1084. https://doi.org/10.1002/chir.20532.

(3) Pasteur, L. C. R. No Title. *Hebd. Séanc. Acad. Sci Paris* **1848**, *26*, 535.

(4) Jacques, J.; Wilen, S. H.; Collet, A. *Enantiomers, Racemates, and Resolutions*; Wiley: New York, 1981.

(5) Boldyreva, E. V. CHAPTER 2: High Pressure Crystallography: Elucidating the Role of Intermolecular Interactions in Crystals of Organic and Coordination Compounds. In *Monographs in Supramolecular Chemistry*; 2019; Vol. 2019-Janua, pp 32–97. https://doi.org/10.1039/9781788013086-00032.

(6) Islam, M. R.; Mahdi, J. G.; Bowen, I. D. Pharmacological Importance of Stereochemical Resolution of Enantiomeric Drugs. *Drug Saf.* **1997**, *17* (3), 149–165. https://doi.org/10.2165/00002018-199717030-00002.

(7) Nguyen, L. A.; He, H.; Pham-Huy, C. Chiral Drugs: An Overview. *Int. J. Biomed. Sci.* **2006**, *2* (2), 85–100.

(8) Calcaterra, A.; D'Acquarica, I. The Market of Chiral Drugs: Chiral Switches versus de Novo Enantiomerically Pure Compounds. *Journal of Pharmaceutical and Biomedical Analysis*. Elsevier B.V. January 5, 2018, pp 323–340. https://doi.org/10.1016/j.jpba.2017.07.008.

(9) Lorenz, H.; Seidel-Morgenstern, A. Processes To Separate Enantiomers. *Angew. Chemie Int. Ed.* **2014**, *53* (5), 1218–1250. https://doi.org/10.1002/anie.201302823.

(10) Lorenz, H.; Seidel-Morgenstern, A. Separation Processes to Provide Pure Enantiomers and Plant Ingredients. *Annu. Rev. Chem. Biomol. Eng.* **2020**, *11*, 469–502. https://doi.org/10.1146/annurev-chembioeng-100419-103732.

(11) Lorenz, H.; Perlberg, A.; Sapoundjiev, D.; Elsner, M. P.; Seidel-Morgenstern, A. Crystallization of Enantiomers. *Chem. Eng. Process. Process Intensif.* **2006**, *45* (10), 863–873. https://doi.org/10.1016/j.cep.2005.11.013.

(12) Coquerel, G. Crystallization of Molecular Systems from Solution: Phase Diagrams, Supersaturation and Other Basic Concepts. *Chem. Soc. Rev.* **2014**, *43* (7), 2286–2300. https://doi.org/10.1039/C3CS60359H.

(13) Lorenz, H. Solubility and Solution Equilibria in Crystallization. In *Crystallization: Basic Concepts and Industrial Applications*; Wiley-VCH Verlag GmbH & Co. KGaA: Weinheim, Germany, 2013; pp 35–74.

https://doi.org/10.1002/9783527650323.ch3.

(14) Secor, R. M. Resolution of Optical Isomers by Crystallization Procedures. *Chem. Rev.* **1963**, *63* (3), 297–309. https://doi.org/10.1021/cr60223a006.

(15) Coquerel, G. Preferential Crystallization. *Topics in Current Chemistry*. August 30, 2006, pp 1–51. https://doi.org/10.1007/128_2006_077.

(16) Lorenz, H.; Polenske, D.; Seidel-Morgenstern, A. Application of Preferential Crystallization to Resolve Racemic Compounds in a Hybrid Process. *Chirality* **2006**, *18* (10), 828–840. https://doi.org/10.1002/chir.20327.

(17) Levilain, G.; Coquerel, G. Pitfalls and Rewards of Preferential Crystallization. *CrystEngComm* **2010**, *12* (7), 1983–1992. https://doi.org/10.1039/c001895c.

(18) Viedma, C. Chiral Symmetry Breaking during Crystallization: Complete Chiral Purity Induced by Nonlinear Autocatalysis and Recycling. *Phys. Rev. Lett.* **2005**, *94* (6), 065504. https://doi.org/10.1103/PhysRevLett.94.065504.

(19) Srisanga, S.; ter Horst, J. H. Racemic Compound, Conglomerate, or Solid Solution: Phase Diagram Screening of Chiral Compounds. *Cryst. Growth Des.* **2010**, *10* (4), 1808–1812. https://doi.org/10.1021/cg901483v.

(20) Leyssens, T.; Horst, J. ter. Solution Co-Crystallisation and Its Applications. In *Multi-Component Crystals: Synthesis, Concepts, Function*; Tiekink, E., Ed.; De Gruyter, 2017.

(21) Li, W.; de Groen, M.; Kramer, H. J. M.; de Gelder, R.; Tinnemans, P.; Meekes, H.; ter Horst, J. H. Screening Approach for Identifying Cocrystal Types and Resolution Opportunities in Complex Chiral Multicomponent Systems. *Cryst. Growth Des.* **2021**, *21* (1), 112–124. https://doi.org/10.1021/acs.cgd.0c00890.

(22) Li, Weiwei; de Groen, Mariette; Kramer, Herman J.M.; Gelder, René de;

Tinnemans, P.; Meekes, Hugo;H. ter, J. Novel Crystallization Techniques for Separation in Multi-Component Systems, Delft University of Technology, 2018. https://doi.org/https://doi.org/10.4233/uuid:436c4e79-7b47-40b7-ade0-fc24b8a5e5c2.

(23) Horst, J. H. T.; Deij, M. A.; Cains, P. W. Discovering New Co-Crystals. *Cryst. Growth Des.* **2009**, *9* (3), 1531–1537. https://doi.org/10.1021/cg801200h.

(24) Reus, M. A.; van der Heijden, A. E. D. M.; ter Horst, J. H. Solubility Determination from Clear Points upon Solvent Addition. *Org. Process Res. Dev.* **2015**, *19* (8), 1004–1011. https://doi.org/10.1021/acs.oprd.5b00156.

(25) Coelho, A. A. TOPAS and TOPAS-Academic : An Optimization Program Integrating Computer Algebra and Crystallographic Objects Written in C++. *J. Appl. Crystallogr.* **2018**, *51* (1), 210–218. https://doi.org/10.1107/S1600576718000183.

(26) George, F.; Tumanov, N.; Norberg, B.; Robeyns, K.; Filinchuk, Y.; Wouters, J.; Leyssens, T. Does Chirality Influence the Tendency toward Cocrystal Formation? *Cryst. Growth Des.* **2014**, *14* (6), 2880–2892. https://doi.org/10.1021/cg500181t.

(27) Chiarella, R. A.; Davey, R. J.; Peterson, M. L. Making Co-Crystals - The Utility of Ternary Phase Diagrams. *Cryst. Growth Des.* **2007**, *7* (7), 1223–1226. https://doi.org/10.1021/cg070218y.

(28) Nehm, S. J.; Rodríguez-Spong, B.; Rodríguez-Hornedo, N. Phase Solubility Diagrams of Cocrystals Are Explained by Solubility Product and Solution Complexation. *Cryst. Growth Des.* **2006**, *6* (2), 592–600. https://doi.org/10.1021/cg0503346.

(29) Springuel, G.; Collard, L.; Leyssens, T. Ternary and Quaternary Phase Diagrams: Key Tools for Chiral Resolution through Solution Cocrystallization. *CrystEngComm* **2013**, *15* (39), 7951. https://doi.org/10.1039/c3ce41141a.

Chapter 4

The Effect of Chirality on the Compression of 2-(2-Oxo-1-pyrrolidinyl) butyramide

This chapter has been published in *Crystal Growth & Design*
Authors: Suse S. Bebiano, Joop H. ter Horst, and Iain D.H. Oswald

4.1 Abstract

Understanding polymorphism in chiral systems for drug manufacturing is essential to avoid undesired therapeutic effects. Generally, polymorphism is studied through changes in temperature and solution concentration. A less common approach is the application of pressure. The goal of this work is to investigate the effect of pressure on levetiracetam (pure enantiomer) and etiracetam (racemic compound). An anisotropic compression of levetiracetam and etiracetam is observed to 5.26 and 6.29 GPa, respectively. The most compressible direction for both was identified perpendicular to the layers of the structure. Raman spectroscopy and the analysis of intermolecular interactions suggests subtle phase transitions in levetiracetam (~2 GPa) and etiracetam (~1.5 GPa). The stability of etiracetam increases with respect to levetiracetam on compression hence chiral resolution of this system is unfavorable using pressure. This work contributes to the ongoing efforts in understanding the stability of chiral systems.

4.2 Introduction

Polymorphism is the ability of a chemical compound to exist in more than one crystalline form.[1] This phenomenon plays an important role in the development of new drugs due to a possible modification of physicochemical properties in active pharmaceutical ingredients (APIs), e.g. solubility, processing behavior and bioavailability.[2,3] The discovery of a new polymorphic form in the screening process could bring the opportunity to design a different drug manufacturing process and also to generate intellectual property.[3] However, the appearance of a new polymorphic form during the manufacturing process is undesirable, due to a possible unwanted effects, such as processing behavior, shelf life and harmful interaction with the biological target.[3]

Polymorphism can also be found in chiral compounds, which are more than 50 % of API currently in the market.[4] Chirality is identified when a chemical compound exhibits two non-superimposable mirror-image conformers (enantiomers). The physicochemical properties of the two enantiomers are identical, however, their optical activity is opposite and their spatial arrangement which can lead to different physiological responses. Typically, these two enantiomers can be found as single crystalline entities or together in a 50/50 equimolar mixture, forming a physical mixture (racemic mixture) or a crystalline compound (racemic compound).[5] In Nature, only the single enantiomer forms are observed, for example, natural amino acids and natural sugars. Contrarily, racemic compounds are the main product of synthesis and extra separation techniques are necessary to obtain the pure enantiomer.6 When a new chiral compound is developed as an API, a enantiopure crystal form is selected preferentially rather than racemic compounds. This is due to the different biologic

activity of enantiomers which can be undesirable hence the separation of enantiomers is essential.[4,7,8]

Crystallisation can be a highly selective separation technique, even for compounds as similar as enantiomers. Usually, crystallisation is initiated by varying parameters such as solvent, temperature and humidity; the thermodynamic parameter pressure is rarely explored. To the best of our knowledge, combined studies of pure and racemic compounds at high pressure have only been reported for amino acids[9–13] and, more recently, the enantiomers of mandelic acid[14–16] and 1,1'-binaphthyl[17] were explored to design pressure-temperature spontaneous resolution. The resolution of mandelic acid has been challenged using single X-ray diffraction attributing the structural transformation at 0.65 GPa to a phase transition from form I to form II of DL-mandelic acid.[15,16]

In this work, we explore the structural features of the RS- and S-forms of 2-(2-Oxo-1-pyrrolidinyl) butyramide. Our inspiration to investigate this system was the extensive polymorphic behavior of piracetam (2-oxo-pyrrolidineacetamide) (an analogous compound without the ethyl group).[18,19] It possesses three polymorphic forms at atmospheric pressure and two high-pressure forms as well as two hydrates.[20–25] 2-(2-Oxo-1-pyrrolidinyl) butyramide crystallizes in two racemic polymorphs at atmospheric pressure (etiracetam, Eti).[26] Form I (monoclinic, P21/c) is stable below 303.5 K and form II (monoclinic, P21/c) is formed via a suspension of form I in methanol above 313 K. In contrast, despite several crystallisation attempts only one crystalline structure was reported for the enantiopure S-form, levetiracetam (Lev).[27,28] Given the extensive crystallisation behavior of piracetam, it is possible that Lev and Eti show equally a rich diagram at high pressure.

The aim of this study is to investigate how the chirality of the material influences the compression of these systems and to identify whether pressure can be used as a tool for the enantiomeric separation. First, we explored the structures at ambient pressure using Raman spectroscopy to identify pressure points at which potential phase transitions might occur. Then, we have followed these studies with X-ray diffraction measurements to gain insight into the changes to the molecular and crystal structure as a function of pressure. Crystal energy calculations using CrystalExplorer have been used to provide intermolecular interaction energies and relate these to the phase transitions that occur in both crystal forms

4.3 Experimental procedure

4.3.1 Materials

Lev and Eti were purchased from Xiamen Top Health Biochem Tech. Co., Ltd. Both samples were recrystallized by cooling crystallisation in ethyl acetate solvent (Sigma-Aldrich) followed by fast solvent evaporation where a drop of saturated solution was placed on a microscopic slide).

4.3.2 Diamond anvil cell (DAC) preparation

A Merrill–Bassett diamond anvil cell (DAC) equipped with 600 μm culet was used to generate pressure.[29] A tungsten foil (200 μm) was indented to a thickness of 100 μm and a 250 μm hole was drilled in the center of indented gasket using an Almax Easylab Microdriller. Four samples were loaded individually into the DAC: i) powder of Lev; ii) single crystal of Lev; iii) powder of Eti form I and; iv) single crystal of Eti.

In each cell, a ruby was loaded into the cell for pressure measurement by ruby-fluorescence method.[30] In all experiments, petroleum ether 35/60 (Alfa Aesar) was used as the pressure-transmitting medium. In the case of Lev, three samples were loaded with single crystals to verify the compression of the structure using unit cell information. In Figure 4.20, the data point for these crystals are highlighted in different shades of the same color.

4.3.3 Raman spectroscopy

Raman spectra of Lev and Eti samples loaded into the DAC were collected using Horiba Jobin Yvon, XploRA micro Raman system using a 532 nm laser line with a 1200 lines/mm grating and CCD detector. An Olympus Microscope coupled with a LWD 50 × objective lens was used for visualization of the sample. The spectra were collected and analyzed using the LabSpec 6 program in the region between 50 and 3500 cm^{-1}. Data collection times and parameters were varied to maximize the signal-to-noise ratio for each pressure.

4.3.4 Single crystal X-ray diffraction

Single crystal X-ray diffraction data were collected by Bruker Kappa Apex II Duo diffractometer using Mo Kα radiation (λ = 0.71073 Å) at 300 K. Diffraction data were acquired using the strategy developed by Dawson *et al.,* adding the movement of kappa angle of -90 or 90°.[31] In APEX 3[32], the datasets were integrated using SAINT[33] with dynamic masks procedure implemented in the program. Absorption correction was carried out using the SHADE.[34] The crystal structures were refined in Olex2[35] using SHELXL.[36] The atomic coordinates were taken from the Cambridge Structural

Database (CSD)[37,38] and used as the starting model for the refinement of Lev (CSD recode OMIVUB[27]) and Eti form I (CSD refcode OFIQUR[26]). All non-hydrogen atoms were refined anisotropically with the use of the RIGU restraint.[39] The hydrogen atoms were placed on the carbon atoms except those involved in hydrogen bonding, e.g. NH_2, which were found from the difference map and allowed to optimize before riding model used as per the procedures in OLEX2. Eti single crystal data set was collected at 0, 0.60, 0.80, 1.02, 1.24, 1.40, 1.90, 2.51, 2.98, 3.51, 3.95, 4.84, 5.51 and 6.29 GPa and LEV single crystals were collected at pressures 0, 0.73, 1.29, 2,00, 2.71, 3.1, 3.67, 4.19, 4.61 GPa. These data have been deposited in CSD with the numbers 2011949-66, 2011968-2011970. To probe the potential phase transition two further LEV crystals were collected at the 1.20, 2.12, 2.68, 3.59, 3.81 and 4.83 GPa for unit cell information only. The crystallographic information can be found in the supplementary information (Table S1 and S2).

4.3.5 Structure analysis

The analysis of molecular and crystal structure was performed using the Mercury 4.1.3 software[38] from Cambridge Crystallographic Data Centre (CCDC). The software CrystalExplorer[40] was used to understand the intermolecular interactions. The calculation of energy was performed between a central molecule and a cluster of molecules in a radius of 3.80 Å using B3LYP/6-31G(d,p) method. The EoSFit7-GUI[41] software was applied to obtain the equation of state (EoS) parameters from diffraction data collected as a function of varying pressure. The calculation of the strain tensor and compressibility indicatrix was performed using PASCal[42] and visualized in VESTA 3.4.6.[43]

4.4 Results & Discussion

4.4.1 Structural analysis of Levetiracetam and Etiracetam

In this study, we have investigated the structural changes that occur in 2-(2-oxopyrrolidin-1-yl) butyramide as a function of pressure. It can crystallize in a chirally pure (Lev) or as a racemic crystal (Eti). Lev is the S-enantiomer and there is only one crystalline form known. Eti crystallizes in two polymorphic forms but in this study, we have only characterized form I as this is the most stable form at room temperature. The molecular structure has a chiral carbon that is linked to an ethyl group, an amide group (CNH2), as well as to an oxopyrrolidine ring (O(py)) that adopts a half-chair conformation (Figure 4.1). The molecular conformation of each of the forms is altered due to the crystal packing but the greatest difference observed is the torsional angle between the amide group and the oxopyrrolidine group (20°; Table 4.1). Torsion angles are relatively soft parameters hence there is the potential that these will show a large change on compression. Two metrics by which we can measure these changes as a function of pressure are the globularity and asphericity. These metrics are derived from Hirshfeld surfaces[44,45] where the crystalline electron distribution is divided into molecular fragments thus the surface is generated using both intermolecular and intramolecular interaction. Asphericity is a measure of molecular anisotropy and globularity is the difference between Hirshfeld surface area and the sphere area with the same volume. At ambient pressure, despite the different conformation, 2-(2-oxopyrrolidin-1-yl) butyramide in Lev and Eti has similar values for this parameters (asphericity 0.033 cf. 0.032; globularity 0.831 cf. 0.839).

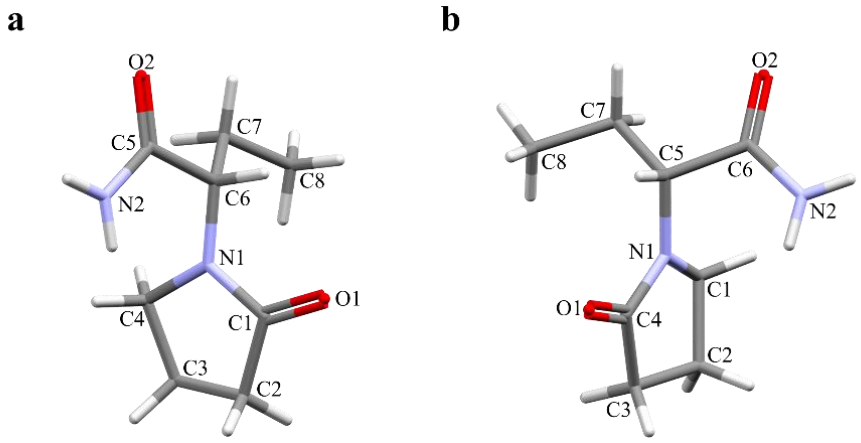

Figure 4.15. - The molecular structure and numbering scheme for **a** S-enantiomer (Lev) (chiral carbon C6) and **b** R-enantiomer present in racemic compound (Eti) (chiral carbon C5) taken from reference structures deposited in the CSD (OMIVUB[27] and OFIQUR[26]). It is not ideal that the numbering schemes are different in both compounds, however to be consistent with the reference we are following the above numbering schemes

Table 4.1. - Torsional angles taken from reference structures deposited in the CSD (OMIVUB[27] and OFIQUR[26]). The information for the R-enantiomer is taken from the molecule in the racemic crystal hence all values would be inverted for the S-enantiomer.

S-enantiomer torsion angles in Lev (°)		R-enantiomer torsional angle in Eti (°)	
C3-C4-N1-C6	163.9(4)	C2-C1-N1-C5	170.55(8)
O1-C1-N1-C6	6.0(6)	O1-C4-N1-C5	-4.9(1)
N1-C6-C5-O2	-166.9(3)	N1-C5-C6-O2	146.74(9)
N1-C6-C7-C8	-54.5(5)	N1-C5-C7-C8	58.2(1)
C5-C6-C7-C8	176.4(4)	C6-C5-C7-C8	-176.07(9)

Lev crystallizes in the monoclinic space group $P2_1$ with a single molecule of Lev in the asymmetric unit. At 293(2) K (CSD refcode: OMIVUB), the unit cell parameters are a = 6.272(5) Å, b = 7.993(5) Å, c = 9.199(7) Å, β = 108.645(9)° and V = 436.962 Å^3 which gives a molecular volume of 218.5 Å^3.[27] In contrast, the crystal structure of Eti form I crystallizes in the centrosymmetric monoclinic space group

$P2_1/c$ with unit cell parameters: a = 9.593(2) Å, b = 7.8325(3) Å, c = 11.9547(4) Å, β = 103.830(3)° and V = 872.22 (5) Å^3 at 293 K (CSD refcode: OFIQUR).[26] The molecular volume for Eti is 218.1 Å^3 hence there is no difference in molecular volumes between the chiral and racemic crystal.

The structure of Lev is organized through hydrogen bonds between the amide groups and the oxopyrrolidine group (N···O(py)' 3.038(5) Å, NH···O(py)' 156°) forming infinite chains through a 2_1-screw axis along the *b*-direction (dark blue hydrogen bond in Figure 4.16a).[27] The interaction between adjacent molecules in this chain is the strongest in the crystal (total -48.0 kJ·mol^{-1}; CrystalExplorer[40]). Following the same translation symmetry (light blue hydrogen bond in Figure 4.16a), a second chain is established through the amide groups (N···O(CNH_2)' 2.995(5) Å, NH···O(CNH_2)' 168°) where the energy of the interaction is also very strong (total -37.8 kJ·mol^{-1}). The combination of these two interactions form rings of four molecules described by a $R_4^4(20)$ graph set (blue area in Figure 4.16a). This motif is propagated along the *b*-direction by 2_1-screw axis.

The molecular packing of Eti is constructed through a hydrogen bond between amide groups (NH···O(CNH_2)' 3.031(9) Å, NH···O(CNH_2)' 159(3)°) building enantiopure chains that lie parallel to the (1 0 -1) plane (dark blue - Figure 4.16c).[26] It is interesting to observe that, despite Eti being racemic, each enantiomer forms a hydrogen bond chain with itself rather than the other enantiomer. This hydrogen bond chain in Eti, constructed by the dark blue hydrogen bonds in Figure 4.16c, is comparable in geometry and hydrogen bond interaction energy (-32.7 kJ·mol^{-1} *cf.* -37.8 kJ·mol^{-1}) to the hydrogen bond chain in Lev, constructed by the light blue hydrogen bonds in Figure 4.16a. The difference in the structures lies in the relationship

between the two chains and hydrogen bonds between them. The chains in Eti are linked through the inversion center to form centrosymmetric dimers connected through a hydrogen bond between the secondary amide hydrogen and the oxopyrrolidine group (NH···O(py) 3.056(4) Å), NH···O(py)' 166(1)°). Due to the dimer arrangement of counter enantiomer molecules consisting of two strong hydrogen bonds the intermolecular interaction energy is -84.3 $kJ \cdot mol^{-1}$.

Both Lev and Eti form layered structures Figure 4.16b & d) where strongly hydrogen-bonded layers are stacked through weaker van der Waals interactions. This type of structural feature is an important feature as previous high-pressure studies have shown that compression is generally observed in the direction perpendicular to the layers due to the lack of strong interactions.[46,47] In Lev, the three-dimensional crystal structure is built through translation of the hydrogen-bonded layer along the *a*-direction. The layers have saw-tooth profile when viewed along the *b*-direction and interact through weaker van der Waals interactions (-11.6 to -17.1 $kJ \cdot mol^{-1}$) where the energy is largely made of dispersion component (Figure 4.16b). In Eti, the layer is not planar but shows a stepped motif where the dimer interaction links the hydrogen-bonded chains together into the layer parallel to the (1 0 -1) plane (Figure 4.16d). Again, there are only van der Waals interactions between the layers but these interactions have a larger range of energies (-1.2 to -31.6 $kJ \cdot mol^{-1}$).

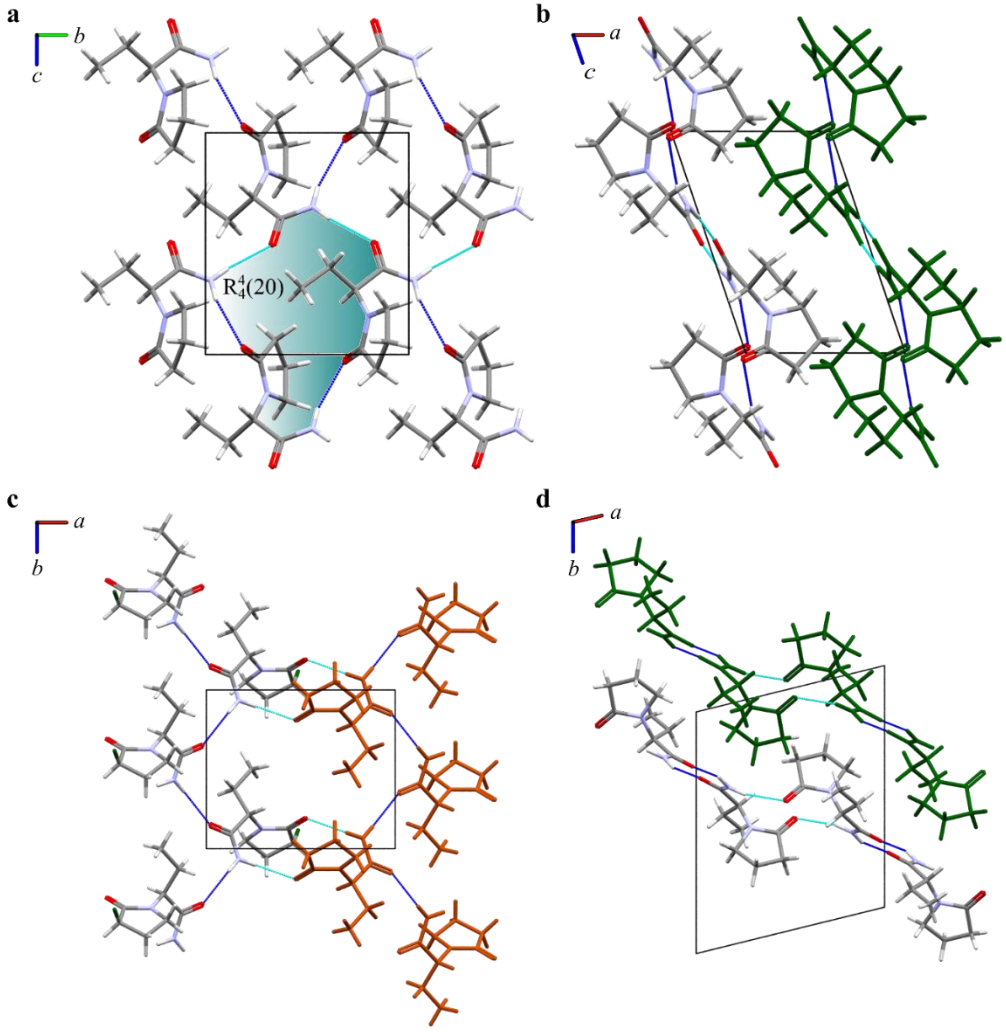

Figure 4.16 - Crystal structure of Lev and Eti. **a** the crystalline structure of Lev is formed through two infinite chains, NH···O(py) (in dark blue) and NH···O(CNH_2) (in light blue) following the *b*-direction; **b** the structure of Lev is packed through van der Waals interactions along *a*-axis (view of two layer – in element color and green color layer), **c** In Eti infinite enantiopure chains (S-enantiomer (in element color) and R-enantiomer (in orange)) formed through NH···O(CNH_2) hydrogen bonds (in dark blue); the chains are linked by NH···O(py) hydrogen bond (in light blue) creating a centrosymmetric dimer; **d** In Eti chains are parallel to the (1 0 -1) plane and are linked by an inversion center. The stepped layers are depicted in green.

4.4.2 Raman spectroscopy study of Levetiracetam and Etiracetam

Raman spectroscopy is a quick method to survey structural changes with respect to pressure. Whilst it shows intramolecular vibrations it can also provide information about the changes in structure through phonon regions of the spectrum. The Raman spectrum of commercial Lev and Eti as well as the band assignments for Lev are shown in Figure 4.17. The band assignments for Lev were applied following the literature values from the work of T. Ramya *et al.*[48]; we have not found any assignments for Eti but it can be assumed the assignments for the molecular vibrations will be similar. The frequencies for the bending of OCN (349 cm^{-1}), the combination of torsional $OCNC_{tors}$ and bending of CCN (707 cm^{-1}) and the stretching of N-H (3200 - 3367 cm^{-1}) are important, since, those reflect the molecular conformation induced by intramolecular and intermolecular interaction. These bands have the potential to allow us to understand the change during the compression process.

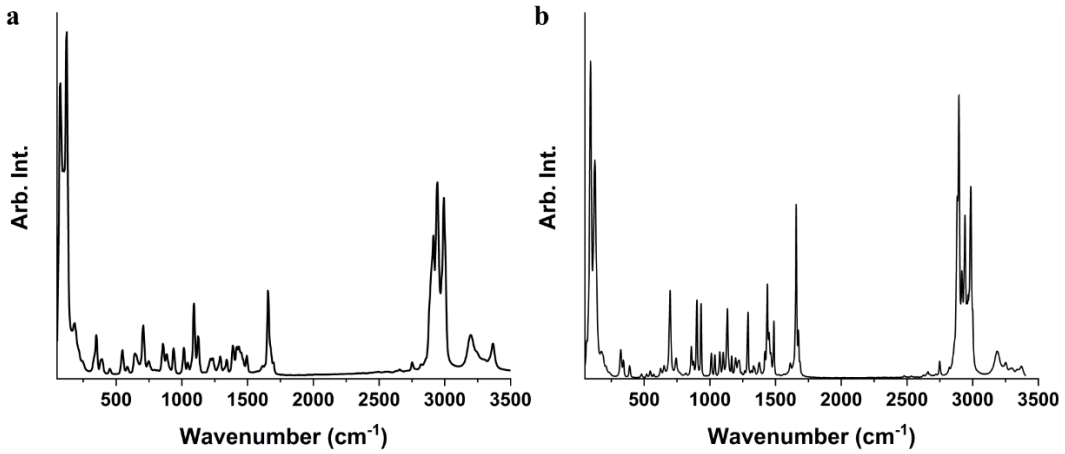

Figure 4.17. - Raman spectrum of commercial **a** Lev and **b** Eti at atmospheric pressure.

For our pressure studies we used two different sample types to understand how the crystal structures of Lev and Eti are modified by increasing pressure, polycrystalline powder and single crystals. There are three important factors when we analyze and compare these two experiments: hydrostaticity, particle size and timeframe. The main pressure-related difference between these two samples is the hydrostatic conditions inside the diamond anvil cell. The hydrostatic pressure, or lack of, can induce or inhibit phase transformations.[49,50] Single crystal experiments are generally hydrostatic, up to a hydrostatic limit of the pressure-transmitting medium, but quasi-hydrostatic for powder samples. The difference is due to compaction of the powder where there are solid-solid interactions as well as solid-pressure transmitting medium interactions. The interaction of the solid with itself can induce strain and thus is only quasi-hydrostatic. Single-crystal samples are surrounded by a pressure transmitting medium hence there are only crystal/pressure-transmitting medium contacts limiting the strain imposed on the crystal. Particle size of the crystalline material and the timeframe of the experiment can dictate the nucleation rate of a transformation hence kinetics can play a significant role.[51] In this study, we collected the Raman spectra for powder sample over one day, whilst the single crystal data were collected over the course of 32 days due to the concurrent X-ray diffraction experiments that were being performed. Therefore, we cannot rule out the effect of the two different timescales on the results obtained. Raman spectra of the powder and single crystal sample of Lev and Eti are shown in Figure 4.18 & Figure 4.19. The Raman spectra of the samples at increased pressure have slightly broader peaks than the Raman spectra at atmospheric pressure which is a consequence of the stress applied to the sample. The increase of pressure induces a gradual shift of the vibrations below

3000 cm^{-1} towards higher wavenumbers (Figure 4.19a, b, d & e). The inverse trend is observed for the N-H stretching modes at approximately 3200 and 3367 cm^{-1} which progressively shift toward low-wavenumbers (Figure 4.19c & f**).** In particular for Lev, the vibration at 345 cm^{-1} (CC stretch + OCN bend and CCC bend) (Figure 4.19a) presents a slight discontinuity in the trend for the powder sample at about 2 GPa, which is not observed for single crystals; in Figure 4.19a, the symbols at 1.25 and 2 GPa overlap hence are depicted in a different color. This discontinuity is also observed for the OCNC torsion + CCN bend in Figure 4.19b. The characteristic of a powder sample is a high surface area hence high surface energy thereby increasing the possibility of a subtle transformation not detected for the single crystal sample. No discontinuity is observed in the shift of the N-H stretch with either powder or single crystals.

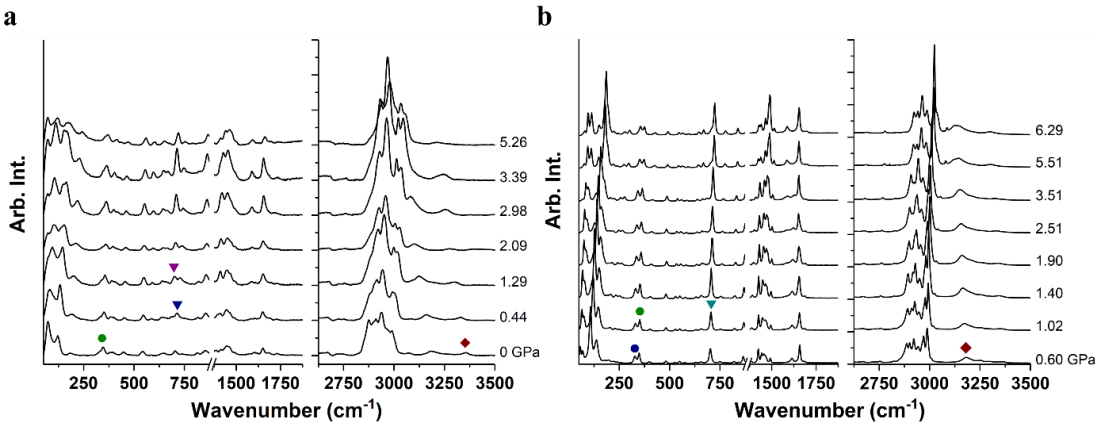

Figure 4.18. - a Raman spectra of powder sample of Lev during the compression to 5.26 GPa. The effect of pressure could be observed in several peaks such as at ●– *approx.* 345 cm^{-1}, ▼– *approx.* 690 cm^{-1},▼– *approx.* 700 cm^{-1} and ◆ – *approx.* 3360 cm^{-1}; **b** Raman spectra of single crystal of Eti during the compression to 6.29 GPa. The effect of pressure could be observed in several peaks such as at ● and ●– *approx.* 345 cm^{-1},▼– *approx.* 700 cm^{-1},◆ – *approx.* 3180 cm^{-1}.

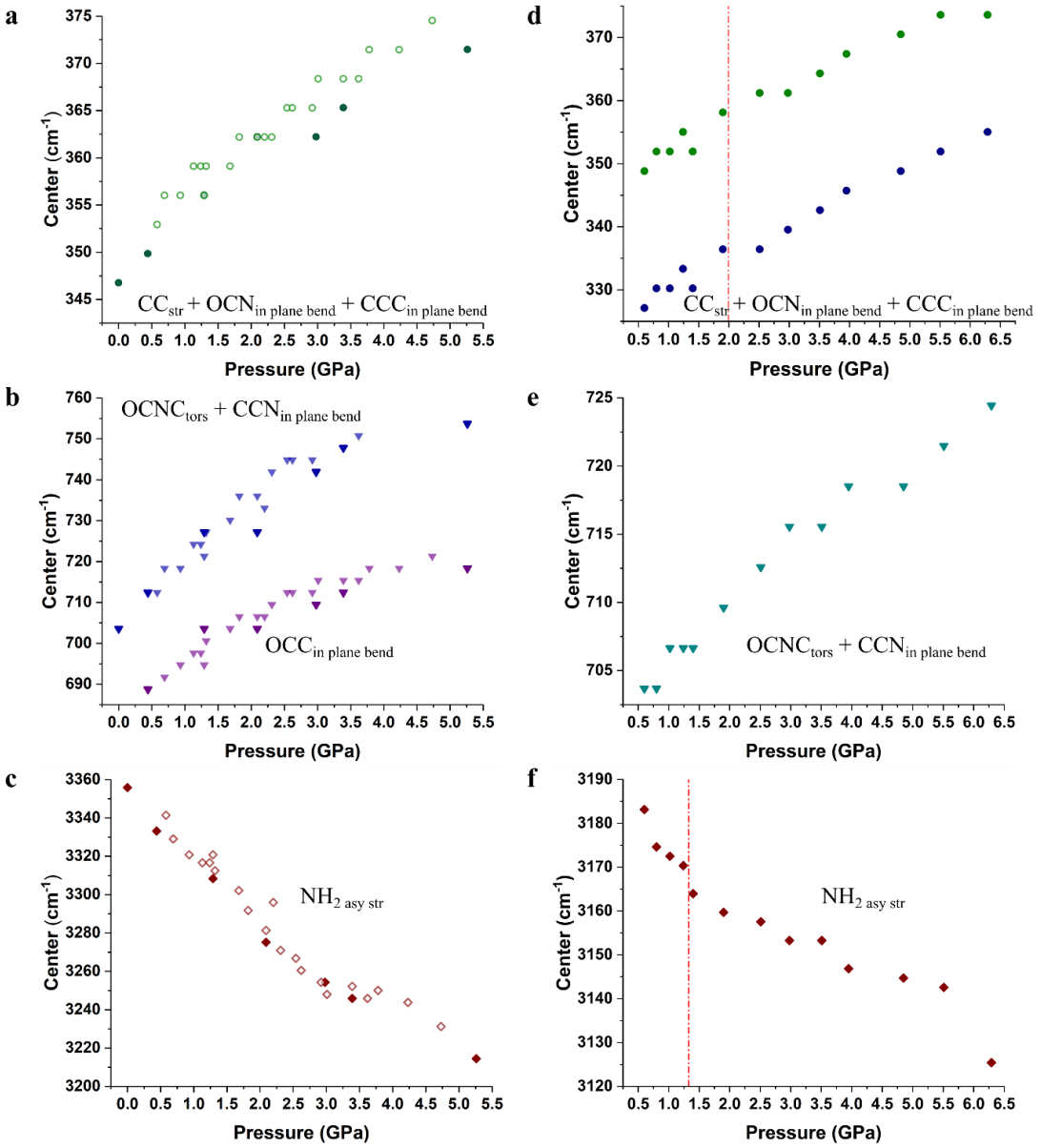

Figure 4.19. - **a-c** Evolution of center position of specific Raman peak for Lev at ●– *approx.* 345 cm^{-1}, ▼– *approx.* 690 cm^{-1},▼– *approx.* 700 cm^{-1} and ◆ – *approx.* 3360 cm^{-1}.during compression to 5.26 GPa. Peak observed in Raman spectra of powder (full symbols), single crystal samples (opened symbols) upon compression of the samples. At 1.25 and 2.1 GPa the data points of the single crystal and powder overlap hence they have a lighter color (light color symbols); **d-f** Evolution of center position of specific Raman peak for Eti at ● and ● – *approx.* 345 cm^{-1}, ▼– *approx.* 700 cm^{-1},◆ – *approx.* 3180 cm^{-1} during compression to 6.29 GPa.

As with Lev, we followed the compression of Eti form I using Raman spectroscopy and single-crystal X-ray diffraction from 0.60 to 6.29 GPa. Following the same approach used in the analysis of the vibrational spectra for Lev, three areas related with the hydrogen bond interactions were investigated to understand the effect of pressure in the structure of Eti. Figure 4.19d illustrates the effect of pressure on the vibrational mode of OCN bond. The frequency at 330 cm^{-1} shows a slight discontinuity above 2.0 GPa and the NH_2 stretch shows a change at 1.25 GPa (Figure 4.19f) indicating that there may be changes in structure at each of these points. These pressure zones were investigated carefully using X-ray diffraction with the goal to understand if any structural modification was induced by pressure.

4.4.3 Single crystal X-ray diffraction study of Levetiracetam and Etiracetam

The Raman data provided us with evidence that slight structural modifications could be occurring in Lev and Eti at higher pressures. For this reason, we collected single crystal diffraction data to verify the changes that may be occurring at the pressures identified in the Raman study. We compressed single crystals of Lev and Eti to 4.83 GPa and 6.29 GPa respectively. The limits of these studies were dictated by the quality of the diffraction pattern. For reference structures we used the literature structures with CSD refcodes OMIVUB[27] (Lev) and OFIQUR[26] (Eti). The changes in the unit cell parameters over the compression range studied are shown in Figure 4.20. The slight dispersion in the measurements for Lev using the three crystals can arise due to errors in pressure measuring (typically 0.05 GPa) as well as errors introduced as the data are collected in a diamond anvil cell. We do not have as many observations

as a normal crystallographic dataset to refine the cell parameters. Neutron powder diffraction would be the best technique for the evolution of cell parameters with pressure but was unavailable to us for this study. Nevertheless, in both instances the change of unit cell parameters with pressure show an anisotropic compression with higher compressibility in the *a*- axis (Lev, 11%) and *c*-axis (Eti, 12%) followed by the compression of *b*-axis (Lev, 7%; Eti 9%) followed by *c*-axis (Lev, 4%) and *a*-axis (Eti, 5%) Figure 4.20a & d. The β-angle reacts differently in each case where it increases by 0.6° until approximately 1.5 GPa where it plateaus in Lev (Figure 4.20b) but for Eti it decreases by 6° during compression (Figure 4.20e). The difference in behavior is linked to the direction of greatest compression with respect to the unit cell. Figure 4.21 shows the compression of the structure and the alignment of this with respect to the unit cell. For Lev, these directions are approximately aligned to the *a*- and *c*- directions of the unit cell hence there is little change in the β-angle whereas for Eti the compression are not so well aligned to the unit cell directions resulting in a greater β-angle change. The change in β-angle where it plateaus is also observed in compression of paracetamol[52] and RS-ibuprofen.[53]

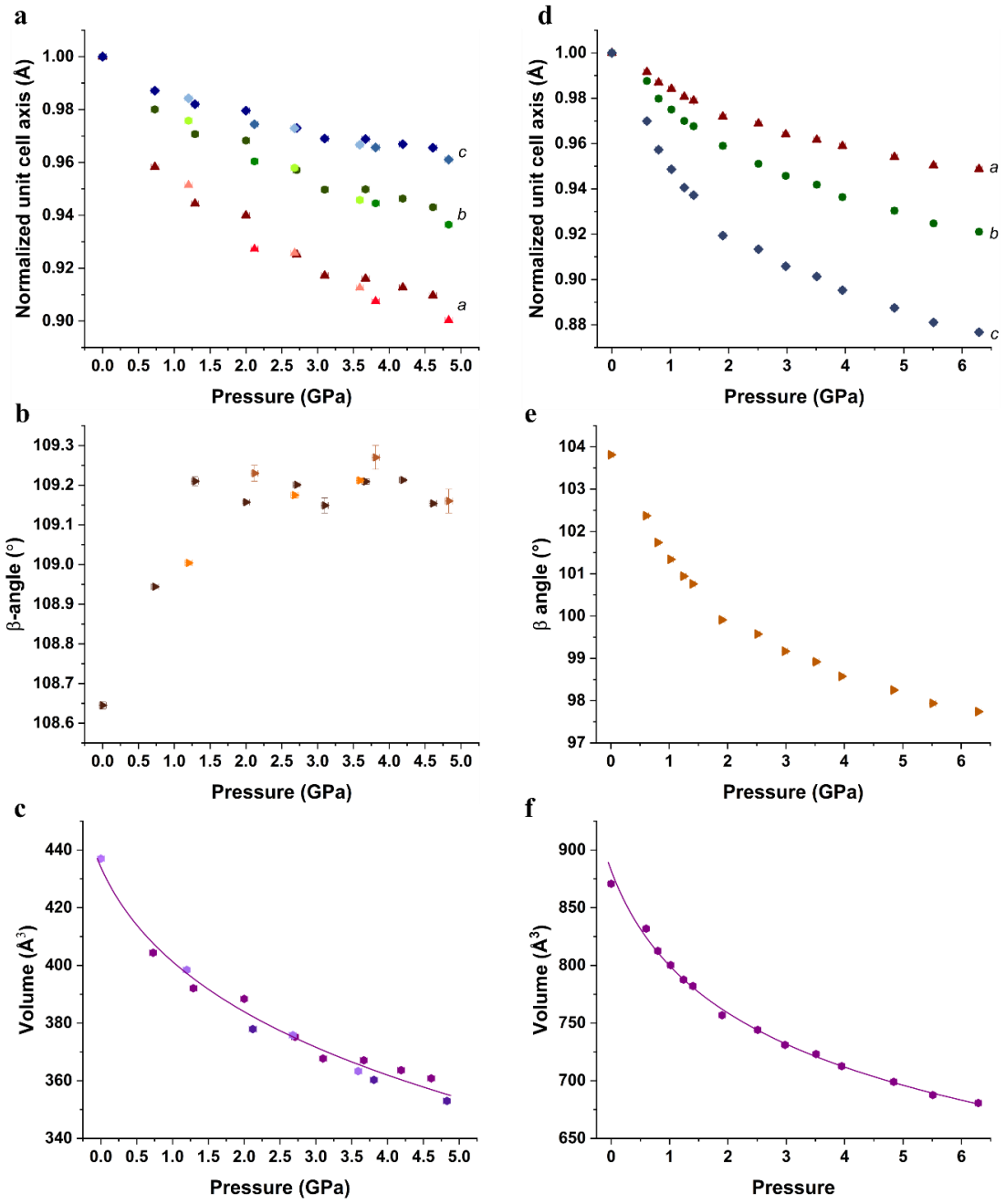

Figure 4.20 - X-ray diffraction compression data of **a-c** Lev and **d-f** Eti. **a)** & **d)** unit cell axis. **b** & **e** Variation of the β angle. **c** & **f** The Volume was fitted to the 3rd order Birch-Murnaghan for Lev and 3rd order Murnaghan Equation of State for Eti. The compression of LEV was performed using three crystals illustrated by solid symbol (crystal 1), open symbol (crystal 2) and half right solid (crystal 3) in compression data of **a** unit cell axis and by different shape of symbols in the **b** variation of the β angle and **c** volume, square in crystal 1; circle in crystal 2 and triangle in crystal 3.

The unit cell volumes are compressed by a similar extent (18% to 4.83 GPa; 22% to 4.84 GPa) as the unit cell parameters. We applied a 3rd order Birch-Murnaghan (BM) and Murnaghan (M) Equation of State (EoS) to each set of data and observed that the best fit was using a 3rd order BM for Lev (using data for all three crystals) and M EoS for Eti (Table 4.2). The refined EoS parameters are: bulk modulus (K_0) of 8(7) GPa with a V_0 = 434(14) Å^3 and K_0'=12(11) for Lev; bulk modulus (K_0) of 6.5(10) GPa with a V_0 = 882(8) Å^3 and K_0' = 8.5(4) for Eti. These parameters indicate that the crystal forms have a similar compressibility. As part of this study we determined the bulk modulus for four other pharmaceutically relevant molecules from literature values using EoSFIT7.0:[41] for piracetam (2rd order BM EoS, K_0=15(2));[54] paracetamol (3rd order BM EoS, K_0=16(10));[52] RS-ibuprofen (2rd order BM EoS, K_0=12.1(8));[53] and chlorothiazide form I (3rd order BM EoS, K_0=13(5)).[55] This analysis demonstrated that Lev is far more compressible than piracetam, paracetamol, RS-ibuprofen and chlorothiazide.

Whilst knowing how the unit cell compresses is important, the principal axis of strain is a better measure of how the solid reacts to compression. The strain tensor and compressibility indicatrix provides the directions in which the crystal structure is compressed which makes it more appropriate for the analysis of low symmetry triclinic and monoclinic systems as the unit cell angles are not necessarily 90°. The principal axis of strain for both crystal structures are presented in Figure 4.21 & Table 4.3. The red compressibility indicatrix for each phase is shown with the respect to the unit cell axis. From this analysis, we have superimposed the directions of compression onto the crystals structures using the red and blue arrows to aid our understanding of the compression.

Table 4.2. – The expression for the equation of states along with the parameters used in the fits along with χ^2 for each fit.

Expression of Bulk modulus

Birch-Murnaghan EoS:

$$P(V) = 3K_0 f_E(1+2f_E)^{\frac{5}{2}}\left(1+\frac{3}{2}(K_0'-4)f_E+\frac{3}{2}\left(K_0K_0''+(K_0'-4)(K_0'-3)+\frac{35}{9}\right)f_E^2\right)$$

where $f_E = \left[\left(\frac{V_0}{V}\right)^{2/3}-1\right]/2$

Murnaghan EoS:

$$P(V) = \frac{K_0}{K_0'}\left[\left(\frac{V_0}{V}\right)^{K_0'}-1\right]$$

	V_0 (Å^3)	K_0 (GPa)	K_0'	χ^2
Lev BM	434(14)	8(7)	12(12)	32.05
Lev M	432(10)	10(4)	8(2)	32.93
Eti BM	845 *	11.8(13)	8.6(16)	15.74
Eti M	882(8)	6.5(10)	8.5(4)	2.92

[i]where P is the pressure, V_0 is the reference volume, V is the volume at pressure, K_0 is the bulk modulus, and K_0' is the derivative of the bulk modulus with respect to pressure.*Refining the V_0 for Eti using BM EoS made the refinement unstable but included here to validate our choice of EoS expression.

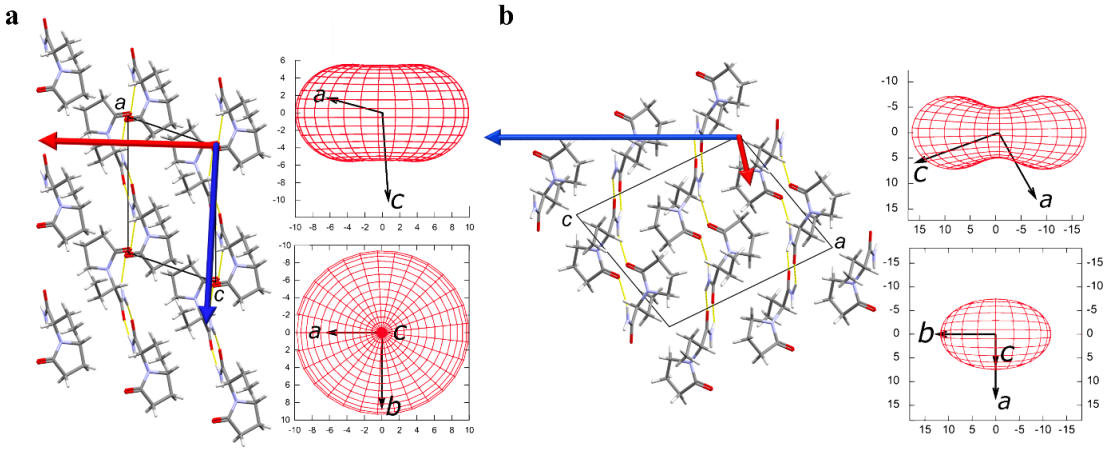

Figure 4.21 - Compressibility indicatrix for **a** Lev and **b** Eti calculated by PASCal together with a vector applied to the crystal structure to show how the crystal compresses (across *a*-axis in red and *c*-axis in blue).

Table 4.3.– Principal axis of strain for the crystal structure of Lev and Eti.

	Principal axis of strain					
	X_1 (TPa^{-1})		X_2 (TPa^{-1})		X_3 (TPa^{-1})	
	Direction	K (TPa^{-1})	Direction	K (TPa^{-1})	Direction	K (TPa^{-1})
Lev	[-0.99 0 -0.17]	11(3)	[0 1 0]	9.8(8)	[-0.11 0 -0.99]	5.4(5)
Eti	[-0.44 0 0.90]	18(1)	[0 -1 0]	11.7(5)	[0.91 0 0.42]	2.3(1)

The presence of layers in the crystal structures is characterized by weak interlayer van der Waals interactions, that can be observed in Lev and Eti. As expected, the most compressible direction for both compounds (Lev: [-0.99 0 -0.17]; Eti: [-0.44 0 0.90]) is almost perpendicular to the layers and the degree of compressibility depends on the geometry of the hydrogen bonding in the layers (Figure 4.21). In addition to the geometry we can correlate the weaker interactions and the layered nature of the structure with the position and percentage of voids in the crystal structure. The voids in the Lev structure are located between the layers that are translated along the *a*-axis **(**Figure 4.22a**)**. Eti form I shows the majority of the void space is between the stepped layers parallel to the (1 0 -1) plane (Figure 4.22b).

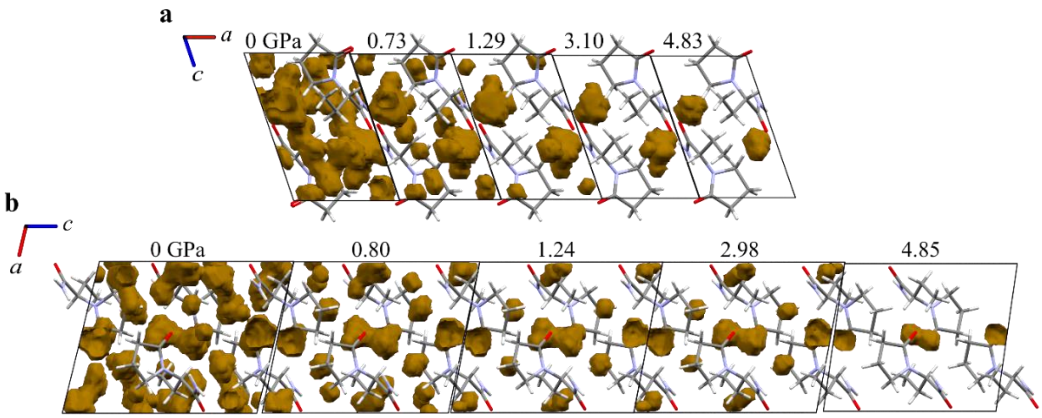

Figure 4.22 - The representation of voids in the crystal structure of Lev and Eti. **a** view along *b*-axis in the crystal structure of Lev and **b** along *b*-axis in the crystal structure of Eti. Parameters used for void calculation probe radius of 0.5 Å and grid spacing 0.2 Å.

On compression there is a general reduction of void volume in Lev (from 12.7 to 1.4 %) and the interlayer voids decrease over the compression range. However, even at the highest pressure there are still voids present in between the ethyl group of one layer and the amide of the second layer. This is due to the perpendicular orientation of the five membered ring with respect to the layer which prevents the molecules coming

closer together and reducing the voids. In contrast to Lev, the direction of the principal axis of strain in Eti contains a significant component of the *a*-and *c*-axis due to the layers being parallel to the (1 0 -1) plane as we discussed in relation to the *β*-angle. The majority of the voids in the crystal structure of Eti are between the stepped layers and are reduced substantially on compression and as a whole the volume decreases by 7.7%. The remaining void space is due to the orientation of the oxopyrrolidine ring and ethyl groups where they form the sides of a 'pocket' and limit the compression.

An unusual observation in the two structures, but common to both, is that the direction of the hydrogen bond ([0 1 0] or [0 -1 0]) is the second most compressible directions. We are able to rationalize this for each structure due to there being little intercalation of the molecules into the neighboring hydrogen-bonded chains. The lack of intercalation and geometry of the hydrogen bonding (sinusoidal pattern rather than a straight chain) permits the hydrogen-bonded chain to act as a spring; something that has been noted in other studies.[46,56] The remaining void volume in both systems, highlighted previously, are the remnants of the void between translated molecules in the hydrogen-bonded chain hence indicates the lack of intercalation. In Lev, the oxygen of the oxopyrrolidine group is the only part that is in the same plane as the neighboring chain hence has little impact on the compression along the bond.

The least compressible direction in Lev is along the [-0.11 0 -0.99] direction. As previously described, the hydrogen-bonded chains are positioned at a slight angle to the *c*-axis restricting the compression along the [-0.11 0 -0.99] direction. The ethyl group of one chain is in close contact with the oxopyrrolidine ring and at ambient pressure are close to the van der Waals radii for the groups. The structure compresses so that these groups interlock and prevent further compression along the *c*-direction.

In addition to this, the NH···O(py) hydrogen bond is also in this direction. It compresses at a similar rate to the other hydrogen bond in the system, 6.25% in NH···O(py) bond, compared with 7.02% in NH···O(CNH_2). For Eti the compression of structure in the [0.91 0 0.42] direction is much lower than Lev which can be attributed to the strong dimer interaction over the inversion center. Due to the symmetry there is necessarily a two-point contact between the molecules in the chains rather than the single hydrogen bond contact observed in Lev which provides a more robust interaction. As expected the hydrogen bonds were compressed with different rates, 4.25% in NH···O(py) and 8.18% in NH···O(CNH_2) hydrogen bonds.

4.4.4 Comparison of Levetiracetam and Etiracetam

We have investigated compression of 2-(2-oxo-1-pyrrolidinyl) butyramide as both the enantiopure and racemic solid forms to observe the similarities and differences of these materials when exposed to pressure including the potential to use pressure as a method of phase separation.

At basic level, we observe that the globularity and sphericity for Lev and Eti diverge slightly when compressed to 4.83 and 4.85 GPa, respectively (Table 4.4). The compression promotes a less spherical surface for both compounds. The molecular volume for Lev and Eti is also very similar at ambient pressure (Lev: 218.5 $Å^3$; Eti: 217.8 $Å^3$). On compression (Figure 4.23), the molecular volume for both forms is equivalent to approximately 1 GPa after which they deviate slightly. At higher pressures, the molecular volume of Eti is marginally lower than Lev which may indicate Eti increased stability with respect to Lev. Hence a conclusion from this work is that chiral resolution using pressure is not a viable method for this system. Pressure

has been used in the past to separate mandelic acid where the molecular volume of the chiral crystal is lower than that of the racemic crystal.[14]

Table 4.4. – Asphericity and globularity for the molecules in Lev and Eti crystal structures at atmospheric and high-pressure.

	Lev		Eti	
	0 GPa	4.83 GPa	0 GPa	4.85 GPa
Globularity	0.831	0.804	0.839	0.823
Sphericity	0.033	0.036	0.032	0.037

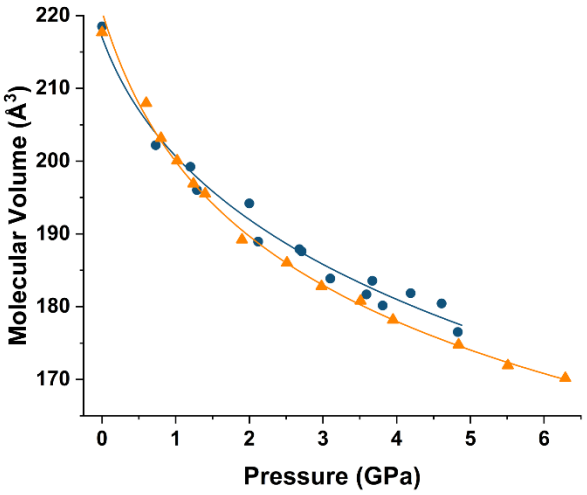

Figure 4.23 - Molecular volume (*V/Z*) for Eti (orange plot) and Lev (blue plot) as a function of pressure. The lines are only a guide for the visualization.

Until to this point, we discussed the compression of Lev and Eti as a progressive compression of the structure. However, there are some indications that imply a subtle phase transition where the structure rearranges slightly enough to stabilize at high-pressure. The Raman spectra of both compounds show a discontinuity in the increase of frequency with increasing of pressure (Figure 4.19) as described in previous sections. We have plotted the percentage change in length for both Lev and Eti in Figure 4.24. This plot highlights the small discontinuities on the compression of Lev after 2 GPa and in Eti after 1.5 GPa. For Lev, we have plotted all the datasets for

the three single crystals measured and it can be observed that there are discontinuities in each of the cell axes. The plot for Eti is less clear but the *c*-axis shows the greatest change over the pressure range. Superimposed on these graphs are the adjusted lattice energies for the structures as calculated using PIXEL.[57–59] These energies take into account the intermolecular energies but also the change in the molecular energy following procedures in Johnstone et al.[60] The lattice energy for Levetiracetam shows a distinct change over the pressure range of the discontinuity in the lattice parameters. The lattice energy of Etiracetam does not show a distinct discontinuity but there is a change in gradient of the slope at the pressure of the suspected transition. From these additional observations, we will tentatively identify these as Form II of Levetiracetam and Form III of Etiracetam. These boundaries are our best estimate given the data we have collected. Neutron powder diffraction would provide an opportunity to define these boundaries with increased precision.

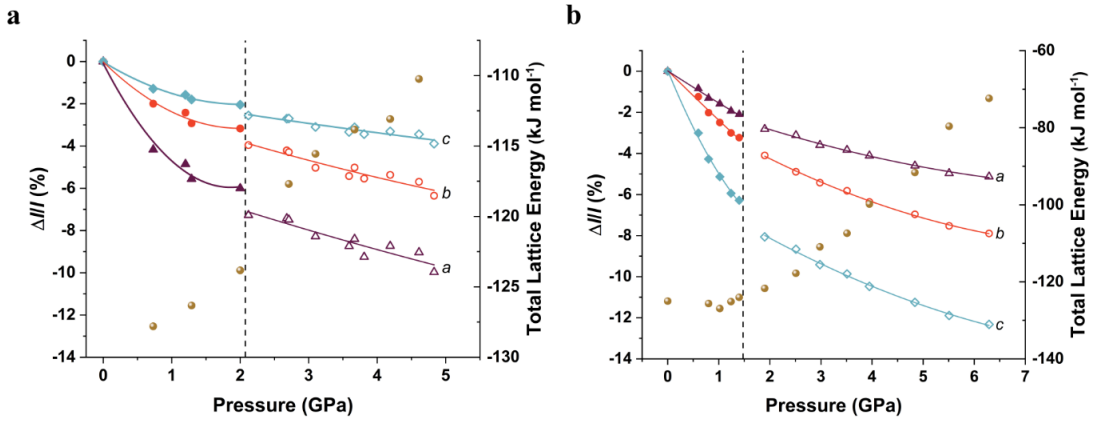

Figure 4.24 - Variation of unit cell lengths as a percentage change together with the adjusted total lattice energies for **a** Lev (all data) and **b** Eti as a function of pressure. The discontinuities in the region of 2 GPa and 1.5 GPa can be seen in Lev and Eti respectively. Lines are polynomials as guide to eye.

A more in-depth investigation into the potential phase transitions at the molecular level reveals that there are changes in the intermolecular interactions over

the 'phase transition' pressure (CrystalExplorer[40]). The interactions between molecules in translated layers (between the central molecule and the blue and red molecules in Figure 4.25) show a relieving of repulsive energies over the transition pressure whilst this is not evident in the interactions between molecules in the hydrogen-bonded chain using the amide moieties (purple molecule).

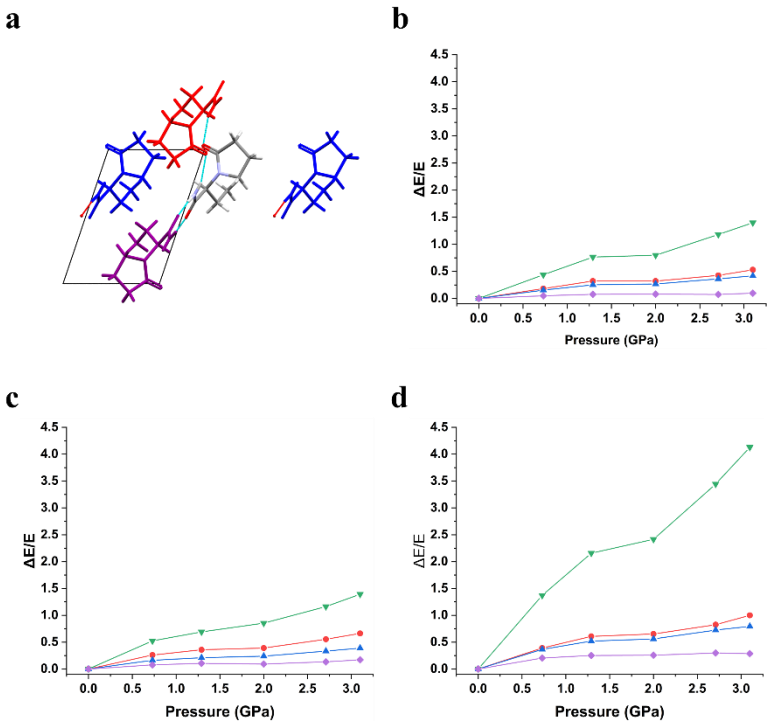

Figure 4.25 - Energy of molecular interactions in Lev illustrated by **a** molecular packing diagram surrounding the element colored molecule with **b** red molecule interaction energies (amide-oxopyrrolidine hydrogen bond), **c** purple molecule interaction energies (amide-amide hydrogen bond) and **d** blue molecule interaction energies (interlayer interaction). Green – repulsion energy, blue – dispersion energy, red – polarization energy and violet- total energy.

Overall for Eti, there is a very small difference in the unit cell parameters where the *c*-axis varies the most over the possible transition. The interactions between hydrogen-bonded dimer, chain, and layer indicate a slight change in total energy that is driven by a variation in the polarization energy over the transition pressure (Figure 4.26). The relieving of repulsive energies for interactions between hydrogen-bonded

dimer and chain are not as pronounced as Lev whilst the interactions between layers shows no discontinuity. That the hydrogen-bonded dimers are showing the greatest changes in the intermolecular energies can be rationalized through the direction of the hydrogen-bonded dimer has a component of the *c*-direction. It is clear from Figure 4.26 that the polarization component of the molecules in the layer are affected at the same pressure whereas the interlayer interaction polarization changes at a higher pressure. Ultimately, the changes are so small that any difficulties in refinement will change the intermolecular interactions which is particularly important given that this is refined using high pressure data.

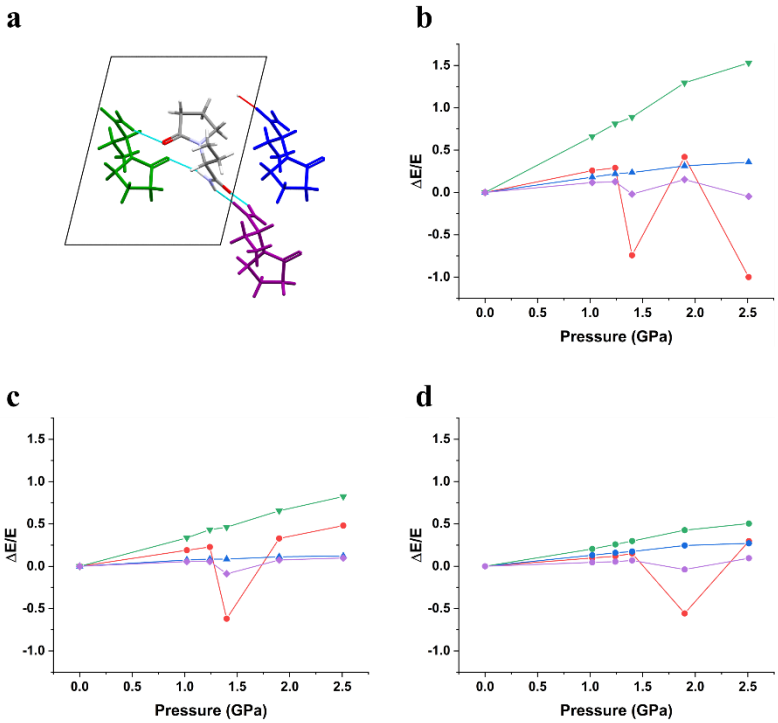

Figure 4.26 - Energy of molecular interactions in Eti illustrated by **a** molecular packing diagram surrounding the element colored molecule with **b** green molecule interaction energies (amide-oxopyrrolidine hydrogen bond dimer), **c** purple molecule interaction energies (amide-amide hydrogen bond) and **d** blue molecule interaction energies (interlayer interaction). Green – repulsion energy, blue – dispersion energy, red – polarization energy and violet- total energy.

4.5 Conclusion

We have discussed the effect of high pressure on the structure of Eti (racemic compound) and Lev (enantiopure crystal of the S-enantiomer). Both compounds showed an anisotropic strain compression where the most compressible axis is determined by the presence of van der Waals interaction between layers. Nonetheless, the compression of both compounds is not linear. The Raman spectroscopy analysis highlights that there is a possible phase transition in Lev (*approx*. 2GPa) to Form II and Eti (*approx*. 1.5GPa) to Form III. These observations are supported by the analysis of the change of unit cell parameters as a function of pressure as well as the change in lattice energies and corresponding intermolecular energies over the transition. In Lev, we observe that the repulsive energy of some of the interlayer interactions is relieved over the transition whilst the interlayer hydrogen--bonded molecules show no such relief. With respect to the preferential crystallisation at high-pressure of the chiral compound, Eti shows an increase of density up to 1.7% at 4.8GPa in relation to Lev. This factor makes the spontaneous resolution through high pressure unlikely.

4.6 Acknowledgement

We would like to thank Professor Tom Leyssens from University of Louvain for supplying the project with samples of Levetiracetam and Etiracetam and Dr Martin R. Ward for useful discussions and help with data collection.

We would like to thank the EPSRC (Grant Ref: EP/N015401/1) and the Doctoral Training Centre in Continuous Manufacturing and Crystallisation (Grant Ref: EP/K503289/1) and the Centre for Innovative Manufacturing in Continuous Manufacturing and Crystallisation (Grant Ref: EP/I033459/1) for funding this work.

We would like to acknowledge that this work was carried out in the CMAC National Facility supported by UKRPIF (UK Research Partnership Fund) award from the Higher Education Funding Council for England (HEFCE) (Grant Ref: HH13054).

4.7 References

(1) Haleblian, J.; McCrone, W. Pharmaceutical Applications of Polymorphism. *Journal of Pharmaceutical Sciences*. 1969, pp 911–929. https://doi.org/10.1002/jps.2600580802.

(2) Brittain, H. G. *Polymorphism in Pharmaceutical Solids: Second Edition*, 2nd Editio.; CRC Press, 2009. https://doi.org/10.3109/9781420073225.

(3) Yu, L.; Reutzel, S. M.; Stephenson, G. A. Physical Characterization of Polymorphic Drugs: An Integrated Characterization Strategy. *Pharmaceutical Science and Technology Today*. June 1, 1998, pp 118–127. https://doi.org/10.1016/S1461-5347(98)00031-5.

(4) Nguyen, L. A.; He, H.; Pham-Huy, C. Chiral Drugs: An Overview. *Int. J. Biomed. Sci.* **2006**, *2* (2), 85–100.

(5) Lorenz, H.; Perlberg, A.; Sapoundjiev, D.; Elsner, M. P.; Seidel-Morgenstern, A. Crystallization of Enantiomers. *Chem. Eng. Process. Process Intensif.* **2006**, *45* (10), 863–873. https://doi.org/10.1016/j.cep.2005.11.013.

(6) Lorenz, H.; Seidel-Morgenstern, A. Processes To Separate Enantiomers. *Angew. Chemie Int. Ed.* **2014**, *53* (5), 1218–1250. https://doi.org/10.1002/anie.201302823.

(7) Wechter, W. J.; Bigornia, A. E.; Murray, E. D.; Levine, B. H.; Young, J. W. Rac-Flurbiprofen Is More Ulcerogenic than Its (S)-Enantiomer. *Chirality* **1993**,

5 (7), 492–494. https://doi.org/10.1002/chir.530050703.

(8) Islam, M. R.; Mahdi, J. G.; Bowen, I. D. Pharmacological Importance of Stereochemical Resolution of Enantiomeric Drugs. *Drug Saf.* **1997**, *17* (3), 149–165. https://doi.org/10.2165/00002018-199717030-00002.

(9) Bordallo, H. N.; Kolesov, B. A.; Boldyreva, E. V.; Juranyi, F. Different Dynamics of Chiral and Racemic (L- and DL-) Serine Crystals: Evidenced by Incoherent Inelastic Neutron and Raman Scattering. *J. Am. Chem. Soc.* **2007**, *129* (36), 10984–10985. https://doi.org/10.1021/ja073351n.

(10) Zakharov, B. A.; Kolesov, B. A.; Boldyreva, E. V. Effect of Pressure on Crystalline L- and Dl-Serine: Revisited by a Combined Single-Crystal X-Ray Diffraction at a Laboratory Source and Polarized Raman Spectroscopy Study. *Acta Crystallogr. Sect. B Struct. Sci.* **2012**, *68* (3), 275–286. https://doi.org/10.1107/S0108768112015960.

(11) Minkov, V. S.; Krylov, A. S.; Boldyreva, E. V.; Goryainov, S. V.; Bizyaev, S. N.; Vtyurin, A. N. Pressure-Induced Phase Transitions in Crystalline <scp>l</Scp> - and <scp>dl</Scp> -Cysteine. *J. Phys. Chem. B* **2008**, *112* (30), 8851–8854. https://doi.org/10.1021/jp8020276.

(12) Görbitz, C. H. Crystal Structures of Amino Acids: From Bond Lengths in Glycine to Metal Complexes and High-Pressure Polymorphs. *Crystallogr. Rev.* **2015**, *21* (3), 160–212. https://doi.org/10.1080/0889311X.2014.964229.

(13) Moggach, S. A.; Parsons, S.; Wood, P. A. High-Pressure Polymorphism in Amino Acids. *Crystallogr. Rev.* **2008**, *14* (2), 143–184. https://doi.org/10.1080/08893110802037945.

(14) Rietveld, I. B.; Barrio, M.; Tamarit, J. L.; Do, B.; Céolin, R. Enantiomer

Resolution by Pressure Increase: Inferences from Experimental and Topological Results for the Binary Enantiomer System (R)- and (S)-Mandelic Acid. *J. Phys. Chem. B* **2011**, *115* (49), 14698–14703. https://doi.org/10.1021/jp209328d.

(15) Cai, W.; Marciniak, J.; Andrzejewski, M.; Katrusiak, A. Pressure Effect on <scp>d,L</Scp> -Mandelic Acid Racemate Crystallization. *J. Phys. Chem. C* **2013**, *117* (14), 7279–7285. https://doi.org/10.1021/jp401626a.

(16) Marciniak, J.; Andrzejewski, M.; Cai, W.; Katrusiak, A. Wallach's Rule Enforced by Pressure in Mandelic Acid. *J. Phys. Chem. C* **2014**, *118* (8), 4309–4313. https://doi.org/10.1021/jp411738p.

(17) Roszak, K.; Katrusiak, A. High-Pressure and Temperature Dependence of the Spontaneous Resolution of 1,1′-Binaphthyl Enantiomers. *Phys. Chem. Chem. Phys.* **2018**, *20* (7), 5305–5311. https://doi.org/10.1039/c7cp07234a.

(18) Fabbiani, F. P. A.; Allan, D. R.; Parsons, S.; Pulham, C. R. An Exploration of the Polymorphism of Piracetam Using High Pressure. *Crystengcomm* **2005**, *7*, 179–186. https://doi.org/10.1039/b418976k.

(19) Fabbiani, F. P. A. A.; Allan, D. R.; David, W. I. F. F.; Davidson, A. J.; Lennie, A. R.; Parsons, S.; Pulham, C. R.; Warren, J. E. High-Pressure Studies of Pharmaceuticals: An Exploration of the Behavior of Piracetam. *Cryst. Growth Des.* **2007**, *7* (6), 1115–1124. https://doi.org/10.1021/cg0607710.

(20) Admiraal, G.; Eikelenboom, J. C.; Vos, A. Structures of the Triclinic and Monoclinic Modifications of (2-Oxo-1-Pyrrolidinyl)Acetamide. *Acta Crystallogr. Sect. B Struct. Crystallogr. Cryst. Chem.* **1982**, *38* (10), 2600–2605. https://doi.org/10.1107/s0567740882009431.

(21) Bandoli, G.; Clemente, D. A.; Grassi, A.; Pappalardo, G. C. Molecular Determinants for Drug-Receptor Interactions. 1. Solid-State Structure and Conformation of the Novel Nootropic Agent 2-Pyrrolidone-N-Acetamide: X-Ray and Theoretical SCF-MO Studies. *Mol. Pharmacol.* **1981**, *20* (3), 558–564.

(22) Picciochi, R.; Diogo, H. P.; Minas Da Piedade, M. E. Thermodynamic Characterization of Three Polymorphic Forms of Piracetam. *J. Pharm. Sci.* **2011**, *100* (2), 594–603. https://doi.org/10.1002/jps.22294.

(23) Toscani, S.; Céolin, R.; Ter Minassian, L.; Barrio, M.; Veglio, N.; Tamarit, J. L.; Louër, D.; Rietveld, I. B. Stability Hierarchy between Piracetam Forms I, II, and III from Experimental Pressure-Temperature Diagrams and Topological Inferences. *Int. J. Pharm.* **2016**, *497* (1–2), 96–105. https://doi.org/10.1016/j.ijpharm.2015.11.036.

(24) Fabbiani, F. P. A.; Allan, D. R.; David, W. I. F.; Davidson, A. J.; Lennie, A. R.; Parsons, S.; Pulham, C. R.; Warren, J. E. High-Pressure Studies of Pharmaceuticals: An Exploration of the Behavior of Piracetam. *Cryst. Growth Des.* **2007**, *7* (6), 1115–1124. https://doi.org/10.1021/cg0607710.

(25) Fabbiani, F. P. A.; Allan, D. R.; Parsons, S.; Pulham, C. R. An Exploration of the Polymorphism of Piracetam Using High Pressure. *CrystEngComm* **2005**, *7* (29), 179. https://doi.org/10.1039/b418976k.

(26) Herman, C.; Vermylen, V.; Norberg, B.; Wouters, J.; Leyssens, T. The Importance of Screening Solid-State Phases of a Racemic Modification of a Chiral Drug: Thermodynamic and Structural Characterization of Solid-State Phases of Etiracetam. *Acta Crystallogr. Sect. B Struct. Sci. Cryst. Eng. Mater.* **2013**, *69* (4), 371–378. https://doi.org/10.1107/S2052519213015054.

(27) Song, J.; Lou, K. X.; Li, X. J.; Wu, X. P.; Feng, R. X. 2-(2-Oxopyrrolidin-1-Yl)Butyramide. *Acta Crystallogr. Sect. E Struct. Reports Online* **2003**, *59* (11). https://doi.org/10.1107/S1600536803022578.

(28) Xu, K.; Xiong, X.; Guo, L.; Wang, L.; Li, S.; Tang, P.; Yan, J.; Wu, D.; Li, H. An Investigation into the Polymorphism and Crystallization of Levetiracetam and the Stability of Its Solid Form. *J. Pharm. Sci.* **2015**, *104* (12), 4123–4131. https://doi.org/10.1002/jps.24628.

(29) Moggach, S. A.; Allan, D. R.; Parsons, S.; Warren, J. E. Incorporation of a New Design of Backing Seat and Anvil in a Merrill-Bassett Diamond Anvil Cell. *J. Appl. Crystallogr.* **2008**, *41*, 249–251. https://doi.org/10.1107/s0021889808000514.

(30) Piermarini, G. J.; Block, S.; Barnett, J. D.; Forman, R. A. Calibration of the Pressure Dependence of the R 1 Ruby Fluorescence Line to 195 Kbar. *J. Appl. Phys.* **1975**, *46* (6), 2774–2780. https://doi.org/10.1063/1.321957.

(31) Dawson, A.; Allan, D. R.; Parsons, S.; Ruf, M. Use of a CCD Diffractometer in Crystal Structure Determinations at High Pressure. *J. Appl. Crystallogr.* **2004**, *37* (3), 410–416. https://doi.org/doi:10.1107/S0021889804007149.

(32) Inc. Bruker AXS; APEX 3. Madison, Wisconsin, USA 2017.

(33) Inc. Bruker AXS; SAINT Version 7. Madison, Wisconsin, USA 2003.

(34) Parsons, S. SHADE. Program for Empirical Absorption Corrections to High Pressure Data. The University of Edinburgh: UK 2004.

(35) Dolomanov, O. V.; Bourhis, L. J.; Gildea, R. J.; Howard, J. A. K. K.; Puschmann, H. OLEX2 : A Complete Structure Solution, Refinement and Analysis Program. *J. Appl. Crystallogr.* **2009**, *42* (2), 339–341.

https://doi.org/10.1107/S0021889808042726.

(36) Sheldrick, G. M. Crystal Structure Refinement with SHELXL. *Acta Crystallogr. Sect. C Struct. Chem.* **2015**, *71*. https://doi.org/10.1107/S2053229614024218.

(37) Groom, C. R.; Bruno, I. J.; Lightfoot, M. P.; Ward, S. C. The Cambridge Structural Database. *Acta Crystallogr. Sect. B Struct. Sci. Cryst. Eng. Mater.* **2016**, *72* (2), 171–179. https://doi.org/10.1107/S2052520616003954.

(38) Macrae, C. F.; Bruno, I. J.; Chisholm, J. A.; Edgington, P. R.; McCabe, P.; Pidcock, E.; Rodriguez-Monge, L.; Taylor, R.; Van De Streek, J.; Wood, P. A. Mercury CSD 2.0 - New Features for the Visualization and Investigation of Crystal Structures. *J. Appl. Crystallogr.* **2008**, *41* (2), 466–470. https://doi.org/doi:10.1107/S0021889807067908.

(39) Thorn, A.; Dittrich, B.; Sheldrick, G. M. Enhanced Rigid-Bond Restraints. *Acta Crystallogr. Sect. A Found. Crystallogr.* **2012**, *68* (4), 448–451. https://doi.org/10.1107/S0108767312014535.

(40) Turner, M. J.; McKinnon, J. J.; Wolff, S. K.; Grimwood, D. J.; Spackman, P. R.; Jayatilaka, D.; Spackman, M. A. . CrystalExplorer17. University of Western Australia 2017.

(41) Gonzalez-Platas, J.; Alvaro, M.; Nestola, F.; Angel, R. EosFit7-GUI: A New Graphical User Interface for Equation of State Calculations, Analyses and Teaching. *J. Appl. Crystallogr.* **2016**, *49* (4), 1377–1382. https://doi.org/10.1107/S1600576716008050.

(42) Cliffe, M. J.; Goodwin, A. L. PASCal: A Principal Axis Strain Calculator for Thermal Expansion and Compressibility Determination. *J. Appl. Crystallogr.*

2012, *45* (6), 1321–1329. https://doi.org/10.1107/S0021889812043026.

(43) Momma, K.; Izumi, F. VESTA 3 for Three-Dimensional Visualization of Crystal, Volumetric and Morphology Data. *J. Appl. Crystallogr.* **2011**, *44* (6), 1272–1276. https://doi.org/doi:10.1107/S0021889811038970.

(44) Spackman, M. A.; Byrom, P. G. A Novel Definition of a Molecule in a Crystal. *Chem. Phys. Lett.* **1997**, *267* (3–4), 215–220. https://doi.org/10.1016/S0009-2614(97)00100-0.

(45) Hirshfeld, F. L. Bonded-Atom Fragments for Describing Molecular Charge Densities. *Theor. Chim. Acta* **1977**, *44* (2), 129–138. https://doi.org/10.1007/BF00549096.

(46) Connor, L. E.; Delori, A.; Hutchison, I. B.; Nic Daeid, N.; Sutcliffe, O. B.; Oswald, I. D. H. The Ecstasy and the Agony; Compression Studies of 3,4-Methylenedioxymethamphetamine (MDMA). *Acta Crystallogr. Sect. B Struct. Sci. Cryst. Eng. Mater.* **2015**, *71* (1), 3–9. https://doi.org/10.1107/S2052520614026389.

(47) Johnstone, R. D. L.; Lennie, A. R.; Parsons, S.; Pidcock, E.; Warren, J. E. Comparison of the Effects of Pressure on Three Layered Hydrates: A Partially Successful Attempt to Predict a High-Pressure Phase Transition. *Acta Crystallogr. Sect. B-Structural Sci.* **2009**, *65* (6), 731–748. https://doi.org/10.1107/S0108768109039469.

(48) Ramya, T.; Gunasekaran, S.; Ramkumaar, G. R. Molecular Structure, Spectroscopic Characterization of (S)-2-Oxopyrrolidin-1-Yl Butanamide and Ab Initio, DFT Based Quantum Chemical Calculations. *Spectrochim. Acta - Part A Mol. Biomol. Spectrosc.* **2015**, *149*, 132–142.

https://doi.org/10.1016/j.saa.2015.04.033.

(49) Yoo, C. S.; Cynn, H. Equation of State, Phase Transition, Decomposition of β-HMX (Octahydro-1,3,5,7-Tetranitro-1,3,5,7-Tetrazocine) at High Pressures. *J. Chem. Phys.* **1999**, *111* (22), 10229–10235. https://doi.org/10.1063/1.480341.

(50) Liu, X.; Bull, C. L.; Kleppe, A. K.; Dowding, P. J.; Lewtas, K.; Pulham, C. R. High-Pressure Crystallisation Studies of Biodiesel and Methyl Stearate. *CrystEngComm* **2019**, *21* (30), 4427–4436. https://doi.org/10.1039/c9ce00393b.

(51) Hutchison, I. B.; Delori, A.; Wang, X.; Kamenev, K. V.; Urquhart, A. J.; Oswald, I. D. H. Polymorphism of a Polymer Precursor: Metastable Glycolide Polymorph Recovered via Large Scale High-Pressure Experiments. *CrystEngComm* **2015**, *17* (8), 1778–1782. https://doi.org/10.1039/C5CE00119F.

(52) Oswald, I. D. H.; Motherwell, W. D. S.; Parsons, S.; Pulham, C. R. A Paracetamol–Morpholine Adduct. *Acta Crystallographica Section E Structure Reports Online*. 2002, pp o1290–o1292. https://doi.org/10.1107/S1600536802018111.

(53) Ostrowska, K.; Kropidowska, M.; Katrusiak, A. High-Pressure Crystallization and Structural Transformations in Compressed R, S -Ibuprofen. *Cryst. Growth Des.* **2015**, *15* (3), 1512–1517. https://doi.org/10.1021/cg5018888.

(54) Fabbiani, F. P. A.; Allan, D. R.; David, W. I. F.; Davidson, A. J.; Lennie, A. R.; Parsons, S.; Pulham, C. R.; Warren, J. E. High-Pressure Studies of Pharmaceuticals: An Exploration of the Behavior of Piracetam. *Cryst. Growth Des.* **2007**, *7* (6), 1115–1124. https://doi.org/10.1021/cg0607710.

(55) Oswald, I. D. H.; Lennie, A. R.; Pulham, C. R.; Shankland, K. High-Pressure Structural Studies of the Pharmaceutical, Chlorothiazide. *CrystEngComm* **2010**, *12* (9), 2533. https://doi.org/10.1039/c001355b.

(56) Hutchison, I. B.; Bull, C. L.; Marshall, W. G.; Urquhart, A. J.; Oswald, I. D. H. Pressure-Induced Polymorphism of Caprolactam: A Neutron Diffraction Study. *Molecules* **2019**, *24* (11). https://doi.org/10.3390/molecules24112174.

(57) Gavezzotti, A. Efficient Computer Modeling of Organic Materials. The Atom-Atom, Coulomb-London-Pauli (AA-CLP) Model for Intermolecular Electrostatic-Polarization, Dispersion and Repulsion Energies. *New J. Chem.* **2011**, *35* (7), 1360–1368. https://doi.org/10.1039/C0NJ00982B.

(58) Gavezzotti, A. Non-Conventional Bonding between Organic Molecules. The "Halogen Bond" in Crystalline Systems. *Mol. Phys.* **2008**, *106* (12–13), 1473–1485. https://doi.org/Doi 10.1080/00268970802060674.

(59) Reeves, M. G.; Wood, P. A.; Parsons, S. MrPIXEL: Automated Execution of Pixel Calculations via the Mercury Interface. https://doi.org/10.1107/S1600576720008444.

(60) Johnstone, R. D. L.; Francis, D.; Lennie, A. R.; Marshall, W. G.; Moggach, S. A.; Parsons, S.; Pidcock, E.; Warren, J. E. High-Pressure Polymorphism in L-Serine Monohydrate: Identification of Driving Forces in High Pressure Phase Transitions and Possible Implications for Pressure-Induced Protein Denaturation. *CrystEngComm* **2008**, *10* (12), 1758–1769.

Chapter 5

A New High-pressure Form of Hydrochlorothiazide

5.1 Abstract

Crystallisation is a method of separation and purification widely applied in the fine chemical, food and pharmaceutical industries. Different methodologies have been applied in a crystallisation process depending on the opportunity to generate a driving force for crystallisation. For example, varying concentration and solubility in a system by evaporation of solvent or increase of temperature can increase the driving force for crystallisation; which are applied in evaporative and cooling crystallisation, respectively. The variation of pressure can also increase the driving force for crystallisation by decrease the molecular volume of the compound.

Recently, the variation of pressure in liquid, solution and solid systems has been applied to access new crystal forms. The effects of pressure on the crystal structure can be characterized *in-situ* using single-crystal X-ray diffraction and Raman Spectroscopy which enables the investigation of intramolecular and intermolecular modification during crystal transformation.

In this work, we studied the compound Hydrochlorothiazide (HCT) at high-pressure using diamond anvil cell and large volume press equipment. It was possible to generate a new high-pressure polymorphic form through a reconstructive phase transition. This form was recovered at ambient conditions, remaining stable at these conditions. Due to the irreversible transition to the stable form in a low range of

pressure, this system turned to be unsuitable for nucleation studies. However, the high-pressure form is kinetically stable for long periods at ambient condition (months), which presents an opportunity to explore the use of high-pressure polymorph seeds to feed a crystallisation process at ambient conditions. For this reason, we focused this study to the characterisation of the new polymorphic form which was carried out through Raman spectroscopy, X-ray powder diffraction and differential scanning calorimetry. The transition to a new high-pressure form resulted in the alteration of space group symmetry and perhaps an emphasis of packing interaction.

5.2 Introduction

Pressure as a thermodynamic parameter can be used to induce solid-solid transitions and nucleation from solution.[1–7] The formation of new polymorphic forms at high pressure can be dictated by several experimental conditions. The selection of initial material i.e. single-crystal or powder sample; the rate of compression[8,9]; the pressure-transmitting medium[10,11]; and the time that a sample is kept at the same pressure [12,13] may generate a new high-pressure form. Recent studies on materials at high pressure have been guided by Crystal Structure Prediction where potential valid polymorphs of materials have been computationally observed. The validity of forms is assessed based on the lattice energy of the forms and the crystal structure density.[14,15]

Nucleation takes an essential role in crystallisation by determining important material properties such as crystal form and crystal size distribution (CSD). The big challenge in understanding nucleation events is the small size of the nucleus that usually falls in the range of 1-1000 molecules and the time scale of generating a nucleus ranges from less than a second to days.[16] Moreover, nucleation is a stochastic

event that can occur spontaneously or induced by foreign particles (impurities or surfaces). The study of nucleation is a challenge due to the wide range of induction period and difficulty to eliminate foreign particles. Nucleation can be induced by a change in the environment of the solution or crystalline phase (e.g. temperature). Other methods of inducing nucleation are the use of pressure where the volume of the system is reduced, promoting the formation of the solid state over remaining in the liquid phase.

Chlorothiazide (CTZ; Figure 5.1a), 6-Chloro-4H-1,2,4-benzothiadiazine-7-sulfonamide 1,1-dioxide is an active pharmaceutical ingredient (API) applied to diuretic therapy. This compound is very interesting because although the potential for new polymorphic forms showed in Crystal Structure Prediction (CSP) studies,[17,18] no polymorphic form was found by cooling and evaporation crystallisation. However, Oswald et *al* identified and characterized a new polymorphic form for CTZ at 4.4 GPa.[7] This polymorph is a consequence of an isostructural phase transition, where the molecular conformation changes slightly due to the interaction between the sulfonic group and the thiazide ring system of a neighbouring molecule resulting in the deformation of the ring; the sulfonamide group also showed a change of the torsion angle due to shear of the molecular layers. The isostructural phase transition is shown to be reversible at 4.2 GPa through decompression. This type of transition is exactly the type that we wished to investigate for our nucleation studies at pressure as we had the requirement that the phase transition is reversible however the pressure at which it occurred was too high for the pressure to be easily controlled.

The behaviour of CTZ under pressure suggested that HCT may be an interesting candidate for a nucleation study at high-pressure. Besides, HCT presents a rich

polymorphic behaviour with four potential forms[19–23] of which only three have been characterised structurally at ambient conditions.[17,21,23] Hydrochlorothiazide (HCT; Figure 5.1b), 6-Chloro-3,4-dihydro-2H-1,2,4-benzothiadiazine-7-sulfonamide 1,1-dioxide is a diuretic agent as CTZ. The molecular structures of CTZ and HCT differ in the thiazide ring, which is saturated in the case of HCT, Figure 5.[19]

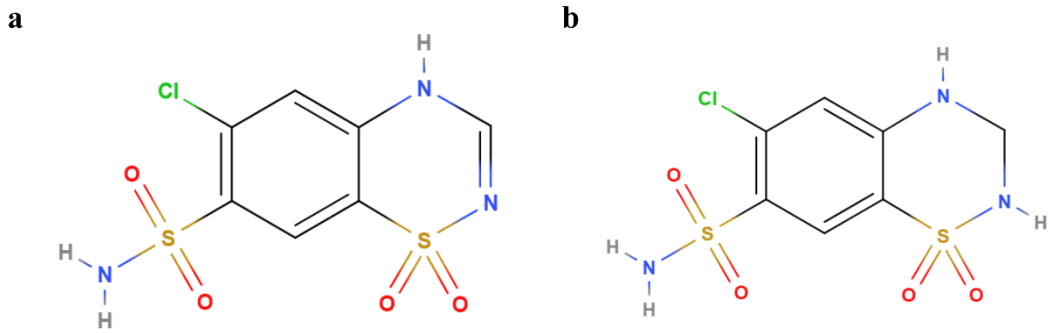

Figure 5.1 – Chemical diagram of **a** chlorothiazide and **b** hydrochlorothiazide

Several projects have previously been carried out to explore the polymorphism of HCT at ambient condition, mainly with the aim of improving the low solubility of this compound. The first polymorphic form of HCT was reported by Dupont et *al* in 1972.[19] After almost one decade, Bong et *al*[22] described four polymorphic forms. However, the following studies were not able to replicate the crystallisation conditions to obtain these polymorphs.[21] Florence et *al.*[20] reported HCT form II using X-ray powder diffraction from an unsual crystallisation technique of adding an acetone solution to an aqueous solution containing hydroxypropylmethylcellulose under agitation. This form crystallizes in the space group $P2_1/c$ with one molecule in the asymmetric unit. Later, the HCT polymorphic forms were characterized by powder neutron diffraction[17] and by single crystal X-ray diffraction for form I.[23] Saini et *al*[23] described a new

polymorphic denoted as form IA from antisolvent crystallisation, tert-butanol was added as antisolvent to the saturated solution of HCT (form I) in ethyl methyl ketone. This form presents a very similar molecular conformation observed in HCT form I; the difference of forms is noted in the rotation of the sulfonamide hydrogen.

To explore the potential of finding a new polymorphic form of HCT, a number of research groups have used conformational analysis[24] and crystal structure prediction[17,21] which only led to the discovery of new solvates. However, this same approach was applied successfully to the screening of cocrystals [25–28], which some of them showed a considerable solubility improvement compared with HCT.

Recently, Thomas et *al.*[29] verified the formation of wing shape crystals for HCT when crystallized in methanol by evaporation crystallisation, Figure 5.2. Detailed characterisation revealed the presence of enantiomorphism twinned crystals. The enantiomers result in the flipping of the saturated ring coupled with inversion of amide adjacent to the sulfone group and rotation of the sulfonamide group. Theoretical calculations were performed to evaluate the energy barriers associated with conformational inversion (47 $kJ \cdot mol^{-1}$). The authors surmised that interaction with polar protic solvent would be able to overcome this barrier. Also, it was suggested a presence of centrosymmetric $\pi \cdots \pi$ stacking interaction (-93 $kJ \cdot mol^{-1}$) at the interfacial join of the enantiomorphic wings could have an essential role in the nucleation.

In this work, we attempt to utilize HCT to explore crystal nucleation by performing high- pressure experiments in the diamond anvil cell. It was possible to access a new polymorphic form of HCT in an irreversible phase transition which precluded us from using this system to study the nucleation process *in-situ*. However, the recoverable nature of the high-pressure phase is interesting by itself. This chapter explores how the

high-pressure form is scaled up using the large volume press allowing its characterisation by X-ray powder diffraction at ambient pressure.

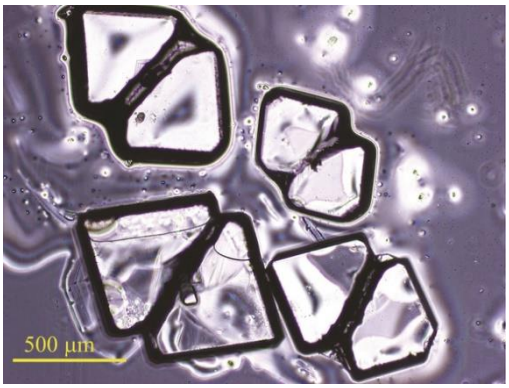

Figure 5.2 - Two-wing habit observed in the HCT crystals (image from the Thomas et *al.* article[29]).

5.3 Experimental procedure

5.3.1 Materials

The compound investigated in this study hydrochlorothiazide (HCT), 6-Chloro-3,4-dihydro-2H-1,2,4-benzothiadiazine-7-sulfonamide 1,1-dioxide, was purchased from Sigma Aldrich. For high-pressure experiments, petroleum ether (40:60) was obtained from Alfa Aesar and used as a pressure transmission medium.

5.3.2 Diamond Anvil Cell

High pressure was generated using the Merrill–Bassett diamond anvil cell equipped with 600 µm culet type seats. A tungsten foil was indented to a thickness of 100 µm and a hole of 250 µm was drilled in the centre of indented gasket using an Almax Easylab Microdriller. To maintain hydrostatic conditions during the application of pressure petroleum ether (40:60) as used as a pressure transmission medium. Ruby chips were loaded into the DAC as a pressure marker. A single crystal was loaded

(140μm x 125 μm x 90 μm) in the cell and during the closing of the cell the crystal broke.

5.3.3 Large Volume Press (LVP)

High-pressure conditions were generated by the use of a large volume press assembly. Prior to loading in the pressure cell, the sample was ground using agate mortar and pestle. Sample and pressure transmitting medium (PTM) were confined in a polytetrafluoroethylene (PTFE) tube (ID = 8.0 mm, OD = 10.0 mm) sealed using PTFE end caps and PTFE sealing tape.[8] Petroleum ether (40:60) was used as PTM and washer liquid during filtration. The sample was pressurized in small increments up to a range of 0.60 – 0.80 GPa. At these pressures, the samples were held for a period of 30 min to 24h.

5.3.4 Raman Spectroscopy

Raman spectra were collected by Horiba Jobin Yvon Xplora micro Raman system with an Olympus Microscope coupled with a LWD 50 × objective lens and CCD detector. The spectra were acquired using a 532 nm laser source, 1200 lines/mm grating and the sum of 2 accumulations to avoid transitory events such as electrical spikes. The selection of slit, hole and filter parameters was chosen to maximize the signal from the sample.

5.3.5 X-ray Powder Diffraction

X-ray powder diffraction (XRPD) data were performed on Bruker D8 Advance I and II diffractometers. The stage of both diffractometers was configured in Debye-Scherrer transmission geometry; the X-ray emission was supplied by a Cu source (λ =

1.5406 Å) used in conjunction with a $K\alpha_1$ Johansson monochromator and 1 mm anti-divergence slit. A Vantec 1D detector was used together with 2.5° Soller slits in the Advance II instrument and a Lynxeye detector was used in the Advance I instrument. The Advance II instrument was design to use a multiwell plate (24 sample places) and a 7.5 μm layer of Kapton film was added to support the samples, in the case of Advance I instrument a 0.7 mm borosilicate capillary was used as support the sample.

The high-pressure X-ray powder diffraction data were collected on Beamline I15 at the Diamond Light Source, using a monochromatic X-ray beam with an incident wavelength of 0.41466 Å. A single crystal of HCT was loaded into a DAC and 0.9 GPa applied to the sample. The phase transition was visually observed as the crystal broke into a polycrystalline sample. 2D diffraction images were recorded at room temperature using a MAR345 image plate detector. Dioptas software[30] was used to integrate the 2D diffraction patterns as a function of 2θ to give one-dimensional diffraction profiles.

All data were collected at room temperature. Simple Pawley fitting and Rietveld refinement of the XRPD data was performed using Topas (Academic, V5).[31]

5.3.6 Differential Scanning calorimetry

Differential scanning calorimetry (DSC) data were performed using a Netzsch DSC 214 Polyma. The equipment was calibrated for both temperature and sensitivity over the temperature range -93 °C to 605 °C, at a heating rate of 20 °C min^{-1} using thermal standards (indium, tin, bismuth and zinc) supplied by Netzsch. The aluminium pans were pre-weighed, loaded with the sample and sealed with a pierced lid. The furnace was purged with helium (60 mL min^{-1}). The samples were analysed following

a temperature program from 25 to 300°C at heating and cooling rate range of 5 and 20 $K \cdot min^{-1}$.

5.4 Results

Despite the structure of HCT form I being described in several studies elsewhere we have revisited it to help provide an idea for the formation of a new high-pressure structure.

HCT crystallizes in the space group $P2_1$ with one molecule in the asymmetric unit. The unit cell parameters are a = 7.419(6) Å, b = 8.521(3) Å, c = 10.003(2) Å, β = 11.720° and a V = 587.5 $Å^3$ at an undefined temperature but an estimate of between 283-303 K is reasonable for ambient temperatures.[19] The chains of HCT molecules are formed using the primary and secondary amide groups (N-H···O = 2.928 Å & 2.884 Å (green)) where the molecules are related by the 2_1-screw operation, Figure 5.3a. The mean plane of the aromatic rings in the chain are not parallel but at an angle of 38.55º when viewed down the *c*-direction. These chains are linked to neighbouring chains along the *c*-direction (light blue) via the second hydrogen atoms of the primary amide, Figure 5.3b. The structure is complete through the final amine on the thiazide ring which hydrogen bonds to the sulfonyl oxygen of molecules along the *a*-direction. Again, these chains are related by a 2_1-screw operation.

Before the study of HCT under high-pressure conditions, we studied the compound under ambient conditions using Raman spectroscopy eliminating any effect of loading procedure, Figure 5.4. The Raman spectrum shows two intense peaks at low frequencies in the phonon region that are associated with specific packing of HCT. Another important area in the Raman spectrum, for organic compounds, is associated

with the functional groups involved in intermolecular interactions such as hydrogen-bonds. It was possible to identify, as reported in previous studies,[24,32] the SO_2 stretching near to 1168 cm^{-1} and the NH stretching modes near to 3170, 3265 and 3365 cm^{-1}. These modes are a consequence of three types of hydrogen-bonding interactions with sulphonic group, which the donors are primary sulphonamide, secondary sulfonamide and secondary amide.

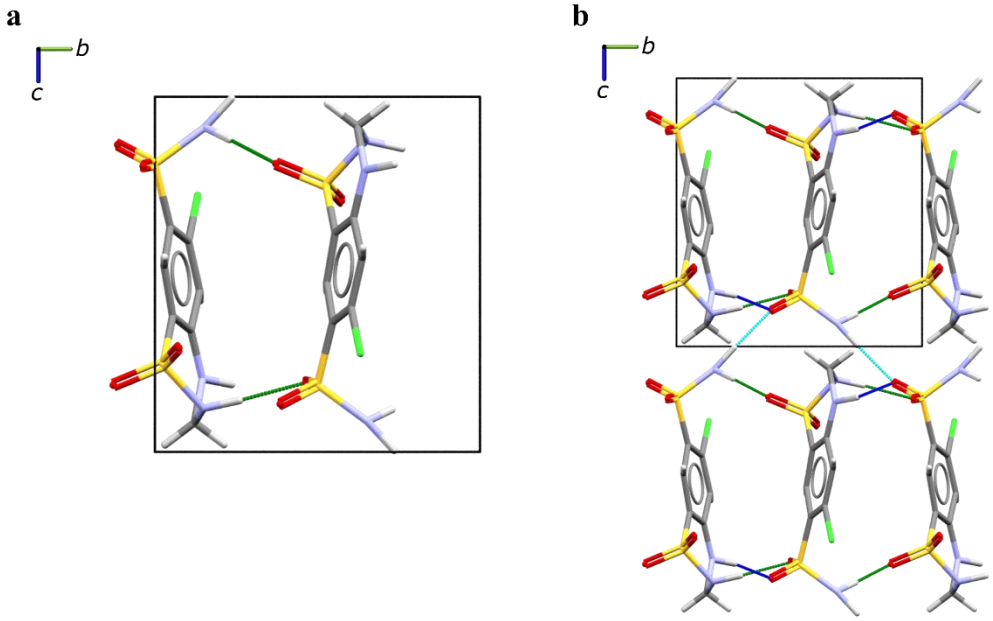

Figure 5.3 – **a** Dimer formed by primary and secondary amide and sulfonamide groups and **b** Crystal packing of HCT via N-H···O bonding. Chains formed by primary sulfonamide groups (link by light blue dotted lines) and through secondary sulfonamide and amide groups (link by dark blue dotted lines) along in the *b*-axis.

The behaviour of HCT under hydrostatic conditions was studied initially using Merrill–Bassett diamond anvil cell (DAC) up to 0.82 GPa and back to atmospheric pressure, Figure 5.5. The cell design allows the collection of Raman spectra and microscope images *in-situ*. During the process of loading the DAC, the crystal could had been fractured when the cell was being closed (fissure on the middle of the crystal

visible in Figure 5.5a at 0.49 GPa) due to operator mishandle or by the effect of pressure into a cleavage plane. This cleavage plane could be related to the interface between twin crystals correspondent to different enantiomer.

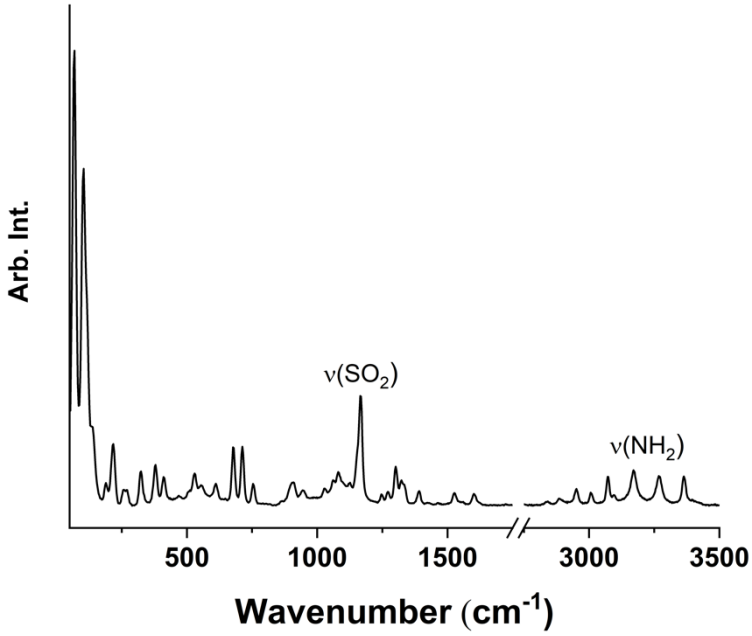

Figure 5.4 – Raman spectrum of HCT on a glass slide under atmospheric conditions.

The HCT form I is stable until 0.49 GPa but increasing pressure to 0.55 GPa, a reconstructive phase transition is observed with changes to the Raman spectrum (highlighted by the shift of the peak at 3163 cm^{-1} to higher wavenumbers) and crystal morphology. During the increase of the load applied to sample, a drop of sample pressure was measured, from 0.82 to 0.77GPa, a possible indication of the increase in density of the new high-pressure polymorph. This new phase is stable until the maximum of pressure applied in the compression study, 0.82 GPa (Figure 5.5a). The Raman spectra indicate a general shift to higher frequencies with increasing pressure which is observed on all high pressure studies. However, the peaks related to the N-H stretching modes present a more pronounced shift effect after the phase transition. At

0.82 GPa, the peak at 3167 cm^{-1} shifts *approx.* 76 cm^{-1} to form a shoulder on the peak at 3272 cm^{-1}. This significant jump in wavenumber is also observed, but to a lesser degree, for the peak at 3265 (shift of *approx.* 20 cm^{-1}) and 3365 cm^{-1} (shift *approx.* 30 cm^{-1}). The alteration of N-H stretching modes will be a consequence of the modification of intermolecular interactions involving NH groups in the crystal structure, where the hydrogen-bonding interactions become weaker or are broken thereby inducing a shift to higher wavenumbers. This will occur with organization into a different packing geometry. Other pressure studies have shown that the efficiency in the molecular packing is more important than hydrogen bonding hence hydrogen bonds can become longer to accommodate the increase molecular packing.[33–36] In fact, that is what we observe with form II of HCT where the hydrogen bonds lengthen from 2.88-2.90 Å in form I to 2.91-3.21 Å in form II and with an increase in the density from 1.706 to 1.829 $mg \cdot m^{-3}$.[17] The molecules in form II engage in a more parallel contact.

The investigation of nucleation at high pressure requires a reversible phase transition for the application of probability distribution method by ter Horst.[37] Another important experimental factor was that the phase transition should be at low pressure so that the changes in pressure were more easily manipulated. However, the irreversible nature of the observed transition in a short time scale made this impossible to investigate the nucleation rate. Instead our focus turned to the behaviour of HCT at high pressure and on decompression as the recovery of high-pressure phases is intriguing from a polymorph screening point of view.

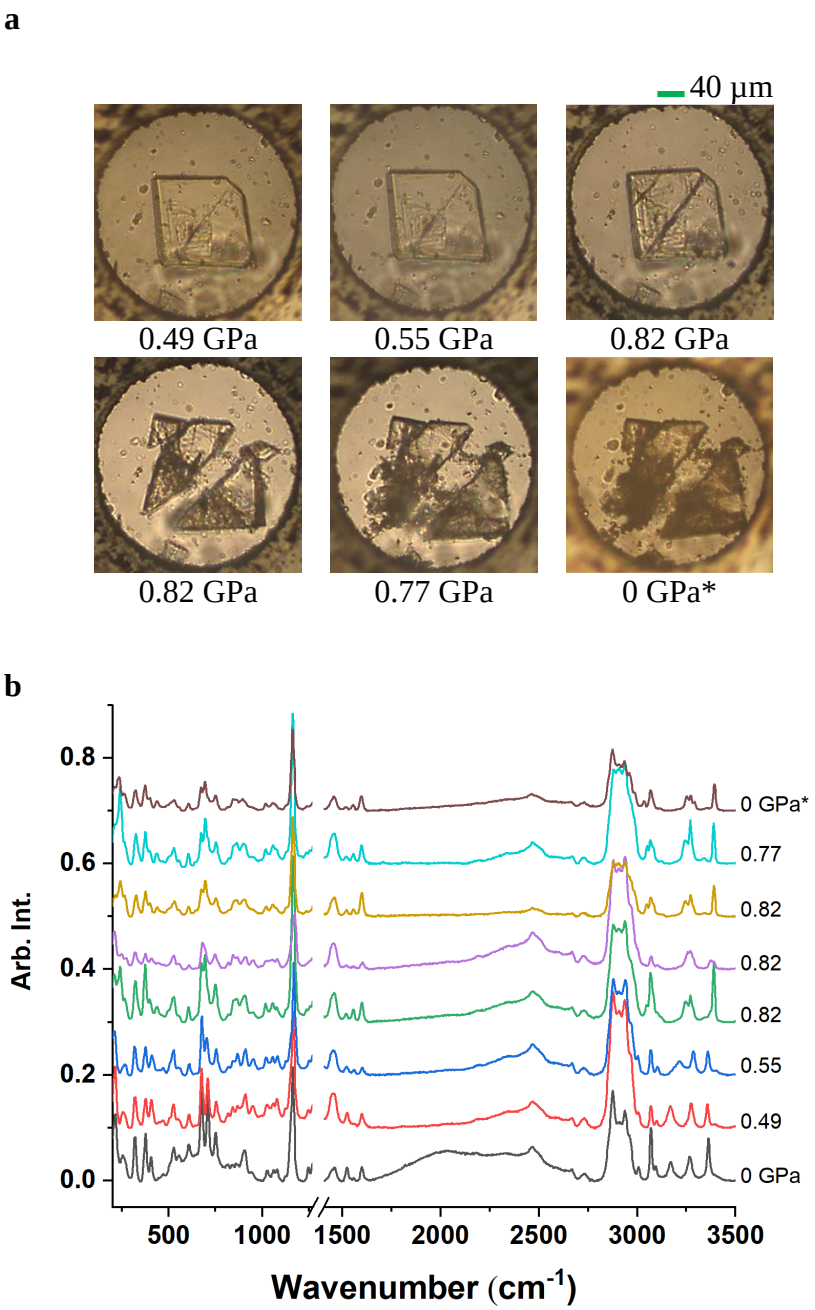

Figure 5.5 – Compression and decompression investigation of HCT from 0 to 0.82 GPa. **a** microscope images recorded before the phase transition at 0.49 GPa, followed by the visualization of phase transition from 0.55 GPa to 0.82 GPa and consequent decompression to 0.77 GPa due to the reorganization of the structure. The picture of crystal was also recorded after decompression (0 GPa*). **b** Raman Spectra acquired immediately after the capture of the microscopic image. At 0.82 GPa, the process of transition was identified by microscopy and several Raman spectra and images are recorded without changing the pressure.

5.4.1 Structural analysis of the high-pressure form of hydrochlorothiazide

The discovery of a new polymorphic form of HCT, high-pressure form (HP form), that is stable after decompression drove this study in another direction, the structural characterisation of this new polymorphic form at ambient pressure. To achieve this goal, several experiments were performed in the large volume press, Table 5.1. The use of the press allows the production of higher quantities of compounds (100's milligrams) so that there is enough material to elucidate the structure and other analysis using ambient pressure techniques; this was enabled by the longevity of the HP form under ambient conditions. All the diffraction patterns (figures in the Appendix B, Figure B.1, Figure B.2 and Figure B.3), showed a mixed phase of HCT form I and an unknown phase (Figure 5.6a). These data were analysed in more detail using TOPAS Academic[31]. The procedures will be detailed here for completeness however the indexing of the powder was performed by Kenneth Shankland. Due to the complexity of the data, it was necessary to combine different methodologies to determine the 'pure' powder diffraction pattern for the high-pressure polymorph. Firstly, the diffraction data were fitted through a dual Rietveld refinement of HCT form I and II but only allowing the scale factor to refine to elucidate which of the polymorphs of HCT were present. This demonstrated that Form II was not present. To determine the unknown structure, the peaks of HCT form I were identified from the experimental diffraction pattern and the remaining peaks were assigned to the new polymorphic form (HP form). The peaks associated with the new phase were used to index the new phase and there was one unit cell that fit the data very well (a = 7.503 Å, b = 7.9154

Å, c = 22.806 Å, α= 99.146º, β = 124.920º, γ = 94.889º which would indicate a Z' = 2 in $P\bar{1}$ or Z' = 4 in *P*1 structure). The new unit cell information was added as an input to a new dual Rietveld (form I)/Pawley (HP form) refinement (Figure 5.6b). This dual model input file was applied to data from all powders produced using the large volume press.

Table 5.1 – Experimental conditions applied to powder samples of HCT obtained in the LVP and DAC.

Sample	Method	High-pressure		XRPD	
		Pressure GPa	Time held h	Acquisition	Method
HCT-A	LVP	0.60	16	After downloaded	On plate
HCT-B				After downloaded	On plate
HCT- B1				12 days later	On capillary
HCT-C		0.78	24	After downloaded	On plate
HCT-C1				1 year later	On plate
HCT-C2				2 years later	On plate
HCT-D		0.80	0.5	After downloaded	On plate
HCT-E		0.80	16	After downloaded	On plate
HCT-F					On plate
HCT-G		0.75-0.80			On plate
HCT-H					On plate
HCT-I	DAC	0.9		*In-situ*	On the DAC cell

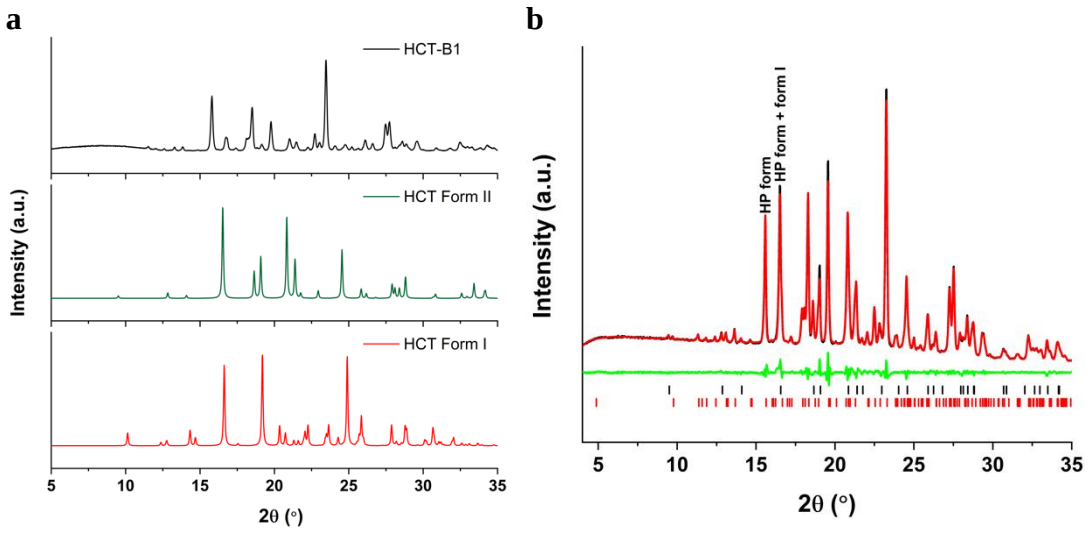

Figure 5.6 – Characterisation of HCT through XRPD. **a** Comparison of experimental data of HCT-B1 sample with simulated data of form I (CSD: HCSBTZ)[19] and HP form of HCT (CSD: HCSBTZ01)[20] **b** Dual Rietveld/Pawley refinement applied to HCT-B1; The model (red line) fits well the experimental pattern (black) which is evident by the difference between these patterns (green line). Black tick marks represent the positions of the HCT form I reflections and red tick marks show the positions of the new HCT HP form reflections.

5.4.2 High-pressure polymorphic form

Through the dual Rietveld/Pawley refinement method it was possible to refine form I and isolate the peaks of the HP form in all samples of HCT obtained in LVP experiments. Using the isolated peaks, the high-pressure form could be indexed and a dual Rietveld/Pawley refinement could be performed. Due to the implementation of Pawley refinement of the HP form, the quantification of each polymorphic form is not possible. However, the conversion between form I and HP form was previously observed by our research group through X-ray powder diffraction experiments on samples at 0.9 GPa on beamline I15 in Diamond Light Source, Figure 5.7. The powder diffraction pattern collected in this experiment fits very well the HP form model that was obtained from the large volume press recovery and indicates that this sample was pure HP form, Figure 5.7b.

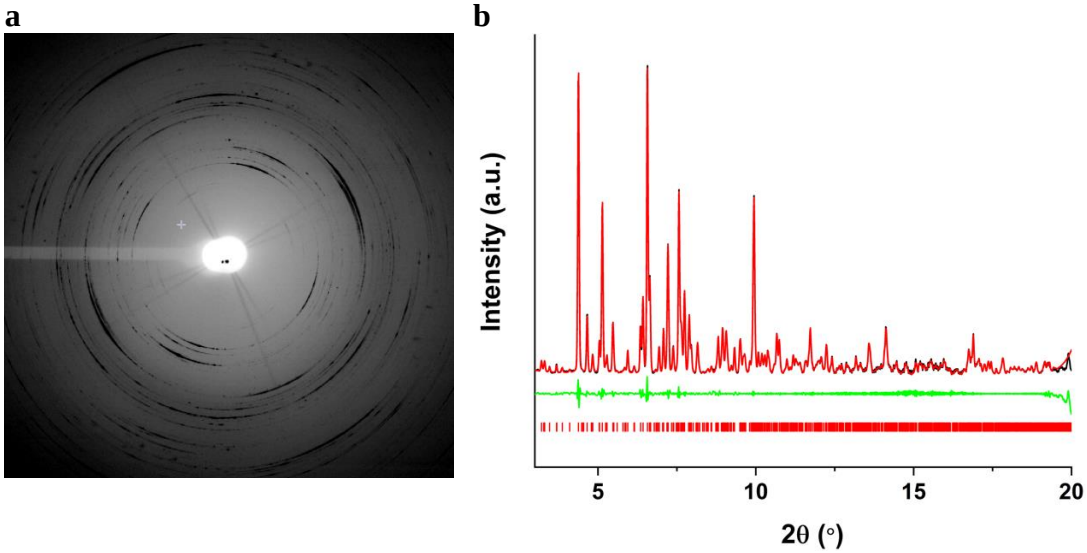

Figure 5.7- Powder diffraction pattern of pure HP form of HCT, HCT-I. **a** Image of the diffracted beams **b** dual Rietveld/Pawley fit applied to HCT-I data; The model of HP form (red line) fits well the experimental pattern (black) which is evident by the difference between these patterns (green). Black tick marks represent the positions of the HCT form I reflections and red tick marks show the positions of the new HCT form reflections.

To enable an approximation of the purity of the LVP samples we used peak areas from the pure HP form at pressure to provide a baseline for assessment. Even though, the XRPD data collected in the plate holder can be affected by preferential orientation, a good approximation between peak area and relative polymorphic form amounts can be achieved due to the reconstructive nature of the transition in this sample which facilitates the production of a suitably random powder. The comparison of pure high-pressure diffraction data with the data collected for LVP samples allow us to determine the relative amounts of HP form in the LVP samples by the ratio of peak area between HP form and form I using peaks specific to each of these phases.

The determination of the ratio of the polymorphic forms relies on two assumptions: (i) the powder sample obtained by a reconstructive phase transition is ideal for XRPD measurements i.e. there is little preferred orientation effects; and (ii) the ratio of the

two peaks chosen in the pure high-pressure form sample is consistent with the structure and that the structure does not change significantly on decompression. The assumption (i) is based in the nature of a reconstructive phase transition; in this process the transformation from a single-crystal sample to polycrystalline sample provokes different crystal orientations which minimizes the preferential orientation effects. The raw powder diffraction image of HCT at 0.90 GPa indicates that the powder is close to ideal denoting a low implication of preferential orientation in this sample albeit there are slight maxima around the rings. The assumption (ii) is required due to the absence of an exclusive peak attributable to form I. In the mixed phase there was a peak that could be attributed solely to the HP form that could be integrated however there were no peaks that could be attributed to form I. Therefore, a peak was chosen that contained contributions from one reflection per structure which gives us the best opportunity to 'quantify' the phases and minimise possible effects of structural changes. The selection of one peak related to both forms is unavoidable, Figure 5.6b.

The peak area ratio was carried out using well defined peak, (1-1-1) and (1-10) reflections representative of HP form and a mixed composition of HP form and form I, respectively, Figure 5.6b. In the powder diffraction pattern, these reflections are observed at 2θ near to 16 and 17° in experiments performed with CuKα_1 source instruments (HCT A to HCT H samples, e.g. Figure 5.6) and 4.4 and 4.7° in experiments carried out at Diamond Light Source (HCT-I, Figure 5.7).

The high-pressure data can be fitted well using only the indexing achieved for the HP phase indicating that the *in-situ* data collected at 0.9 GPa is that of the pure HP phase. Any variation of ratio in the recovered samples will be due to the quantity of form I present in the sample. We normalised the ratios so that the ratio determined

from the high-pressure data was set to 1. In this study, we analysed the dependence of pressure and hold time to achieve the transition to the high-pressure form. The dual Rietveld/Pawley refinement was applied to all the samples successfully, Table 5.2. The indexing matched the form I and HP form of HCT, previously described. The results obtained in this work showed a partial polymorphic conversion at the range of 0.50-0.80 GPa for samples held during different periods. The higher value of conversion was found in the sample HCT-C where pressure was applied until 0.78 GPa and held for 24h. This sample was also analyzed after one and two years. The results showed a progressive conversion of HP form to form I over this time period. The relationship between form conversion, pressure and time held is not conclusive. Other factors that may have an important impact in the polymorphic conversion, such as rate of compression and decompression (difficult to be controlled in the LVP), time before and during X-ray diffraction collection however these parameters were not logged. Given the longevity of the HP form the time around X-ray diffraction experiment is not likely a source of error. Higher pressure values also should had been considered, but due to pressure limit in the LVP apparatus (< 0.80 GPa) they were not explored.

Table 5.2 – Results obtained in the Pawley fit analysis of HCT, peak area ratio and unit cell parameters.

Sample	Polymorphic form	Peak area ratio HP/form I*	Unit cell Parameters a Å	b Å	c Å	α °	β °	γ °	V Å^3
HCT-A	Mixture Form I + HP form	0.193	7.503(2)	7.9154(14)	22.806(5)	99.146(10)	124.920(8)	94.889(6)	1070.2(5)
HCT-B		0.488	7.5047(15)	7.9161(10)	22.821(4)	99.170(6)	124.905(5)	94.853(4)	1071.5(3)
HCT-B1		0.124	7.5000(8)	7.9152(6)	22.810(2)	99.158(6)	124.911(5)	94.887(3)	1069.96(19)
HCT-C		0.902	7.491(2)	7.9037(16)	22.773(6)	99.156(11)	124.896(10)	94.856(7)	1065.8(5)
HCT-C1		0.544	7.5077(11)	7.9215(7)	22.834(3)	99.161(5)	124.896(5)	94.869(3)	1073.3(2)
HCT-C2		0.238	7.5061(7)	7.9180(5)	22.8267(17)	99.140(4)	124.895(4)	94.889(2)	1072.32(16)
HCT-D		0.107	7.4755(17)	7.9010(12)	22.730(5)	99.304(13)	124.770(10)	94.919(8)	1061.8(4)
HCT-E		0.276	7.4754(17)	7.9010(12)	22.730(5)	99.304(13)	124.770(10)	94.919(8)	1061.758
HCT-F		0.041	7.4832(17)	7.9127(10)	22.771(6)	99.316(15)	124.783(13)	94.937(8)	1066.0(4)
HCT-G		0.064	7.488(2)	7.9170(15)	22.772(7)	99.330(14)	124.776(11)	94.916(8)	1067.4(5)
HCT-H		0.028	7.4946(16)	7.92056(9)	22.785(6)	99.227(16)	124.793(15)	94.941(9)	1069.7(4)
HCT-I	HP form	1	7.398(10)	7.700(6)	22.41(3)	99.422(6)	124.792(7)	94.857(3)	1009(2)

*Peak area ratio between peak representative of HP form (peak area calculated using the peak at 16° (HCT-A to HCT-H) and 4.3° (HCT-I) and the peak representative of mixed forms (peak area calculated using the peak at 17° (HCT-A to HCT-H) and 4.7° (HCT-I)).

5.4.3 Comparison between form I and HP form of HCT

In the absence of a crystal structure for the HP form of HCT, the recovery of HP form through the use of LVP instrument allowed us to evaluate the stability of the compound with respect to temperature and in solution.

The thermal behaviour of mixed phases of form I and HP form was studied using the HCT-C and HCT-F samples due to the conditions in which they were created i.e. highest pressure and longest holding time (Figure 5.8 and Table 5.3). A temperature cycle was performed in the range of 20 and 290°C. The cycle was carried out at different rates, 5 °C·min^{-1} for HCT-C and 20 °C·min^{-1} for HCT-F. The results showed an endothermic event at *ca* 265°C corresponding to the melting point of the mixture very similar to the melting temperature of pure form I of HCT[23] (T_{onset} = 266.49 °C; ΔH = 113.4 J·g^{-1}). During the heating process the samples reached decomposition hence crystallisation was not observed during the cooling process. The values of onset temperature and enthalpy of melting show that the difference of stability of form I and HP form of HCT could be defined mainly by the entropy term in the Gibbs free energy equation, expected for a reconstructive phase transition. As stated earlier, based on the indexing of the new patterns, the new crystal structure will have either *Z*'=2 or 4. In each case there is an increase in the number of molecules in the asymmetric unit over form I hence an increase in the entropy of the system through increase in the number of variables.

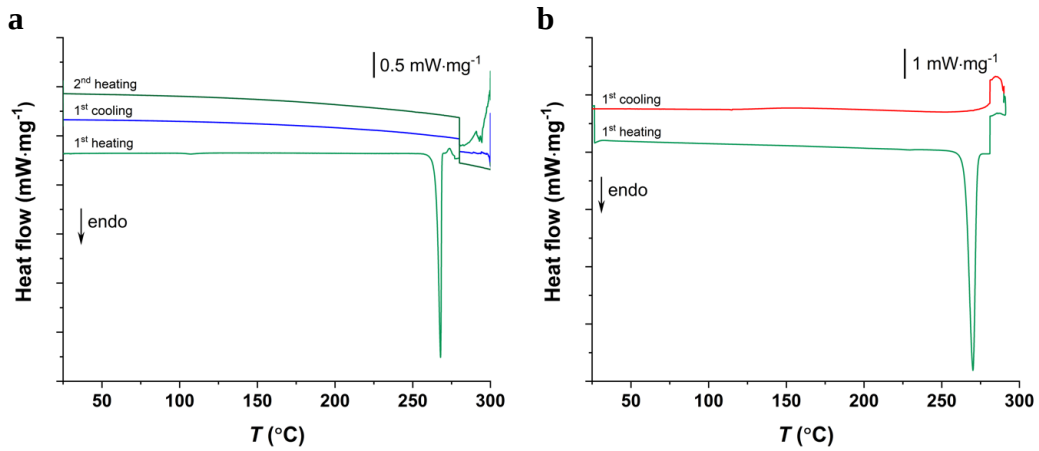

Figure 5.8 – Thermal analysis of the HCT-C (6 mg) and HCT-F (8.12 mg), mixed form of form I and HP form of HCT. The temperature cycles were performed to HCT-C and HCT-F sample at 5.0 and 20.0 $K \cdot min^{-1}$, respectively.

Table 5.3 – Values of onset temperature (T_{onset}) and enthalpy (ΔH) obtained in the thermal study.

Sample	T_{onset} °C	ΔH $J \cdot g^{-1}$
HCT Form I*	266.5	-113.4
HCT-C	265.1	-123.1
HCT-F	265.0	-110.9

* Values from the work reported by Saini *et al*[23]

Due to the small differences in the values between the two phases we looked at the stability of HCT in solution through a slurry method in water and ethanol. A small amount of HCT was added into the vial with the solvent. A sample was collected after a few minutes and immediately analyzed through XRPD. The results showed a quick conversion of the mixed material to form I. The presence of a small amount of form I in the mixture could have acted as a seed and promote the conversion of HP form to form I through solution-mediated transformation driven by solubility differences.

5.4.4 Approaches to solving the structure of HP form

In this study, we were able to index the HP form by applying the dual Rietveld/Pawley refinement to powder diffraction data collected at the University of

Strathclyde ($CuK\alpha_1$ source ($\lambda = 1.5406$ Å)) and extracting the 2-theta values associated with the high pressure form. These values were used in TOPAS Academic[31] to find a suitable cell (Table 5.4). There were two solutions that showed a high Goodness of Fit (GoF) with a volume that is consistent with 2 or 4 molecules of HCT in the asymmetric unit using the 18 $Å^3$ rule ($C_7H_8ClN_3O_4S_2$; Molecular volume of 306 $Å^3$ hence $Z = 3.5$). Whilst solution 2 has a more reasonable number of molecules ($Z = 2$), the fit to the data was poor (Table 5.4). The 18 $Å^3$ rule is a guide based on observations of ambient pressure crystal structures hence it is not surprising that this does not necessarily fit with crystal structure formed at 0.8 GPa that will have increased density over ambient pressure crystal structures.

Table 5.4 - Fit of the HCT7 data with the unit cell parameters of solution 2

	Space group	Volume $Å^3$	GoF	zero error	a Å	b Å	c Å	α °	β °	γ °
0)	$P\bar{1}$	1072.918	89.57	-0.0470	7.5090	7.9219	22.8275	99.093	124.94	94.895
1)	$P\bar{1}$	1072.774	84.92	-0.0475	7.5093	7.9208	18.8118	105.047	95.929	85.101
2)	$P\bar{1}$	616.23	73.88	-0.0589	5.7206	6.0098	18.1461	93.746	88.149	82.205
3)	$P\bar{1}$	1071.705	56.57	-0.0534	7.5057	7.9194	18.4112	99.474	86.066	85.106
4)	$P\bar{1}$	897.263	48.51	-0.0642	5.6814	8.7475	23.5287	111.079	123.33	86.574
5)	$P\bar{1}$	545.568	46.98	-0.0116	8.3504	10.5253	7.1600	108.961	84.142	113.486
6)	$P\bar{1}$	1080.486	44.68	-0.0225	7.5296	7.9294	18.8681	105.043	95.707	85.132
7)	$P\bar{1}$	1080.89	43.29	-0.0203	7.5298	7.9306	18.4746	99.428	86.257	85.145
8)	$P\bar{1}$	1082.194	42.39	-0.0140	7.5322	7.9318	18.4919	99.462	86.241	85.101
9)	$P\bar{1}$	522.261	40.72	-0.0636	4.9965	9.5078	11.6706	76.917	97.973	103.838

The second stage of structural solution from powders was simulated annealing using procedures in DASH[38] and TOPAS Academic[31]. This process starts with the known unit cell parameters and an idea of the contents of the unit cell. The contents can be estimated based on the likely symmetry of the crystal structure and volume of the unit cell. The unit cell parameters of the HP form of HCT limits the space group

choice to either $P\bar{1}$ or $P1$ with $Z' = 2$ or 4, respectively. The least computationally demanding is the $P\bar{1}$ structure as the positions of only two molecules are required. As an example of simulated annealing, two molecules of HCT are added to the unit cell in a known geometry, i.e. the conformation of the molecules in form I; the other two molecules are generated through the space group. From this point the simulated annealing algorithm starts with random values of parameters, such as molecular position, orientation and conformation. The comparison between calculated and observed intensities is assessed by the determination of χ^2 (goodness-of –fit statistic). After this comparison, a random parameter is changed and the χ^2 is calculated again. The algorithm keeps the new value if the χ^2 values has gone down. If the χ^2 value has gone up there is the potential to accept the change depending the temperature of the system. Initially the 'temperature' of the system is high hence this is likely so that more of the potential energy surface can be surveyed and that the search does not get trapped in local minima. During the process the temperature is lowered hence there is an increased likelihood of finding the global minimum. The algorithm continues this procedure until the system converges to a minimum in χ^2 space, or when a maximum number of moves is achieved. In each of these cases the solution was not apparent perhaps due to the purity of the samples hence better data may help us to elucidate the structure.[*]The LVP experimental parameters of sample HCT-C will be used to isolate the HP form for analysis on beamline I11 at Diamond Light Source.

[*] To improve the resolution of the data, we have successfully applied with success to synchrotron X-ray powder diffraction beamline (I11) at the Diamond Light Source but as yet the time has not been scheduled.

5.5 Conclusion

The characterisation of single-crystals of HCT in the diamond anvil cell using Raman spectroscopy coupled with microscopy allowed the detection of a reconstructive phase transition at *ca* 0.55 GPa to a new high-pressure form. The new polymorphic phase is sufficiently stable after decompression: Under ambient conditions the HP form converts slowly (year timescale) to form I when left as a powder although it converts readily in solution environment. The long timescales for conversion preclude this compound to be the used in nucleation studies at high pressure. However, the high stability of the HP form at atmospheric condition brings new opportunities to scale up a high-pressure form using crystallisation methods at ambient conditions. A combined dual Rietveld/Pawley refinement, permitted the identification and indexing of a HP form of HCT from the mixed phase samples produced in the large volume press. The structural data show a transformation from the space group $P2_1$ to a likely space group, $P\bar{1}$. The Raman data indicate a weakening of the hydrogen-bond interaction through an increase in the wavenumber of the NH stretching modes, which could suggest the molecular packing interactions are more important in this new form.

5.6 Acknowledgement

We would like to thank Dr Martin R. Ward for useful discussions and Prof. Kenneth Shankland from University of Reading for the collaboration in the analysis of the powder patterns.

We would like to thank the EPSRC (Grant Ref: EP/N015401/1) and the Doctoral Training Centre in Continuous Manufacturing and Crystallisation (Grant Ref:

EP/K503289/1) and the Centre for Innovative Manufacturing in Continuous Manufacturing and Crystallisation (Grant Ref: EP/I033459/1) for funding this work. We would like to acknowledge that this work was carried out in the CMAC National Facility supported by UKRPIF (UK Research Partnership Fund) award from the Higher Education Funding Council for England (HEFCE) (Grant Ref: HH13054).

5.7 References

(1) Wood, P. A.; Francis, D.; Marshall, W. G.; Moggach, S. A.; Parsons, S.; Pidcock, E.; Rohl, A. L. A Study of the High-Pressure Polymorphs of L-Serine Using Ab Initio Structures and PIXEL Calculations. *CrystEngComm* **2008**, *10* (9), 1154. https://doi.org/10.1039/b801571f.

(2) Fedorov, A. Y.; Rychkov, D. A.; Losev, E. A.; Zakharov, B. A.; Stare, J.; Boldyreva, E. V. Effect of Pressure on Two Polymorphs of Tolazamide: Why No Interconversion? *CrystEngComm* **2017**, *19* (16), 2243–2252. https://doi.org/10.1039/C6CE02527G.

(3) Hutchison, I. B.; Bull, C. L.; Marshall, W. G.; Urquhart, A. J.; Oswald, I. D. H. Pressure-Induced Polymorphism of Caprolactam: A Neutron Diffraction Study. *Molecules* **2019**, *24* (11). https://doi.org/10.3390/molecules24112174.

(4) Zakharov, B. A.; Kolesov, B. A.; Boldyreva, E. V. Effect of Pressure on Crystalline L- and Dl-Serine: Revisited by a Combined Single-Crystal X-Ray Diffraction at a Laboratory Source and Polarized Raman Spectroscopy Study. *Acta Crystallogr. Sect. B Struct. Sci.* **2012**, *68* (3), 275–286. https://doi.org/10.1107/S0108768112015960.

(5) Toscani, S.; Céolin, R.; Ter Minassian, L.; Barrio, M.; Veglio, N.; Tamarit, J.

L.; Louër, D.; Rietveld, I. B. Stability Hierarchy between Piracetam Forms I, II, and III from Experimental Pressure-Temperature Diagrams and Topological Inferences. *Int. J. Pharm.* **2016**, *497* (1–2), 96–105. https://doi.org/10.1016/j.ijpharm.2015.11.036.

(6) Boldyreva, E. V.; Dmitriev, V.; Hancock, B. C. Effect of Pressure up to 5.5 GPa on Dry Powder Samples of Chlorpropamide Form-A. *Int. J. Pharm.* **2006**, *327* (1–2), 51–57. https://doi.org/10.1016/j.ijpharm.2006.07.019.

(7) Oswald, I. D. H.; Lennie, A. R.; Pulham, C. R.; Shankland, K. High-Pressure Structural Studies of the Pharmaceutical, Chlorothiazide. *CrystEngComm* **2010**, *12* (9), 2533. https://doi.org/10.1039/c001355b.

(8) Hutchison, I. B.; Delori, A.; Wang, X.; Kamenev, K. V.; Urquhart, A. J.; Oswald, I. D. H. Polymorphism of a Polymer Precursor: Metastable Glycolide Polymorph Recovered via Large Scale High-Pressure Experiments. *CrystEngComm* **2015**, *17* (8), 1778–1782. https://doi.org/10.1039/C5CE00119F.

(9) Hutchison, I. B.; Bull, C. L.; Marshall, W. G.; Parsons, S.; Urquhart, A. J.; Oswald, I. D. H. Compression of Glycolide-h 4 to 6 GPa. *Acta Crystallogr. Sect. B Struct. Sci. Cryst. Eng. Mater.* **2017**, *73* (6), 1151–1157. https://doi.org/10.1107/S2052520617015657.

(10) Ward, M. R.; Younis, S.; Cruz-Cabeza, A. J.; Bull, C. L.; Funnell, N. P.; Oswald, I. D. H. Discovery and Recovery of Delta p -Aminobenzoic Acid. *CrystEngComm* **2019**, *21* (13), 2058–2066. https://doi.org/10.1039/C8CE01882K.

(11) Zakharov, B. A.; Goryainov, S. V.; Boldyreva, E. V. Unusual Seeding Effect in

the Liquid-Assisted High-Pressure Polymorphism of Chlorpropamide. *CrystEngComm* **2016**, *18* (29), 5423–5428. https://doi.org/10.1039/C6CE00711B.

(12) Boldyreva, E. V. Combined X-Ray Diffraction and Raman Spectroscopy Studies of Phase Transitions in Crystalline Amino Acids at Low Temperatures and High Pressures: Selected Examples. *Phase Transitions* **2009**, *82* (4), 303–321. https://doi.org/10.1080/01411590902838656.

(13) Boldyreva, E. V.; Sowa, H.; Ahsbahs, H.; Goryainov, S. V.; Chernyshev, V. V.; Dmitriev, V. P.; Seryotkin, Y. V.; Kolesnik, E. N.; Shakhtshneider, T. P.; Ivashevskaya, S. N.; et al. Pressure-Induced Phase Transitions in Organic Molecular Crystals: A Combination of x-Ray Single-Crystal and Powder Diffraction, Raman and IR-Spectroscopy. *J. Phys. Conf. Ser.* **2008**, *121* (2), 022023. https://doi.org/10.1088/1742-6596/121/2/022023.

(14) Neumann, M. A.; van de Streek, J.; Fabbiani, F. P. A.; Hidber, P.; Grassmann, O. Combined Crystal Structure Prediction and High-Pressure Crystallization in Rational Pharmaceutical Polymorph Screening. *Nat. Commun.* **2015**, *6* (1), 7793. https://doi.org/10.1038/ncomms8793.

(15) Oswald, I. D. H.; Allan, D. R.; Day, G. M.; Motherwell, W. D. S.; Parsons, S. Realizing Predicted Crystal Structures at Extreme Conditions: The Low-Temperature and High-Pressure Crystal Structures of 2-Chlorophenol and 4-Fluorophenol. *Cryst. Growth Des.* **2005**, *5* (3), 1055–1071.

(16) Chen, J.; Sarma, B.; Evans, J. M. B.; Myerson, A. S. Pharmaceutical Crystallization. *Cryst. Growth Des.* **2011**, *11* (4), 887–895. https://doi.org/10.1021/cg101556s.

(17) Leech, C. K.; Fabbiani, F. P. A.; Shankland, K.; David, W. I. F.; Ibberson, R. M. Accurate Molecular Structures of Chlorothiazide and Hydrochlorothiazide by Joint Refinement against Powder Neutron and X-Ray Diffraction Data. *Acta Crystallogr. Sect. B Struct. Sci.* **2008**, *64* (1), 101–107. https://doi.org/10.1107/S010876810705687X.

(18) Johnston, A.; Bardin, J.; Johnston, B. F.; Fernandes, P.; Kennedy, A. R.; Price, S. L.; Florence, A. J. Experimental and Predicted Crystal Energy Landscapes of Chlorothiazide. *Cryst. Growth Des.* **2011**, *11* (2), 405–413. https://doi.org/10.1021/cg1010049.

(19) Dupont, L.; Dideberg, O. Structure Cristalline de l'hydrochlorothiazide, C 7 H 8 ClN 3 O 4 S 2. *Acta Crystallogr. Sect. B Struct. Crystallogr. Cryst. Chem.* **1972**, *28* (8), 2340–2347. https://doi.org/10.1107/S0567740872006090.

(20) Florence, A.; Johnston, A.; Fernandes, P.; Shankland, K.; Stevens, H. N. E.; Osmundsen, S.; Mullen, A. B. Powder Study of Hydrochlorothiazide Form II. *Acta Crystallogr. Sect. E Struct. Reports Online* **2005**, *61* (9). https://doi.org/10.1107/S1600536805023640.

(21) Johnston, A.; Florence, A. J.; Shankland, N.; Kennedy, A. R.; Shankland, K.; Price, S. L. Crystallization and Crystal Energy Landscape of Hydrochlorothiazide. *Cryst. Growth Des.* **2007**, *7* (4), 705–712. https://doi.org/10.1021/cg0606242.

(22) Kim, B. H.; Kim, J. K. Pharmaceutical Studies on the Polymorphism of Hydrochlorothiazide. *Arch. Pharm. Res.* **1984**, *7* (1), 47–52. https://doi.org/10.1007/BF02856921.

(23) Saini, A.; Chadha, R.; Gupta, A.; Singh, P.; Bhandari, S.; Khullar, S.; Mandal,

S.; Jain, D. S. New Conformational Polymorph of Hydrochlorothiazide with Improved Solubility. *Pharm. Dev. Technol.* **2015**, *21* (5), 1–8. https://doi.org/10.3109/10837450.2015.1041040.

(24) Aceves-Hernández, J. M.; Agacino-Valdés, E.; Paz, M.; Hinojosa-Torres, J. Experimental and Theoretical Study of the Conformational Analysis of Hydrochlorothiazide. *J. Mol. Struct.* **2006**, *786* (1), 1–8. https://doi.org/10.1016/j.molstruc.2005.09.019.

(25) Price, S. (Sally) L. Computed Crystal Energy Landscapes for Understanding and Predicting Organic Crystal Structures and Polymorphism. *Acc. Chem. Res.* **2009**, *42* (1), 117–126. https://doi.org/10.1021/ar800147t.

(26) Almarsson, Ö.; Hickey, M. B.; Peterson, M.; Zaworotko, M.; Moulton, B.; Rodriguez-Hornedo, N. Pharmaceutical Co-Crystal Compositions of Drugs Such as Carbamazepine, Celecoxib, Olanzapine, Itraconazole, Topiramate, Modafinil, 5-Fluorouracil, Hydrochlorothiazide, Acetaminophen, Aspirin, Flurbiprofen, Phenytoin and Ibuprofen.

(27) Ranjan, S.; Devarapalli, R.; Kundu, S.; Vangala, V. R.; Ghosh, A.; Reddy, C. M. Three New Hydrochlorothiazide Cocrystals: Structural Analyses and Solubility Studies. *J. Mol. Struct.* **2017**, *1133*, 405–410. https://doi.org/10.1016/j.molstruc.2016.12.019.

(28) Sanphui, P.; Devi, V. K.; Clara, D.; Malviya, N.; Ganguly, S.; Desiraju, G. R. Cocrystals of Hydrochlorothiazide: Solubility and Diffusion/Permeability Enhancements through Drug–Coformer Interactions. *Mol. Pharm.* **2015**, *12* (5), 1615–1622. https://doi.org/10.1021/acs.molpharmaceut.5b00020.

(29) Thomas, S. P.; Grosjean, A.; Flematti, G. R.; Karton, A.; Sobolev, A. N.;

Edwards, A. J.; Piltz, R. O.; Iversen, B. B.; Koutsantonis, G. A.; Spackman, M. A. Investigation of an Unusual Crystal Habit of Hydrochlorothiazide Reveals Large Polar Enantiopure Domains and a Possible Crystal Nucleation Mechanism. *Angew. Chemie Int. Ed.* **2019**, *58* (30), 10255–10259. https://doi.org/10.1002/anie.201905085.

(30) Prescher, C.; Prakapenka, V. B. DIOPTAS : A Program for Reduction of Two-Dimensional X-Ray Diffraction Data and Data Exploration. *High Press. Res.* **2015**, *35* (3), 223–230. https://doi.org/10.1080/08957959.2015.1059835.

(31) Coelho, A. TOPAS – Academic: General Profile and Structure Analysis Software for Powder Diffraction Data. *TOPAS – Academic: General Profile and Structure Analysis Software for Powder Diffraction Data*. Version 5. 2012.

(32) Deppeler, H. P. Hydrochlorothiazide. In *Analytical Profiles of Drug Substances and Excipients*; 1981; Vol. 10, pp 405–441. https://doi.org/10.1016/S0099-5428(08)60646-2.

(33) Allan, D. R.; Clark, S. J.; Brugmans, M. J. P.; Ackland, G. J.; Vos, W. L. Structure of Crystalline Methanol at High Pressure. *Phys. Rev. B* **1998**, *58* (18), R11809–R11812. https://doi.org/10.1103/PhysRevB.58.R11809.

(34) Allan, D. R.; Clark, S. J. Comparison of the High-Pressure and Low-Temperature Structures of Ethanol and Acetic Acid. *Phys. Rev. B* **1999**, *60* (9), 6328–6334. https://doi.org/10.1103/PhysRevB.60.6328.

(35) McGregor, P. A.; Allan, D. R.; Parsons, S.; Pulham, C. R. The Low-Temperature and High-Pressure Crystal Structures of Cyclobutanol (C 4 H 7 OH). *Acta Crystallogr. Sect. B Struct. Sci.* **2005**, *61* (4), 449–454. https://doi.org/10.1107/S0108768105019191.

(36) Allan, D. R.; Clark, S. J.; Dawson, A.; McGregor, P. A.; Parsons, S. Pressure-Induced Polymorphism in Phenol. *Acta Crystallogr. Sect. B* **2002**, *58* (6), 1018–1024. https://doi.org/doi:10.1107/S0108768102018797.

(37) Jiang, S.; ter Horst, J. H. Crystal Nucleation Rates from Probability Distributions of Induction Times. *Cryst. Growth Des.* **2011**, *11* (1), 256–261. https://doi.org/10.1021/cg101213q.

(38) David, W. I. F.; Shankland, K.; van de Streek, J.; Pidcock, E.; Motherwell, W. D. S.; Cole, J. C. DASH : A Program for Crystal Structure Determination from Powder Diffraction Data. *J. Appl. Crystallogr.* **2006**, *39* (6), 910–915. https://doi.org/10.1107/S0021889806042117.

Chapter 6

Conclusions and Future Work

The aim of this thesis is to investigate crystal nucleation at ambient and high-pressure conditions using phase diagrams and structural characterisation. This chapter summarises the main conclusions of this work and suggests possible approaches for further research based on this topic.

Nucleation is a crucial stage in the crystallisation that can determine crystal size distribution, crystal shape, purity and polymorphic form. For these reasons, the expansion of crystal nucleation knowledge is essential to optimize and control the product quality in crystallisation industry.

In chapter 3, we explored a strategy to improve the chiral resolution of racemic compound RS-2-(2-oxo-pyrrolidin-1-yl)-butyramide, known as Etiracetam, by applying cocrystallisation. The formation of a pure enantiomer cocrystals (Levetiracetam cocrystals) and racemic cocrystals presented a possibility to change the chiral phase diagram, by expanding the enantiopure region and reducing the racemic region. This information can be accessed through the determination of saturation temperatures and eutectic composition points. The determination of solubility curves of target compounds, coformers and mixtures was performed in Crystal 16. This equipment allowed us to design the phase diagram using less amount of sample and being less labour-intensive than traditional techniques (e.g. gravimetric analysis). To decrease the number of variable of the quaternary phase diagram, we followed the approach of Weiwei et al. In this methodology, the solvent, coformer and total amount

of enantiomers were maintained constant (x_S+x_R). As a result, the phase diagram was designed as saturation temperature as a function of the ratio x_S and x_S+x_R. The chiral cocrystal system with oxalic acid demonstrated the possibility of change the eutectic point. However, the shift observed was towards the enantiopure cocrystal and therefore reduce this region further. During this process we identified the requirement of the racemic cocrystals to have a lower solubility that the enantiopure cocrystal to push the eutectic composition in the correct direction.

The challenge to find the cocrystals of Eti and Lev with the selected coformers can be related with an asymmetry phase diagram of the cocrystal. To validate this assumption more demanding methodology can be used as high-performance liquid chromatography to analyse the composition of liquid phase remaining after crystallisation followed by the determination of crystal form through XRPD. It would be also important to identify the crystal form and monitor the formation of cocrystal by *in-situ* Raman spectroscopy attached to Crystal 16 equipment. This type of *in-situ* analysis reduces the potential for solid form transformation during the analysis period. A continuing challenges in the cocrystal area is the identification of co-formers to create successful cocrystals that have the desired properties. This methodology is advantageous due to the fact we are dealing with the solubility that has a link to the free energies of the solid forms.

In the chapter 4, we investigated the same chiral system but using high-pressure to evaluate the opportunity to explore this system as a model compound for nucleation measurements. In the compression, both compounds showed anisotropic compression. The Raman spectroscopy analysis highlighted a possible phase transition in Levetiracetam (~2 GPa) to form II and in Etiracetam (~1.5 GPa) to form III that was

confirmed by X-ray analysis. These subtle transition at relative high-pressure prohibited the use of this system for nucleation studies. Additionally, we evaluate the use of pressure for enantiomer resolution. The analysis of the density profile at high-pressure showed that Etiracetam increases density up to 1.7% at 4.8 GPa in relation to Lev, which turns spontaneous resolution through high pressure unlikely. The subtle phase transition in these materials was a real challenge for the analysis. One potential avenue that was discussed was the use of Neutron powder diffraction. This type of analysis is a strong method to evaluate the equation of state of materials due to the large number of data points for Pawley or Rietveld analysis. Any discontinuities would be clear rather than the use of one single crystal to evaluate the solid.

In terms of nucleation at pressure, it is dependent of the compression behaviour of the compound. The selection of a compound with a very well-known reversible phase transition below 1 GPa described in the literature could be a first step for this type of analysis so that a probability experiment can be performed following on from the work of ter Horst et al under ambient pressure conditions. To enable this, Raman Spectroscopy could be used to detect the phase transitions in the materials as long as the spectra have well-defined peaks that illustrate the transition. The Raman spectrum collection should be quick to minimize the uncertainty associated to the measurement and to be able to capture the change. The use Raman Spectroscopy mapping to scan a powder sample during compression could allow the determination of probability distributions of induction times. A further challenge that would need to be addressed is the increments of pressure using the DAC. These need to be control to secure reproducibility of the induction times.

In chapter 5, we evaluated the use of hydrochlorothiazide as a model compound for the nucleation study at high-pressure. This compound showed a promising compression behaviour at high-pressure. A reconstructive phase transition to new high-pressure polymorphic at ~ 0.55 GPa was observed under the microscope and detected using Raman Spectroscopy. However, this form remained stable after decompression to ambient condition making it impossible to reproduce the phase transition process for induction times measurements. The stability of the new polymorphic form opened the opportunity to characterize the form at ambient conditions. Large amounts of high-pressure form were produced using the large volume cell and analysed by X-ray powder diffraction. A combined dual Rietveld/Pawley refinement permitted the identification and indexing of the new high-pressure polymorph from the mixed phase samples. Unfortunately, this new phase remains unidentified.

The determination of high-pressure polymorphic form of hydrochlorothiazide is complex due to inexistence of a single crystal of this form and the mixture of forms obtained in the LVP. The application of cryo-recovery, compression at low temperatures follow by X-ray diffraction could present an opportunity to determine the crystal structure of the high-pressure form. This has been demonstrated on the recovery of high-pressure phases of magnesium sulfate pentahydrate with collection at HRPD at ISIS Neutron and Muon source. The high resolution of this instrument as well as low temperature collection may be a route to identify this new phase. High-pressure Neutron diffraction at Pearl Instrument at ISIS Neutron and Muon Source was discussed but the narrow window of d-spacing's available create a challenge for structure indexing and solution.

In conclusion, the path of this thesis was to explore the nucleation of organic molecular systems under ambient and high pressure conditions. We have analysed the formation of cocrystal of enantiopure and racemic solids of RS/S-2-(2-oxo-pyrrolidin-1-yl)-butyramide and extended the search for new solid-state forms using high pressure analysis. The behaviour of this system seems contrary to the analogous compound piracetam that yields multiple solid state forms. This different behaviour will add evidence to the global understanding of the organic solid state. The recovery of the high-pressure form of hydrochlorothiazide continues to build on the future application of high-pressure to isolate new solid forms for seeding ambient pressure crystallisations that could be complementary discovery avenue to those being used at present in industry.

Appendices

A.1 Details of the X-ray diffraction collection for Etiracetam.

Table A.1. Experimental details for Etiracetam: The refinement parameters for etiracetam on compression. For all structures: $C_8H_{14}N_2O_2$, M_r = 170.21, monoclinic, $P2_1/c$, Z = 4. Experiments were carried out using Bruker Kappa Apex II Duo diffractometer using with Mo Ka radiation. H-atom parameters were constrained.

	ETI_1	**ETI_2**	**ETI_3**	**ETI_4**
Temperature (K)	296	296	296	296
Pressure (GPa)	0.001	0.8	1.02	1.24
a, *b*, *c* (Å)	9.5887 (19), 7.8270 (16), 11.947 (2)	9.4631 (4), 7.6689 (7), 11.4366 (4)	9.4363 (3), 7.6314 (6), 11.3336 (4)	9.4031 (4), 7.5920 (9), 11.2372 (6)
β (°)	103.813 (5)	101.740 (2)	101.341 (2)	100.942 (4)
V (Å^3)	870.7 (3)	812.61 (9)	800.22 (7)	787.62 (11)
μ (mm^{-1})	0.09	0.10	0.10	0.10
Crystal size (mm)	0.2 × 0.2 × 0.08	0.2 × 0.2 × 0.08	0.2 × 0.2 × 0.08	0.2 × 0.2 × 0.08
Data collection				
Absorption correction	Multi-scan *SADABS2016*/2 (Bruker,2016/2) was used for absorption correction. wR2(int) was 0.0588 before and 0.0452 after correction. The Ratio of minimum to maximum transmission is 0.9361. The λ/2 correction factor is Not present.	Multi-scan *SADABS2016*/2 (Bruker,2016/2) was used for absorption correction. wR2(int) was 0.0758 before and 0.0471 after correction. The Ratio of minimum to maximum transmission is 0.9178. The λ/2 correction factor is Not present.	Multi-scan *SADABS2016*/2 (Bruker,2016/2) was used for absorption correction. wR2(int) was 0.0758 before and 0.0485 after correction. The Ratio of minimum to maximum transmission is 0.9156. The λ/2 correction factor is Not present.	Multi-scan *SADABS2016*/2 (Bruker,2016/2) was used for absorption correction. wR2(int) was 0.0631 before and 0.0446 after correction. The Ratio of minimum to maximum transmission is 0.8739. The λ/2 correction factor is Not present.
T_{min}, T_{max}	0.692, 0.745	0.684, 0.745	0.682, 0.745	0.651, 0.745
No. of measured, independent and observed [$I > 2\sigma(I)$] reflections	8875, 1775, 1162	3481, 610, 533	3579, 610, 539	3503, 605, 544
R_{int}	0.053	0.033	0.034	0.034
θ_{max} (°)	26.4	23.2	23.3	23.2
$(\sin\theta/\lambda)_{max}$ (Å^{-1})	0.625	0.555	0.556	0.555

Continued on next page

Table A.1 - *Continued from previous page*

Refinement				
$R[F^2 > 2\sigma(F^2)]$, $wR(F^2)$, S	0.043, 0.105, 1.05	0.032, 0.075, 1.13	0.031, 0.075, 1.09	0.034, 0.081, 1.12
No. of reflections	1775	610	610	605
No. of parameters	110	110	110	110
No. of restraints	84	84	84	84
$\Delta\rho_{max}$, $\Delta\rho_{min}$ (e Å^{-3})	0.17, -0.20	0.10, -0.11	0.10, -0.12	0.11, -0.13
	ETI_5	**ETI_6**	**ETI_7**	**ETI_8**
Temperature (K)	296	296	296	296
Pressure (GPa)	1.4	1.9	2.51	2.98
a, *b*, *c* (Å)	9.3873 (3), 7.5739 (5), 11.1967 (4)	9.319 (3), 7.506 (5), 10.984 (3)	9.290 (2), 7.445 (3), 10.912 (3)	9.2440 (6), 7.4025 (8), 10.8223 (9)
β (°)	100.759 (2)	99.91 (2)	99.574 (19)	99.170 (6)
V (Å^3)	782.07 (6)	756.8 (6)	744.2 (4)	731.09 (11)
μ (mm^{-1})	0.11	0.11	0.11	0.11
Crystal size (mm)	0.2 × 0.2 × 0.08	0.2 × 0.2 × 0.08	0.2 × 0.2 × 0.08	0.2 × 0.2 × 0.08
Data collection				
Absorption correction	Multi-scan *SADABS2016*/2 (Bruker,2016/2) was used for absorption correction. wR2(int) was 0.0710 before and 0.0447 after correction. The Ratio of minimum to maximum transmission is 0.9075. The λ/2 correction factor is Not present.	Multi-scan *SADABS2016*/2 (Bruker,2016/2) was used for absorption correction. wR2(int) was 0.1177 before and 0.0652 after correction. The Ratio of minimum to maximum transmission is 0.8449. The λ/2 correction factor is Not present.	Multi-scan *SADABS2016/2* (Bruker,2016/2) was used for absorption correction. wR2(int) was 0.0580 before and 0.0470 after correction. The Ratio of minimum to maximum transmission is 0.9074. The λ/2 correction factor is Not present.	Multi-scan *SADABS2016*/2 (Bruker,2016/2) was used for absorption correction. wR2(int) was 0.0645 before and 0.0473 after correction. The Ratio of minimum to maximum transmission is 0.9092. The λ/2 correction factor is Not present.
T_{min}, T_{max}	0.676, 0.745	0.629, 0.745	0.671, 0.745	0.677, 0.745
No. of measured, independent and observed [$I > 2\sigma(I)$] reflections	3463, 605, 535	3355, 588, 496	3369, 572, 494	3280, 554, 474
R_{int}	0.034	0.066	0.036	0.039
θ_{max} (°)	23.3	23.4	23.2	23.3
$(\sin\theta/\lambda)_{max}$ (Å^{-1})	0.556	0.558	0.555	0.556
Refinement				
$R[F^2 > 2\sigma(F^2)]$, $wR(F^2)$, S	0.035, 0.131, 1.29	0.046, 0.119, 1.07	0.032, 0.081, 1.06	0.033, 0.080, 1.10
No. of reflections	605	588	572	554
No. of parameters	110	110	110	110
No. of restraints	84	84	84	84
$\Delta\rho_{max}$, $\Delta\rho_{min}$ (e Å^{-3})	0.42, -0.43	0.16, -0.22	0.11, -0.12	0.10, -0.15

Continued on next page

Table A.1 - *Continued from previous page*

	ETI_9	**ETI_10**	**ETI_11**	**ETI_12**
Temperature (K)	296	296	296	296
Pressure (GPa)	3.51	3.95	4.84	5.51
a, *b*, *c* (Å)	9.2213 (10), 7.3717 (11), 10.7684 (15)	9.1948 (19), 7.329 (2), 10.696 (3)	9.1482 (5), 7.2820 (9), 10.6031 (7)	9.1124 (7), 7.2381 (13), 10.5263 (10)
β (°)	98.918 (10)	98.576 (18)	98.252 (4)	97.937 (6)
V (Å^3)	723.15 (17)	712.7 (3)	699.04 (11)	687.63 (15)
μ (mm^{-1})	0.11	0.12	0.12	0.12
Crystal size (mm)	0.2 × 0.2 × 0.08	0.2 × 0.2 × 0.08	0.2 × 0.2 × 0.08	0.2 × 0.2 × 0.08
Data collection				
Absorption correction	Multi-scan *SADABS2016*/2 (Bruker,2016/2) was used for absorption correction. wR2(int) was 0.1094 before and 0.0512 after correction. The Ratio of minimum to maximum transmission is 0.9047. The λ/2 correction factor is Not present.	Multi-scan *SADABS2016*/2 (Bruker,2016/2) was used for absorption correction. wR2(int) was 0.1059 before and 0.0612 after correction. The Ratio of minimum to maximum transmission is 0.8405. The λ/2 correction factor is Not present.	Multi-scan *SADABS2016*/2 (Bruker,2016/2) was used for absorption correction. wR2(int) was 0.0787 before and 0.0507 after correction. The Ratio of minimum to maximum transmission is 0.8958. The λ/2 correction factor is Not present.	Multi-scan *SADABS2016*/2 (Bruker,2016/2) was used for absorption correction. wR2(int) was 0.1018 before and 0.0563 after correction. The Ratio of minimum to maximum transmission is 0.9046. The λ/2 correction factor is Not present.
T_{min}, T_{max}	0.674, 0.745	0.626, 0.745	0.667, 0.745	0.674, 0.745
No. of measured, independent and observed [$I > 2\sigma(I)$] reflections	3137, 540, 449	3137, 542, 414	2953, 495, 402	2933, 492, 394
R_{int}	0.056	0.082	0.043	0.051
θ_{max} (°)	23.3	23.3	23.0	23.2
$(\sin\theta/\lambda)_{max}$ (Å^{-1})	0.556	0.556	0.549	0.554
$R[F^2 > 2\sigma(F^2)]$, $wR(F^2)$, S	0.038, 0.086, 1.08	0.057, 0.147, 1.05	0.041, 0.092, 1.14	0.044, 0.105, 1.10
No. of reflections	540	542	495	492
No. of parameters	110	110	110	110
No. of restraints	84	84	85	85
$\Delta\rho_{max}$, $\Delta\rho_{min}$ (e Å^{-3})	0.12, -0.15	0.24, -0.22	0.13, -0.14	0.17, -0.18

Continued on next page

Table A.1 - *Continued from previous page*

	ETI_13
Temperature (K)	296
Pressure (GPa)	6.29
a, *b*, *c* (Å)	9.0973 (5), 7.209 (1), 10.4748 (8)
β (°)	97.742 (5)
V (Å^3)	680.70 (11)
μ (mm^{-1})	0.12
Crystal size (mm)	0.2 × 0.2 × 0.08
Data collection	
Absorption correction	Multi-scan *SADABS2016*/2 (Bruker,2016/2) was used for absorption correction. wR2(int) was 0.0890 before and 0.0514 after correction. The Ratio of minimum to maximum transmission is 0.9055. The λ/2 correction factor is Not present.
T_{min}, T_{max}	0.675, 0.745
No. of measured, independent and observed [$I > 2\sigma(I)$] reflections	2841, 487, 387
R_{int}	0.061
θ_{max} (°)	23.2
$(\sin\theta/\lambda)_{max}$ (Å^{-1})	0.555
$R[F^2 > 2\sigma(F^2)]$, $wR(F^2)$, S	0.047, 0.106, 1.09
No. of reflections	487
No. of parameters	110
No. of restraints	85
$\Delta\rho_{max}$, $\Delta\rho_{min}$ (e Å^{-3})	0.17, -0.17

A.2 Details of the X-ray diffraction collection for Levetiracetam.

Table A.2- Experimental details for Levetiracetam: The refinement parameters for Levetiracetam on compression. For all structures: $C_8H_{14}N_2O_2$, M_r = 170.21, monoclinic, $P2_1$, Z = 2. Experiments were carried out using Bruker Kappa Apex II Duo diffractometer using with Mo Ka radiation. H-atom parameters were constrained.

	LEV1_1	**LEV1_2**	**LEV1_3**	**LEV1_4**
Temperature (K)	296	296	296	296
Pressure (GPa)	0.73	1.29	2	2.71
a, *b*, *c* (Å)	6.0104 (2), 7.8334 (6), 9.0806 (5)	5.9233 (7), 7.759 (2), 9.0336 (19)	5.8955 (2), 7.7395 (5), 9.0110 (4)	5.8023 (2), 7.6502 (5), 8.9508 (5)
β (°)	108.944 (4)	109.210 (12)	109.157 (3)	109.201 (4)
V (Å^3)	404.37 (4)	392.05 (14)	388.39 (3)	375.21 (4)
μ (mm^{-1})	0.10	0.11	0.11	0.11
Crystal size (mm)	0.08 × 0.05 × 0.05	0.08 × 0.05 × 0.05	0.08 × 0.05 × 0.05	0.08 × 0.05 × 0.05
Data collection				
Absorption correction	Multi-scan *SADABS2016*/2 (Bruker,2016/2) was used for absorption correction. wR2(int) was 0.1652 before and 0.0832 after correction. The Ratio of minimum to maximum transmission is 0.6898. The λ/2 correction factor is Not present.	Multi-scan *SADABS2016*/2 (Bruker,2016/2) was used for absorption correction. wR2(int) was 0.1145 before and 0.0490 after correction. The Ratio of minimum to maximum transmission is 0.8522. The λ/2 correction factor is Not present.	Multi-scan *SADABS2016*/2 (Bruker,2016/2) was used for absorption correction. wR2(int) was 0.0849 before and 0.0421 after correction. The Ratio of minimum to maximum transmission is 0.9111. The λ/2 correction factor is Not present.	Multi-scan *SADABS2016*/2 (Bruker,2016/2) was used for absorption correction. wR2(int) was 0.0732 before and 0.0427 after correction. The Ratio of minimum to maximum transmission is 0.8725. The λ/2 correction factor is Not present.
T_{min}, T_{max}	0.514, 0.745	0.635, 0.745	0.679, 0.745	0.650, 0.745
No. of measured, independent and observed [$I > 2\sigma(I)$] reflections	1766, 547, 501	1563, 529, 433	1817, 546, 525	1779, 526, 498
R_{int}	0.064	0.067	0.029	0.033
θ_{max} (°)	23.3	23.2	23.2	23.2
$(\sin\theta/\lambda)_{max}$ (Å^{-1})	0.555	0.555	0.554	0.554

Continued on next page

Table A.2 - *Continued from previous page*

Refinement				
$R[F^2 > 2\sigma(F^2)]$, $wR(F^2)$, S	0.058, 0.136, 1.13	0.047, 0.091, 1.15	0.037, 0.104, 1.23	0.037, 0.108, 1.14
No. of reflections	547	529	546	526
$\Delta\rangle_{max}$, $\Delta\rangle_{min}$ (e Å^{-3})	0.26, -0.22	0.16, -0.16	0.14, -0.14	0.16, -0.17
Absolute structure	Flack x determined using 197 quotients [(I+)-(I-)]/[(I+)+(I-)] (Parsons, Flack and Wagner, Acta Cryst. B69 (2013) 249-259).	Flack x determined using 142 quotients [(I+)-(I-)]/[(I+)+(I-)] (Parsons, Flack and Wagner, Acta Cryst. B69 (2013) 249-259).	Flack x determined using 211 quotients [(I+)-(I-)]/[(I+)+(I-)] (Parsons, Flack and Wagner, Acta Cryst. B69 (2013) 249-259).	Flack x determined using 207 quotients [(I+)-(I-)]/[(I+)+(I-)] (Parsons, Flack and Wagner, Acta Cryst. B69 (2013) 249-259).
Absolute structure parameter	0.1 (10)	0.0 (10)	0.7 (10)	0.9 (10)
	LEV1_5	**LEV1_6**	**LEV1_7**	**LEV1_8**
Temperature (K)	296	296	296	296
Pressure (GPa)	3.1	3.67	4.19	4.61
a, b, c (Å)	5.7528 (12), 7.591 (3), 8.914 (3)	5.7452 (4), 7.5918 (10), 8.9123 (11)	5.7244 (3), 7.5640 (7), 8.8946 (7)	5.7055 (3), 7.5379 (7), 8.8822 (8)
β (°)	109.149 (19)	109.209 (7)	109.213 (4)	109.154 (5)
V (Å^3)	367.7 (2)	367.08 (7)	363.68 (5)	360.85 (5)
μ (mm^{-1})	0.11	0.11	0.11	0.11
Crystal size (mm)	0.08 × 0.05 × 0.05	0.08 × 0.05 × 0.05	0.08 × 0.05 × 0.05	0.08 × 0.05 × 0.05

Continued on next page

Table A.2 - *Continued from previous page*

Data collection				
Absorption correction	Multi-scan *SADABS2016*/2 (Bruker,2016/2) was used for absorption correction. wR2(int) was 0.0828 before and 0.0438 after correction. The Ratio of minimum to maximum transmission is 0.8994. The λ/2 correction factor is Not present.	Multi-scan *SADABS2016*/2 (Bruker,2016/2) was used for absorption correction. wR2(int) was 0.0846 before and 0.0420 after correction. The Ratio of minimum to maximum transmission is 0.8609. The λ/2 correction factor is Not present.	Multi-scan *SADABS2016*/2 (Bruker,2016/2) was used for absorption correction. wR2(int) was 0.0846 before and 0.0420 after correction. The Ratio of minimum to maximum transmission is 0.8609. The λ/2 correction factor is Not present.	Multi-scan *SADABS2016*/2 (Bruker,2016/2) was used for absorption correction. wR2(int) was 0.0567 before and 0.0377 after correction. The Ratio of minimum to maximum transmission is 0.9013. The λ/2 correction factor is Not present.
T_{min}, T_{max}	0.670, 0.745	0.641, 0.745	0.641, 0.745	0.671, 0.745
No. of measured, independent and observed [$I > 2\sigma(I)$] reflections	1731, 512, 483	1730, 513, 481	1735, 514, 484	1724, 512, 469
R_{int}	0.031	0.031	0.145	0.189
θ_{max} (°)	23.2	23.2	23.2	23.3
$(\sin\theta/\lambda)_{max}$ (Å^{-1})	0.554	0.555	0.555	0.556
Refinement				
$R[F^2 > 2\sigma(F^2)]$, $wR(F^2)$, S	0.037, 0.102, 1.16	0.037, 0.108, 1.22	0.047, 0.118, 1.09	0.058, 0.148, 1.08
No. of reflections	512	513	514	512
$\Delta\rangle_{max}$, $\Delta\rangle_{min}$ (e Å^{-3})	0.20, -0.20	0.15, -0.17	0.19, -0.17	0.20, -0.20
Absolute structure	Flack x determined using 195 quotients [(I+)-(I-)]/[(I+)+(I-)] (Parsons, Flack and Wagner, Acta Cryst. B69 (2013) 249-259).	Flack x determined using 201 quotients [(I+)-(I-)]/[(I+)+(I-)] (Parsons, Flack and Wagner, Acta Cryst. B69 (2013) 249-259).	Flack x determined using 198 quotients [(I+)-(I-)]/[(I+)+(I-)] (Parsons, Flack and Wagner, Acta Cryst. B69 (2013) 249-259).	Flack x determined using 179 quotients [(I+)-(I-)]/[(I+)+(I-)] (Parsons, Flack and Wagner, Acta Cryst. B69 (2013) 249-259).
Absolute structure parameter	-0.9 (10)	2.0 (10)	-0.1 (10)	2.8 (10)

Computer programs: *SAINT* v8.37A (Bruker, 2015), Known Coordinates CSD: OFIQUR, OMIVUB, XL (Sheldrick, 2008), Olex2 (Dolomanov *et al.*, 2009).

Table A.3 Unit cell Parameters of Levetiracetam: Unit cell determinations of three different crystals of Levetiracetam.

	Pressure	a-axis (Å)	b-axis (Å)	c-axis (Å)	β-angle (º)	Volume (Å^3)
RT	0	6.272 (5)	7.993 (9)	9.199 (5)	108.645 (7)	437 (6)
LEV1_1	0.73	6.0104 (2)	7.8334 (6)	9.0806 (5)	108.944 (4)	404.37 (4)
LEV3_1	1.2	5.9675 (3)	7.7994 (6)	9.0541 (8)	109.004 (5)	398.44 (5)
LEV1_2	1.29	5.9233 (7)	7.759 (2)	9.0336 (19)	109.210 (12)	392.05 (14)
LEV1_3	2	5.8955 (2)	7.7395 (5)	9.0110 (4)	109.157 (3)	388.39 (3)
LEV2_1	2.12	5.816 (2)	7.6765 (12)	8.964 (3)	109.23 (2)	377.9 (14)
LEV3_2	2.68	5.8064 (4)	7.6566 (8)	8.9499 (12)	109.175 (7)	375.81 (7)
LEV1_4	2.71	5.8023 (2)	7.6502 (5)	8.9508 (5)	109.201 (4)	375.21 (4)
LEV1_5	3.1	5.7528 (12)	7.591 (3)	8.914 (3)	109.149 (19)	367.7 (2)
LEV3_3	3.59	5.7238 (4)	7.5596 (8)	8.8924 (1)	109.212 (6)	363.34 (6)
LEV1_6	3.67	5.7452 (4)	7.5918 (10)	8.9123 (11)	109.209 (7)	367.08 (7)
LEV2_2	3.81	5.692 (3)	7.5499 (14)	8.883 (3)	109.27 (3)	360.3 (18)
LEV1_7	4.19	5.7244 (3)	7.5640 (7)	8.8946 (7)	109.213 (4)	363.68 (5)
LEV1_8	4.61	5.7055 (3)	7.5379 (7)	8.8822 (8)	109.154 (5)	360.85 (5)
LEV2_3	4.83	5.647 (3)	7.4853 (14)	8.841 (4)	109.16 (3)	353 (19)

B.1 Pawley fit of HCT samples

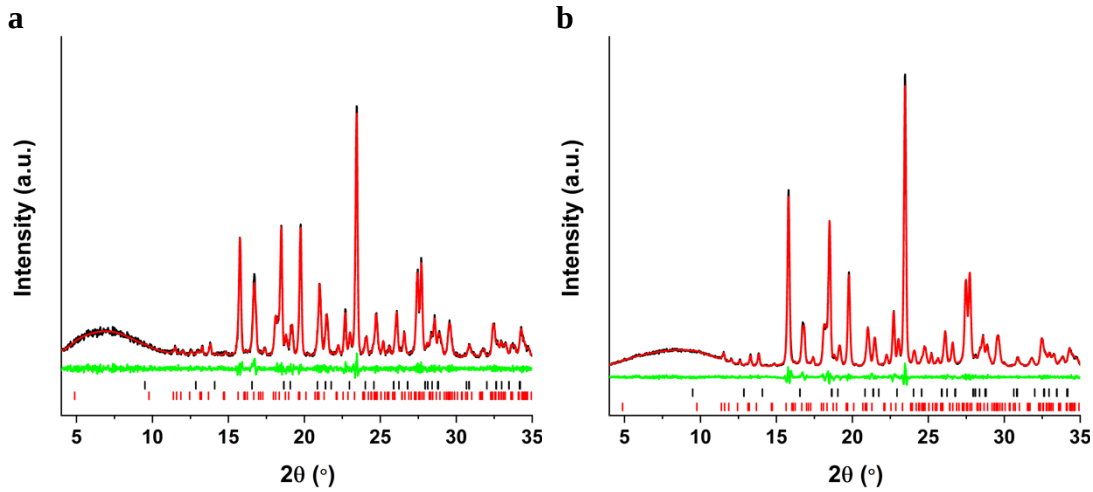

Figure B.1 - The Pawley fit of **a** HCT-A and **b** HCT-B. Black tick marks represent the positions of the HCT form I reflections and red tick marks show the positions of the new HCT form reflections.

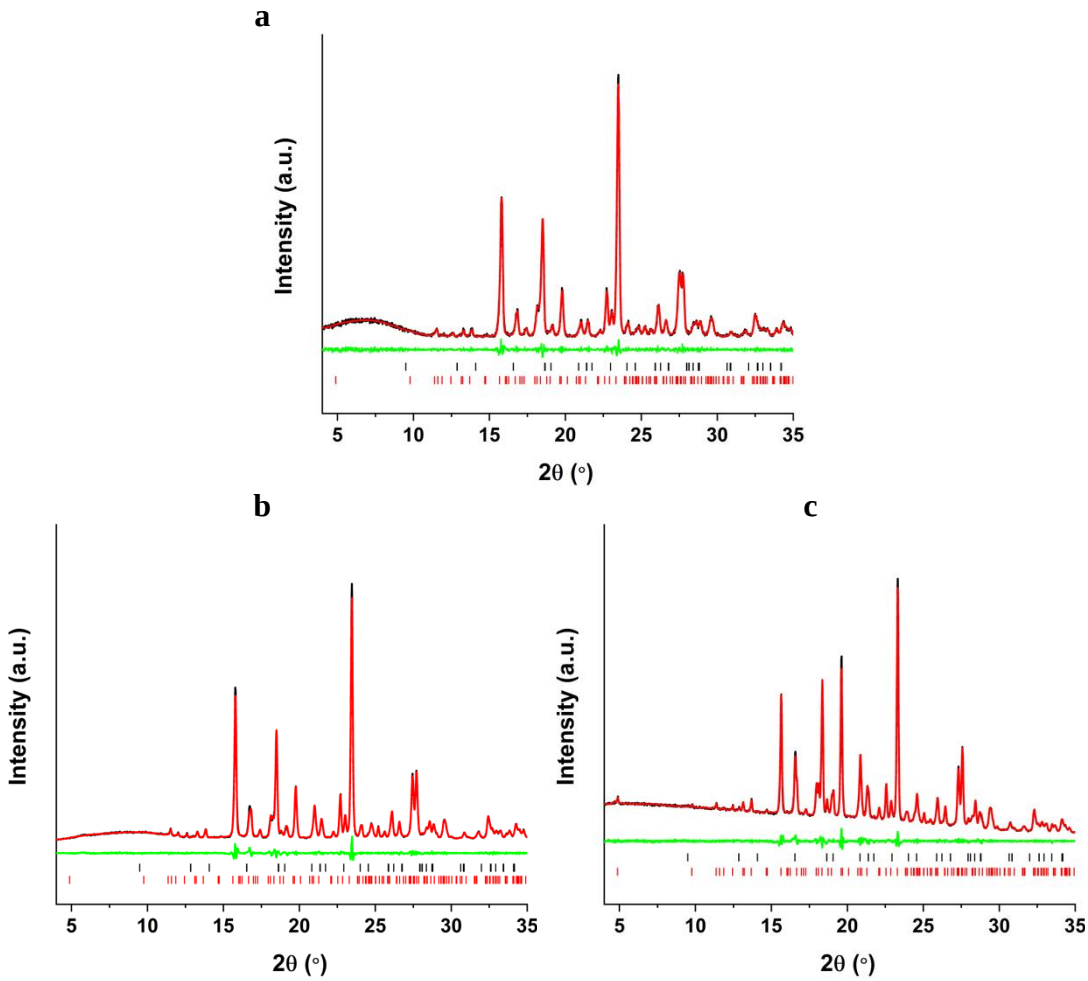

Figure B.2 - The Pawley fit of **a** HCT- Cand , **b** HCT-C1 and **c** HCT-3. Black tick marks represent the positions of the HCT form I reflections and red tick marks show the positions of the new HCT form reflections.

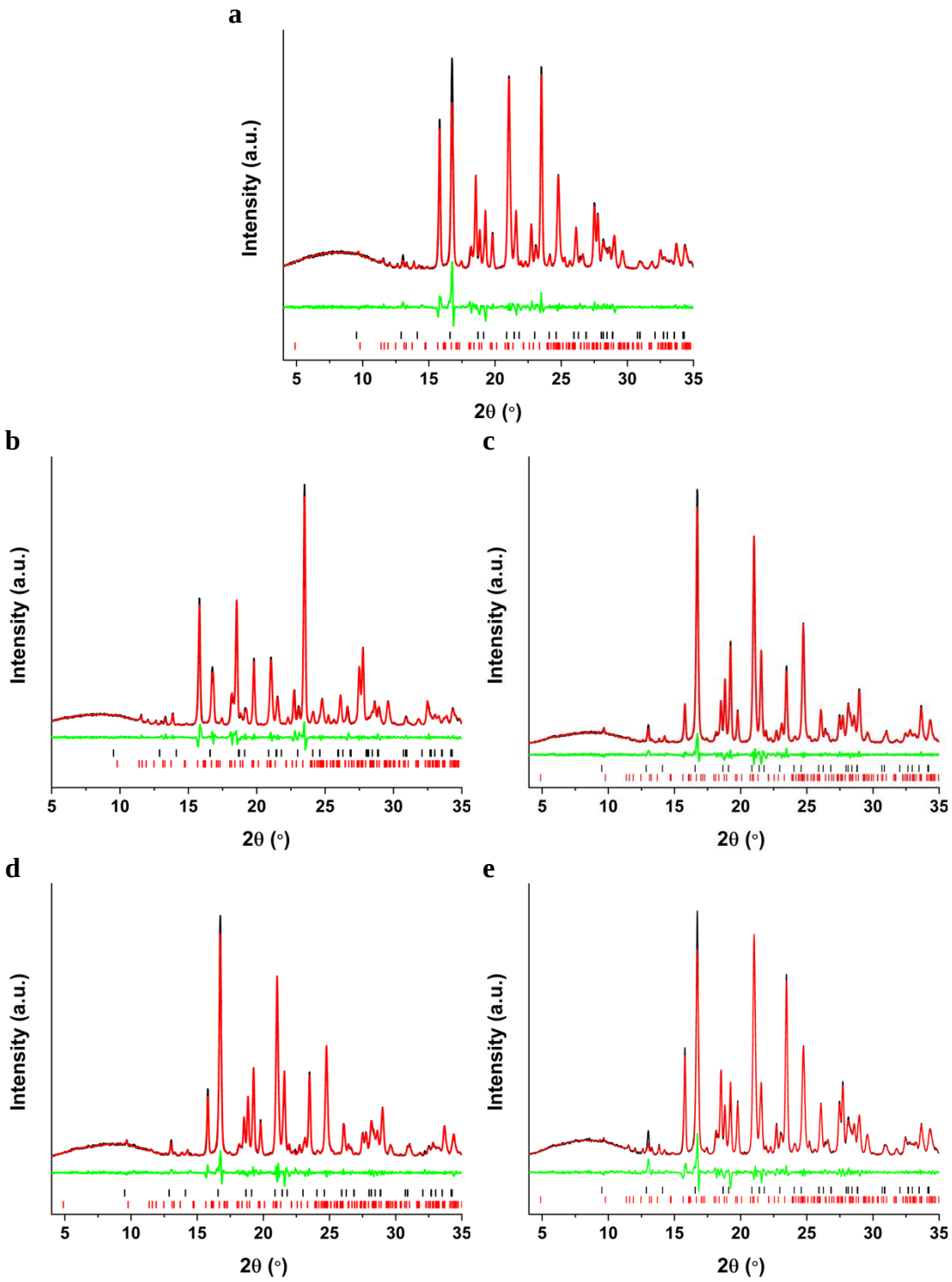

Figure B.3 – The Pawley fit of **a** HCT-D, **b** HCT-E, **c** HCT-F, d HCT-G and **e** HCT-H. Black tick marks represent the positions of the HCT form I reflections and red tick marks show the positions of the new HCT form reflections